

# The XMM-SERVS survey: new *XMM-Newton* point-source catalog for the XMM-LSS field

C.-T.J. Chen<sup>1,2\*</sup>, W.N. Brandt<sup>1,2,3</sup>, B. Luo<sup>4,5</sup>, P. Ranalli<sup>6</sup>, G. Yang<sup>1,2</sup>, D.M. Alexander<sup>7</sup>, F.E. Bauer<sup>8,9,10</sup>, D.D. Kelson<sup>11</sup>, M. Lacy<sup>12</sup>, K. Nyland<sup>12</sup>, P. Tozzi<sup>13</sup>, F. Vito<sup>1,2</sup>, M. Cirasuolo<sup>14</sup>, R. Gilli<sup>15</sup>, M.J. Jarvis<sup>16,17</sup>, B.D. Lehmer<sup>18</sup>, M. Paolillo<sup>19</sup>, D.P. Schneider<sup>1,2</sup>, O. Shemmer<sup>20</sup>, I.R. Smail<sup>7</sup>, M. Sun<sup>21,22</sup>, M. Tanaka<sup>23</sup>, M. Vaccari<sup>17,24</sup>, C. Vignali<sup>25,15</sup>, Y.Q. Xue<sup>21,22</sup>, M. Banerji<sup>26</sup>, K.E. Chow<sup>27</sup>, B. Häußler<sup>28</sup>, R.P. Norris<sup>29,27</sup>, J.D. Silverman<sup>30</sup>, and J.R. Trump<sup>31</sup>

<sup>1</sup>Department of Astronomy & Astrophysics, 525 Davey Lab, The Pennsylvania State University, University Park, PA 16802, USA

<sup>2</sup>Institute for Gravitation and the Cosmos, The Pennsylvania State University, University Park, PA 16802, USA

<sup>3</sup>Department of Physics, The Pennsylvania State University, University Park, PA 16802, USA

<sup>4</sup>School of Astronomy and Space Science, Nanjing University, Nanjing 210093, China

<sup>5</sup>Key Laboratory of Modern Astronomy and Astrophysics (Nanjing University), Ministry of Education, Nanjing, Jiangsu 210093, China

Accepted XXX. Received YYY; in original form ZZZ

## ABSTRACT

We present an X-ray point-source catalog from the XMM-Large Scale Structure survey region (XMM-LSS), one of the XMM-Spitzer Extragalactic Representative Volume Survey (XMM-SERVS) fields. We target the XMM-LSS region with 1.3 Ms of new *XMM-Newton* AO-15 observations, transforming the archival X-ray coverage in this region into a 5.3 deg<sup>2</sup> contiguous field with uniform X-ray coverage totaling 2.7 Ms of flare-filtered exposure, with a 46 ks median PN exposure time. We provide an X-ray catalog of 5242 sources detected in the soft (0.5–2 keV), hard (2–10 keV), and/or full (0.5–10 keV) bands **with a 1% expected spurious fraction determined based on simulations**. A total of 2381 new X-ray sources are detected compared to previous source catalogs in the same area. Our survey has flux limits of  $1.7 \times 10^{-15}$ ,  $1.3 \times 10^{-14}$ , and  $6.5 \times 10^{-15}$  erg cm<sup>-2</sup> s<sup>-1</sup> over 90% of its area in the soft, hard, and full bands, respectively, which is comparable to those of the XMM-COSMOS survey. We identify multiwavelength counterpart candidates for 98.4% of the X-ray sources, of which 94% are considered to be reliable based on their matching likelihood ratios. The reliabilities of these high-likelihood ratio counterparts are further confirmed to be  $\approx 97\%$  reliable based on deep *Chandra* coverage over  $\approx 5\%$  of the XMM-LSS region. Results of multiwavelength identifications are also included in the source catalog, along with basic optical-to-infrared photometry and spectroscopic redshifts from publicly available surveys. We compute photometric redshifts for X-ray sources in 4.5 deg<sup>2</sup> of our field where forced-aperture multi-band photometry is available;  $> 70\%$  of the X-ray sources in this subfield have either spectroscopic or high-quality photometric redshifts.

**Key words:** catalogues – surveys – galaxies:active – X-rays:galaxies – quasars: general

\* E-mail: ctchen@psu.edu

<sup>6</sup>Lund Observatory, Box 43, 22100 Lund, Sweden

<sup>7</sup>Centre for Extragalactic Astronomy, Department of Physics, Durham University, South Road, Durham, DH1 3LE, UK

<sup>8</sup>Instituto de Astrofísica y Centro de Astroingeniería, Facultad

de Física, Pontificia Universidad Católica de Chile, Casilla 306, Santiago 22, Chile

<sup>9</sup>Millennium Institute of Astrophysics (MAS), Chile

<sup>10</sup>Space Science Institute, 4750 Walnut Street, Suite 205, Boulder, Colorado 80301, USA

<sup>11</sup>The Observatories, The Carnegie Institution for Science, 813

## 1 INTRODUCTION

Due to the penetrating nature of X-ray emission and its ubiquity from accreting supermassive black holes (SMBHs), extragalactic X-ray surveys have provided an effective census of active galactic nuclei (AGNs), including obscured systems, in the distant universe. Over at least the past three decades, the overall design of cosmic X-ray surveys has followed a “wedding cake” strategy. At the extremes of this strategy, some surveys have ultra-deep X-ray coverage and a narrow “pencil-beam” survey area ( $\lesssim 1 \text{ deg}^2$ ), while others have shallow X-ray coverage over a wide survey area ( $\approx 10\text{--}10^4 \text{ deg}^2$ ). The wealth of data from cosmic X-ray surveys (and their co-located multiwavelength surveys) have provided a primary source of information in shaping understanding of how SMBHs grow through cosmic time, where deep surveys generally sample high-redshift, moderately luminous AGNs, and wide-field surveys generally probe the high-luminosity, rare objects that are missed by surveys covering smaller volumes. However, narrow-field surveys lack the contiguous volume to encompass a wide range of cosmic

large-scale structures, and wide-field surveys generally lack the X-ray sensitivity to track the bulk of the AGN population through the era of massive galaxy assembly (see [Brandt & Alexander 2015](#) for a recent review).

Among extragalactic X-ray surveys, the medium-deep COSMOS survey over  $\approx 2 \text{ deg}^2$  has the needed sensitivity-area combination to begin to track how a large fraction of distant SMBH growth relates to cosmic large-scale structures (e.g., [Hasinger et al. 2007](#); [Civano et al. 2016](#)). However, even COSMOS cannot sample the full range of cosmic environments. The largest structures found in cold dark matter simulations are already as large as the angular extent of COSMOS at  $z \approx 1$  (80–100 Mpc in comoving size, which covers  $2\text{--}3 \text{ deg}^2$ ; e.g., see [Klypin et al. 2016](#)). Clustering analyses also demonstrate that COSMOS-sized fields are still subject to significant cosmic variance (e.g., [Meneux et al. 2009](#); [de la Torre et al. 2010](#); [Skibba et al. 2014](#)).

Therefore, to study SMBH growth across the full range of cosmic environments and minimize cosmic variance, it is necessary to obtain multiple medium-deep X-ray surveys in distinct sky regions (e.g., [Driver & Robotham 2010](#); [Moster et al. 2011](#)) with multiwavelength data comparable to those of COSMOS. In this work, we present a catalog of 5242 *XMM-Newton* sources detected over  $5.3 \text{ deg}^2$  in one of the well-studied *Spitzer* Extragalactic Representative Volume Survey (SERVS, [Mauduit et al. 2012](#)) fields, the XMM-Large Scale Structure (XMM-LSS) region. This is the first field of the broader XMM-SERVS survey which aims to expand the parameter space of X-ray surveys with three  $> 3 \text{ deg}^2$  surveys reaching XMM-COSMOS-like depths, including XMM-LSS, Wide *Chandra* Deep Field-South (W-CDF-S), and ELAIS-S1.<sup>1</sup> These three extragalactic fields have been chosen based on their excellent multiwavelength coverage and superior legacy value. We list the current and scheduled multiwavelength coverage of XMM-SERVS in Table 1.

The X-ray source catalog presented here has been generated using a total of 1.3 Ms of *XMM-Newton* AO-15 observations in the XMM-LSS field (specifically the region covered by SERVS), plus all archival *XMM-Newton* data in this same region. Our AO-15 observations target the central part of XMM-LSS adjacent to (and partly including) the Subaru *XMM-Newton* Deep Survey (SXDS, [Ueda et al. 2008](#)), transforming the complex archival *XMM-Newton* coverage in this region into a contiguous  $5.3 \text{ deg}^2$  field with relatively uniform X-ray coverage. The median clean exposure time with the PN instrument is  $\approx 46 \text{ ks}$ , reaching survey depths comparable to those of XMM-COSMOS (e.g., [Cappelluti et al. 2009](#)) and SXDS. We also present multiwavelength counterparts, basic photometric properties, and spectroscopic redshifts obtained from the literature. Photometric redshifts are derived over a  $1 \text{ deg}^2$  region, demonstrating what will soon be possible over the entire  $5.3 \text{ deg}^2$  field. The excellent multiwavelength coverage in the XMM-SERVS XMM-LSS field will provide the necessary data for studying the general galaxy population and tracing large-scale structures. The combination of these multiwavelength data and the new X-ray source

Santa Barbara St., Pasadena, CA 91101

<sup>12</sup>National Radio Astronomy Observatory, 520 Edgemont Road, Charlottesville, VA 22903, USA

<sup>13</sup>INAF, Osservatorio Astrofisico di Arcetri, Largo E. Fermi 5, I-50125, Firenze, Italy

<sup>14</sup>European Southern Observatory, Karl-Schwarzschild-Str. 2, 85748 Garching b. München, Germany

<sup>15</sup>INAF – Osservatorio Astronomico di Bologna, Via Gobetti 93/3, 40129 Bologna, Italy

<sup>16</sup>Oxford Astrophysics, Denys Wilkinson Building, University of Oxford, Keble Road, Oxford OX1 3RH, UK

<sup>17</sup>Department of Physics, University of the Western Cape, Bellville 7535, South Africa

<sup>18</sup>Department of Physics, University of Arkansas, 226 Physics Building, 825 West Dickson Street, Fayetteville, AR 72701, USA

<sup>19</sup>Dip.di Fisica Ettore Pancini, Universit di Napoli Federico II, via Cintia, 80126, Napoli, Italy

<sup>20</sup>Department of Physics, University of North Texas, Denton, TX 76203, USA

<sup>21</sup>CAS Key Laboratory for Research in Galaxies and Cosmology, Department of Astronomy, University of Science and Technology of China, Hefei 230026, China

<sup>22</sup>School of Astronomy and Space Science, University of Science and Technology of China, Hefei 230026, China

<sup>23</sup>National Astronomical Observatory of Japan, 2-21-1 Osawa, Mitaka, Tokyo 181-8588, Japan

<sup>24</sup>INAF – Istituto di Radioastronomia, via Gobetti 101, 40129 Bologna, Italy

<sup>25</sup>Dipartimento di Fisica e Astronomia, Universit degli Studi di Bologna, Via Gobetti 93/2, 40129 Bologna, Italy

<sup>26</sup>Institute of Astronomy, University of Cambridge, Madingley Road, Cambridge CB3 0HA, United Kingdom

<sup>27</sup>CSIRO Astronomy and Space Science, PO Box 76, Epping, NSW, 1710, Australia

<sup>28</sup>European Southern Observatory, Alonso de Cordova 3107, Vitacura, Santiago, Chile

<sup>29</sup>Western Sydney University, Locked Bag 1797, Penrith South, NSW 1797, Australia

<sup>30</sup>Kavli Institute for the Physics and Mathematics of the Universe, The University of Tokyo, Kashiwa, Japan 277-8583 (Kavli IPMU, WPI)

<sup>31</sup>Department of Physics, University of Connecticut, 2152 Hillside Road, Storrs, CT 06269, USA

<sup>1</sup> *XMM-Newton* observations of W-CDF-S and ELAIS-S1 have been allocated via the AO-17 *XMM-Newton* Multi-year Heritage Program.

**Table 1.** Current and scheduled 1–10 deg<sup>2</sup> multiwavelength coverage of the XMM-SERVS fields. References: [a] Franzen et al. (2015); [b] Jarvis et al. (2017); [c] Oliver et al. (2012); [d] Lonsdale et al. (2003); [e] Mauduit et al. (2012). Note that SERVS has recently been expanded to cover the full LSST deep drilling fields (*Spitzer* Program ID 11086). [f] Jarvis et al. (2012); [g] [http://www.ast.cam.ac.uk/~mbanerji/VEILS/veils\\_index.html](http://www.ast.cam.ac.uk/~mbanerji/VEILS/veils_index.html); [h] Diehl et al. (2014); [i] Aihara et al. (2017); [j] Tonry et al. (2011); [k] Vaccari et al. (2016); [l] <http://www.lsst.org/News/enews/deep-drilling-201202.html>; [m] Kelson et al. (2014); Patel et al. (2015); [n] Coil et al. (2010); [o] <https://devilsurvey.org/wp/>; [p] <http://www.roe.ac.uk/~ciras/MOONS/VLT-MOONS.html>; [q] Takada et al. (2014); [r] <http://www.galex.caltech.edu/researcher/techdoc-ch2.html>.

Band	Survey Name	Coverage (XMM-LSS, W-CDF-S, ELAIS-S1); Notes
Radio	Australia Telescope Large Area Survey ( <b>ATLAS</b> ) <sup>a</sup> <b>MIGHTEE</b> Survey (Starting Soon) <sup>b</sup>	–, 3.7, 2.7 deg <sup>2</sup> ; 15 μJy rms depth at 1.4 GHz 4.5, 3, 4.5 deg <sup>2</sup> ; 1 μJy rms depth at 1.4 GHz
FIR	<i>Herschel</i> Multi-tiered Extragal. Surv. ( <b>HerMES</b> ) <sup>c</sup>	0.6–18 deg <sup>2</sup> ; 5–60 mJy depth at 100–500 μm
MIR	<i>Spitzer</i> Wide-area IR Extragal. Survey ( <b>SWIRE</b> ) <sup>d</sup>	9.4, 8.2, 7.0 deg <sup>2</sup> ; 0.04–30 mJy depth at 3.6–160 μm
NIR	<i>Spitzer</i> Extragal. Rep. Vol. Survey ( <b>SERVS</b> ) <sup>e</sup> VISTA Deep Extragal. Obs. Survey ( <b>VIDEO</b> ) <sup>f</sup> VISTA Extragal. Infr. Legacy Survey ( <b>VEILS</b> ) <sup>g</sup>	4.5, 3, 4.5 deg <sup>2</sup> ; 2 μJy depth at 3.6 and 4.5 μm 4.5, 3, 4.5 deg <sup>2</sup> ; ZYJK <sub>s</sub> to $m_{AB} \approx 23.8\text{--}25.7$ 3, 3, 3 deg <sup>2</sup> ; JK <sub>s</sub> to $m_{AB} \approx 24.5\text{--}25.5$
Optical Photometry	Dark Energy Survey ( <b>DES</b> ) <sup>h</sup> Hyper Suprime-Cam ( <b>HSC</b> ) Deep Survey <sup>i</sup> Pan-STARRS1 Medium-Deep Survey ( <b>PS1MD</b> ) <sup>j</sup> VST Opt. Imaging of CDF-S and ES1 ( <b>VOICE</b> ) <sup>k</sup> SWIRE optical imaging <sup>d</sup> <b>LSST</b> deep-drilling field (Planned) <sup>l</sup>	9, 6, 9 deg <sup>2</sup> ; Multi-epoch griz, $m_{AB} \approx 27$ co-added 5.3, –, – deg <sup>2</sup> ; grizy to $m_{AB} \approx 25.3\text{--}27.5$ 8, –, 8 deg <sup>2</sup> ; Multi-epoch grizy, $m_{AB} \approx 26$ co-added –, 4.5, 3 deg <sup>2</sup> ; Multi-epoch ugri, $m_{AB} \approx 26$ co-added 8, 7, 6 deg <sup>2</sup> ; u'g'r'i'z' to $m_{AB} \approx 24\text{--}26$ 10, 10, 10 deg <sup>2</sup> ; ugrizy, $\gtrsim 10000$ visits per field
Optical/NIR Spectroscopy	Carnegie- <i>Spitzer</i> -IMACS Survey ( <b>CSI</b> ) <sup>m</sup> PRISM Multi-object Survey ( <b>PRIMUS</b> ) <sup>n</sup> AAT Deep Extragal. Legacy Survey ( <b>DEVILS</b> ) <sup>o</sup> VLT <b>MOONS</b> Survey (Scheduled) <sup>p</sup> Subaru <b>PFS</b> survey (Planned) <sup>q</sup>	6.9, 4.8, 3.6 deg <sup>2</sup> ; 140000 redshifts, 3.6 μm selected 2.9, 2.0, 0.9 deg <sup>2</sup> ; 77000 redshifts to $i_{AB} \approx 23.5$ 3.0, 1.5, – deg <sup>2</sup> ; 43500 redshifts to $Y = 21.2$ 4.5, 3, 4.5 deg <sup>2</sup> ; 210000 redshifts to $H_{AB} \approx 23.5$ 5.3, –, – deg <sup>2</sup> ; $J \approx 23.4$ for HSC deep fields.
UV	<i>GALEX</i> Deep Imaging Survey <sup>r</sup>	8, 7, 7 deg <sup>2</sup> ; Depth $m_{AB} \approx 25$

catalog (along with similar data for COSMOS and the other XMM-SERVS fields) will enable potent studies of SMBH growth across the full range of cosmic environments, from voids to massive clusters, while minimizing cosmic variance effects. The *XMM-Newton* source catalog and several associated data products are being made publicly available along with this paper.

This paper is organized as follows: in §2 we present the details of the new and archival observations, and the procedures for data reduction. In §3 we describe the X-ray source-searching strategies and the details of the production of the X-ray point-source catalog. §3.6 outlines the reliability assessment of the X-ray catalog using simulated X-ray observations. The survey sensitivity and the number counts are also presented here. In §4, we describe the multiwavelength identification methods and reliability assessments, as well as basic multiwavelength properties including spectroscopic and photometric redshifts. A summary is given in §5. The source catalog and the descriptions of columns are included in the Appendix A. Multiwavelength matching results using the Bayesian matching code NWAY are included in Appendix B. **The photometric redshift catalog for the galaxies in our survey region is presented in Appendix C.** Throughout the paper, we assume a ΛCDM cosmology with

$H_0 = 70$  km s<sup>−1</sup> Mpc<sup>−1</sup>,  $\Omega_m = 0.3$ , and  $\Omega_\Lambda = 0.7$ . We adopt a Galactic column density  $N_H = 3.57 \times 10^{20}$  cm<sup>−2</sup> along the line of sight to the center of the source-detection region at RA = 35.6625°, DEC = −4.795° (e.g., Stark et al. 1992).<sup>2</sup> AB magnitudes are used unless noted otherwise.

## 2 XMM-NEWTON OBSERVATIONS IN THE XMM-LSS REGION AND DATA REDUCTION

### 2.1 XMM-Newton and *Chandra* data in the XMM-LSS region

The XMM-LSS field has been targeted by a number of *XMM-Newton* surveys of different sensitivities (e.g., see Fig. 3 of Brandt & Alexander 2015 and Fig. 1 of Xue 2017). The original XMM-LSS survey was an  $\approx 11$  deg<sup>2</sup> field typically covered by observations of  $\approx 10$  ks exposure time per pointing (Pacaud et al. 2006; Pierre et al. 2016). Within the 11 deg<sup>2</sup> field,  $\approx 4$  deg<sup>2</sup> were observed by the *XMM-Newton* Medium Deep Survey (XMDS, 20–25 ks exposure depth,

<sup>2</sup> Derived using the COLDEN task included in the CIAO software package.

**Table 2.** The *XMM-Newton* data used to create the source catalog include 155 pointings with a total of 2.7 Ms of flare-filtered exposure time, of which 1.1 Ms is from the new AO-15 observations.<sup>a</sup> Columns from left to right: target field, *XMM-Newton* revolution, *XMM-Newton* ObsID, observation starting date/time, Right Ascension and Declination of the pointing center (J2000, degrees), cleaned exposure time for PN, MOS1, and MOS2 in each pointing. This table is available in its entirety online.

Field	Revolution	ObsID	Date (UT)	R.A.	Decl.	GTI (PN) (ks)	GTI (MOS1) (ks)	GTI (MOS2) (ks)
AO-15	3054	0780450101	2016-08-13T01:34:06	35.81072	-5.15989	20.91	23.61	23.61
XMM-LSS	1205	0404965101	2006-07-09T08:08:08	35.80953	-5.48532	3.44	10.36	9.91
XMDS	287	0111110401	2001-07-03T14:01:54	35.97582	-5.15253	21.40	27.20	27.40
SXDS	118	0112370101	2000-07-31T21:57:54	34.47819	-4.98115	39.13	42.70	42.83
XMM-XXL-North	2137	0677580101	2011-08-10T01:53:35	37.16867	-4.49993	4.94	5.93	5.52
XMM-XXL-North	2137	0677580101	2011-08-10T01:53:35	37.33404	-4.49993	2.01	6.47	6.67
XLSSJ022404.0-041328	0928	0210490101	2005-01-01T19:08:30	36.03267	-4.20230	80.28	87.98	87.98

<sup>a</sup>: MOS only (MOS1 and MOS2 have the same exposure time). For PN, the total flare-filtered time is 2.3 Ms, of which 0.9 Ms is from the new AO-15 observations.

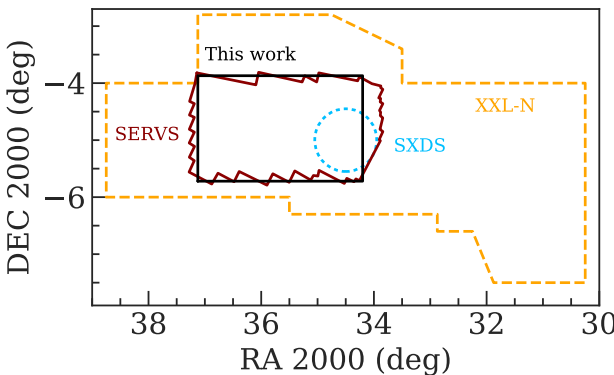


**Figure 1.** Illustration of the survey regions of XMM-XXL-North (XXL-N, Pierre et al. 2016, orange dashed line), the Subaru *XMM-Newton* Deep Survey (SXDS, Ueda et al. 2008, blue dotted circle), and the XMM-SERVS survey of XMM-LSS presented in this work (black box). The *Spitzer* SERVS coverage of XMM-LSS is also shown as the red polygon.

(Chiappetti et al. 2005). In addition, the Subaru *XMM-Newton* Deep Survey (SXDS, Ueda et al. 2008), adjacent to the XMDS field, covers a  $1.14 \text{ deg}^2$  area and reaches a nominal  $\approx 50$  ks exposure per pointing (Ueda et al. 2008). Moreover, the XMM-LSS field recently became a part of the  $25 \text{ deg}^2$  XMM-XXL-North field (Pierre et al. 2016), which has similar *XMM-Newton* coverage as the original XMM-LSS survey (i.e.,  $\approx 10$  ks depth).

In addition to the *XMM-Newton* data, the XMM-LSS region has extensive multiwavelength coverage (see Table 1 for a summary, also see Vaccari 2016). In particular, the central  $\approx 5 \text{ deg}^2$  area of the XMM-XXL-North field (i.e., the combination of the XMDS and SXDS fields) was selected to be one of the SERVS fields. This sky region is covered uniformly by multiple photometric and spectroscopic surveys (see Sec. 4 for more details), and it is one of the deep drilling fields of the Dark Energy Survey (Diehl et al. 2014) and the upcoming Large Synoptic Survey Telescope (LSST) surveys (see Table 1). Compared to the relatively uniform multiwavelength data, archival *XMM-Newton* observations covering this sky region span a wide range of exposure time (see Table 2). In order to advance studies of accreting SMBHs and their environments, deep X-ray observations with similar areal coverage are required in addition to the rich multiwavelength data in this field. To this end, we obtained *XMM-Newton* AO-15 observations taken

between July 2016 and February 2017 with a total of 1.3 Ms exposure time. The relative sky coverage of our survey region, XMM-XXL-North, and SXDS are displayed in Fig 1. Our AO-15 data include 67 *XMM-Newton* observations. In addition to the new data, we made use of all the overlapping archival *XMM-Newton* observations to create a sensitive *XMM-Newton* survey contiguously covering most of the SERVS data in the XMM-LSS region. After excluding observations that were completely lost due to flaring background (see §2.2), the archival data used here include 51 observations culled from the 10 ks XMM-LSS survey, 18 observations from XMDS with 20–25 ks exposures, four mosaic-mode observations<sup>3</sup> obtained as part of the XMM-XXL survey (Pierre et al. 2016), four archival *XMM-Newton* observations targeting galaxy clusters identified in the XMM-XXL-North and XMM-LSS surveys ( $\approx 30$ –100 ks), and the ten 50 ks observations from SXDS. We present the details of each observation in Table 2, and show the positions of each *XMM-Newton* observation used in this work in Fig. 2.

Our AO-15 observations were separated into two epochs to minimize the effects of background flaring. We first observed the XMM-LSS sky region in the SERVS footprint with  $\approx 1$  Ms of *XMM-Newton* exposure time during July–August 2016. These first observations were screened for flaring backgrounds (§2.2); we then re-observed the background-contaminated sky regions using the remaining 0.3 Ms. We also observed the SXDS region in which one of the SXDS observations carried out in 2002 was severely affected by background flares. In this work, we present an X-ray source catalog obtained from a  $5.3 \text{ deg}^2$  sky-region with  $34.2^\circ \leq \alpha_{\text{J2000}} \leq 37.125^\circ$  and  $-5.72^\circ \leq \delta_{\text{J2000}} \leq -3.87^\circ$ <sup>4</sup> (black rectangle in Fig 1 and Fig 2). The sky region is primarily selected by the footprint of our AO-15 observations, with additional SXDS data within the SERVS footprint in the south-west corner. A total of 3.0 Ms of raw *XMM-Newton* observations are used for generating the X-ray source catalog.

In addition to the *XMM-Newton* data, there are also a number of *Chandra* observations in our source-search region, including 18 observations of 10–90 ks exposure depth following up X-ray galaxy clusters identified in the XMM-LSS and XMM-XXL surveys (PIs: Andreon, S.; Jones, L.;

<sup>3</sup> Each mosaic-mode observation is comprised of a number of 10 ks exposures, see [https://xmm-tools.cosmos.esa.int/external/xmm\\_user\\_support/documentation/unb/mosaic.html](https://xmm-tools.cosmos.esa.int/external/xmm_user_support/documentation/unb/mosaic.html).

<sup>4</sup> This is equivalent to the galactic coordinates  $170.25184^\circ < l < 172.07153^\circ$ ,  $-60.49169^\circ < b < -57.17011^\circ$ .

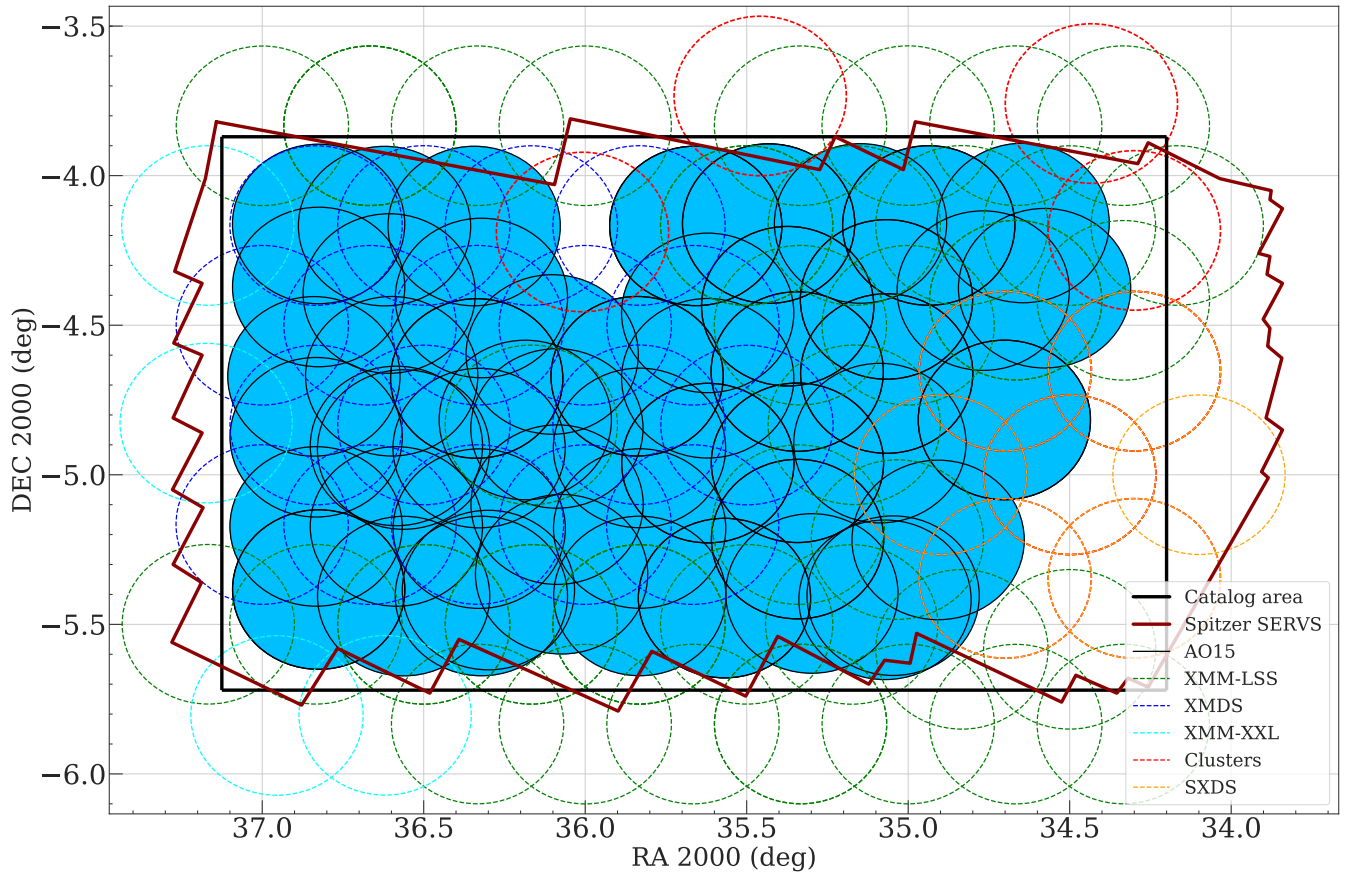


**Figure 2.** Locations of the *XMM-Newton* observations used in this work. The AO-15 observations are marked as the blue-filled circles with solid boundaries. The archival observations are marked as dashed circles. Circles with green, orange, blue, and cyan colors are for XMM-LSS, SXDS, XMDS, and XMM-XXL observations, respectively. The RA/DEC range of our catalog selection area is indicated by the black rectangle, and the *Spitzer* SERVS footprint is marked as the dark-red polygon. Our AO-15 observations do not cover the entirety of the SERVS region, because the existing data from SXDS (bottom-right corner, orange circles) and from deep X-ray cluster observations (top-middle and top-right, the red circles) reached the desired depth.

Mantz, A.; Maughan, B.; Murray, S.; Pierre, M.), these observations occupy a wide RA/DEC range in our catalog region. In §4.1 and §4.2, we make use of the *Chandra* sources in these observations culled from the *Chandra* Source Catalog 2.0 (CSC 2.0; Evans et al. 2010).<sup>5</sup> There are a total of 328 *Chandra* sources from CSC 2.0 in our survey region. Note that the source flux information is not yet available for the CSC 2.0 Preliminary Detections List. Of these 328 *Chandra* sources, 201 of them are in CSC 1.1 (Evans et al. 2010). Their 0.5–7 keV band fluxes range from  $3.0 - 1711 \times 10^{-16}$  erg cm $^{-2}$  s $^{-1}$ , with a median value of  $9.7 \times 10^{-15}$  erg cm $^{-2}$  s $^{-1}$ . We use these *Chandra* sources as a means to improve and assess the multiwavelength counterpart identification reliabilities, since *Chandra* has better angular resolution and astrometric accuracy than those of *XMM-Newton*.

## 2.2 Data preparation and background-flare filtering

We use the *XMM-Newton* Science Analysis System (SAS) 16.1.0<sup>6</sup> and HEASOFT 6.21<sup>7</sup> for our data analysis. The *XMM-Newton* Observation Data Files (ODFs) were processed with the SAS tasks EPICPROC (EPPROC and EMPROC for PN and MOS, respectively) to create MOS1, MOS2, PN, and PN out-of-time (OOT) event files for each ObsID. For observations taken in mosaic mode or with unexpected interruptions due to strong background flares, we use the SAS task EMOSAIC\_PREP to separate the event files into individual pseudo-exposures and assign pseudo-exposure IDs. For the mosaic-mode observations, we also determine the sky coordinates of each pseudo-exposure using the AHFRA and AHFDEC values in the attitude files created using the SAS task ATTHKGEN.

<sup>5</sup> We use the CSC Preliminary Detections List <http://cxc.harvard.edu/csc2/pd2/>.

<sup>6</sup> <https://www.cosmos.esa.int/web/xmm-newton/sas-release-notes-1610>.

<sup>7</sup> [https://heasarc.gsfc.nasa.gov/FTP/software/ftools/release/archive/Release\\_Notes\\_6.21](https://heasarc.gsfc.nasa.gov/FTP/software/ftools/release/archive/Release_Notes_6.21).

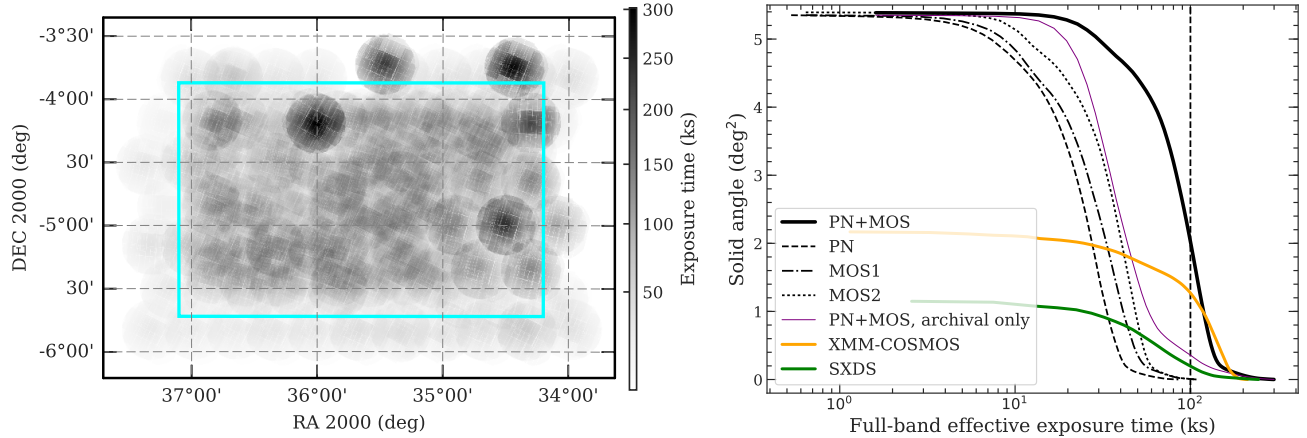


**Figure 3.** *Left* – Full-band survey effective exposure map (PN + MOS). The  $5.3 \text{ deg}^2$  survey region from which the X-ray source catalog is constructed is marked as the cyan rectangular box. Except for several regions with deep *XMM-Newton* follow-up observations of galaxy clusters, the *XMM-Newton* coverage in our survey region is generally uniform. *Right* – The black solid line shows the cumulative survey solid angle as a function of full-band effective (i.e., vignetted) PN+MOS exposure for observations used in this work. Distributions for individual instruments are indicated as the dashed line (PN), dash-dotted line (MOS1), and dotted line (MOS2). For comparison, the cumulative survey solid angle for the archival *XMM-Newton* data in our survey region, in XMM-COSMOS, and in SXDS are shown as the thin purple line, thick orange line, and thick green line, respectively. The dashed vertical line marks exposure time = 100 ks.

For each event file, we create single-event light curves in time bins of 100 s for high (10–12 keV) and low (0.3–10 keV) energies using EVSELECT to search for time intervals without significant background flares (the “good time intervals”, GTIs). We first remove time intervals with 10–12 keV count rates exceeding  $3\sigma$  above the mean, and then repeat the  $3\sigma$  clipping procedure for the low-energy light curves. Since background flares usually manifest themselves as a high-count-rate tail in addition to the Gaussian-shape count-rate histogram, adopting the  $3\sigma$  clipping rule can effectively remove the high-count-rate tail while retaining useful scientific data. For a small number of event files with intense background flares, we filter the event files using the nominal count-rate thresholds suggested by the *XMM-Newton* Science Operations Centre.<sup>8</sup> We exclude 12 pointings with  $\text{GTI} < 2 \text{ ks}$  from our analysis. A total of 2.7 Ms (2.3 Ms) of MOS (PN) exposure remains after flare filtering, including 1.1 Ms (0.9 Ms) from AO-15 and 1.6 Ms (1.4 Ms) from the archival data. The flare-filtered median PN exposure time of the full  $5.3 \text{ deg}^2$  survey region is  $\approx 45.8 \text{ ks}$ . For the central  $\approx 4.5 \text{ deg}^2$  region covered by SERVS, the median PN exposure time is 48.5 ks. These values were not corrected for vignetting.

After screening for background flares, we further exclude events in energy ranges that overlap with the instrumental background lines (Al K $\alpha$  lines at 1.45–1.54 keV for MOS and PN, which usually accounts for  $\approx 10\%$  of the mean counts<sup>9</sup>; Cu lines at 7.2–7.6 keV and 7.8–8.2 keV for PN, which accounts for 30% of the 2–10 keV counts<sup>10</sup>).

From the flare-filtered, instrumental-line-removed event files, we construct images with a commonly adopted  $4''$

pixel size using EVSELECT in the following bands: 0.5–2 keV (soft), 2–10 keV (hard), and 0.5–10 keV (full). For each image, we generate exposure maps with and without vignetting corrections using the SAS task EEXPMAP. We set USEFASTPIXELIZATION=0 and ATTREBIN=0.5 in order to obtain more accurate exposure maps. The exposure maps without vignetting-corrections are only used for generating maps of the instrumental background, which is not affected by vignetting (see §3). Detector masks were also generated using the SAS task EMASK. The distribution of vignetting-corrected exposure values across the XMM-LSS field and the PN+MOS1+MOS2 exposure map are presented in Fig. 3.

### 3 THE MAIN X-RAY SOURCE CATALOG

#### 3.1 First-pass source detection and astrometric correction

The astrometric accuracy of *XMM-Newton* observations can be affected by the pointing uncertainties of *XMM-Newton*. This uncertainty is usually smaller than a few arcsec, but can be as large as  $\approx 10''$  (e.g., Cappelluti et al. 2007; Watson et al. 2008; Rosen et al. 2016). To achieve better astrometric accuracy and to minimize any systematic offsets between different *XMM-Newton* observations, we run an initial pass of source detection for each observation and then use the first-pass source list to register the *XMM-Newton* observations onto a common WCS frame. The first-pass source detection methods are outlined below:

- (i) For the exposures taken by each of the three instruments for each observation, we generate a temporary source list using the SAS task EWAVELET with a low likelihood threshold (THRESHOLD=4). EWAVELET is a wavelet-based algorithm that runs on the count-rate image generated using the image and vignetting-corrected exposure map extracted as described in §2.2.

<sup>8</sup> <https://www.cosmos.esa.int/web/xmm-newton/sas-thread-epic-filterbackground>

<sup>9</sup> [https://xmm-tools.cosmos.esa.int/external/xmm\\_user\\_support/documentation/uhb/epicintbkgd.html](https://xmm-tools.cosmos.esa.int/external/xmm_user_support/documentation/uhb/epicintbkgd.html).

<sup>10</sup> Ranalli et al. (2015).

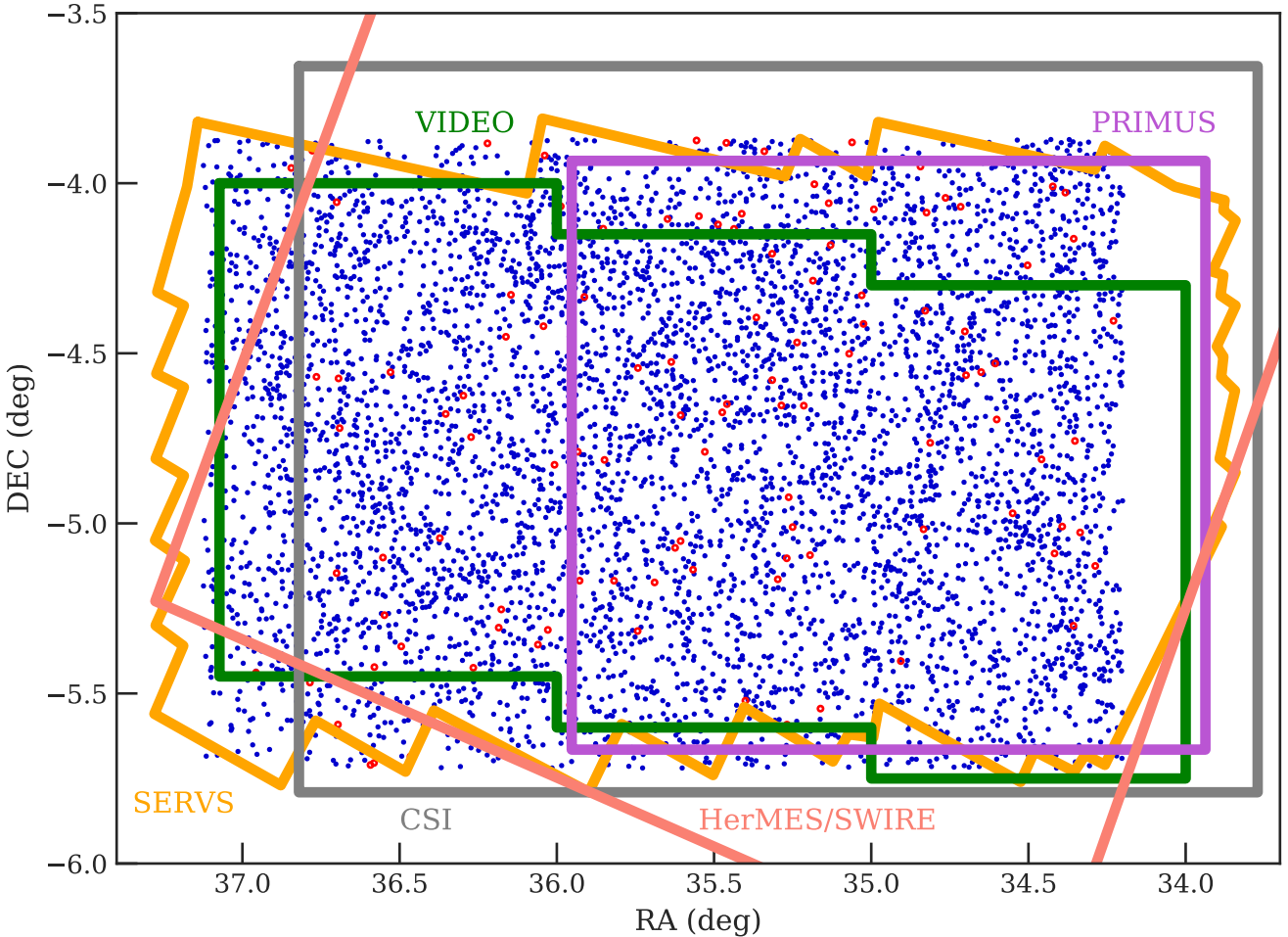


**Figure 4.** Spatial distribution of the 5242 sources detected in this work. We have identified reliable multiwavelength counterparts (see Sec. 4.1 and Sec. 4.2 for details) for 98% of the *XMM-Newton* sources (blue dots), while the remaining 2% of sources are marked as open red circles. Some of the multiwavelength coverage of the XMM-LSS field is also shown as labeled (see §4 for details).

- (ii) We use the temporary source list as an input to generate background images using the SAS task ESPLINEMAP with METHOD=MODEL. This option fits the source-excised image with two templates: the vignetted exposure map, and the un-vignetted exposure map. The former represents the cosmic X-ray background with an astrophysical origin, while the latter represents the intrinsic instrumental noise. ESPLINEMAP then finds the best-fit linear combination of the two templates and generates a background map. The details of this method are described in Cappelluti et al. (2007). The background maps are used for the PSF-fitting based source detection task described in Step (iv).
- (iii) We run EWAVELET again for each observation. This time the source list is generated by running EWAVELET on the exposure map and image coadded across the PN, MOS1, and MOS2 exposures (when available) with the default likelihood threshold (THRESHOLD=5).
- (iv) For each EWAVELET source list, we use the SAS task EMLDETECT to re-assess the detection likelihood and determine the best-fit X-ray positions. EMLDETECT is a PSF-fitting tool which performs maximum-likelihood fits to the input source considering the *XMM-Newton* PSF, exposure values, and background levels of the input source on each image.

EMLDETECT also convolves the PSF with a  $\beta$ -model brightness profile<sup>11</sup> for clusters and uses the result to determine if the input source is extended. Instead of running on the co-added image, EMLDETECT takes the image, exposure map, background map, and detector mask of each input observation into account. We use a stringent likelihood threshold (LIKMIN= 10.8) to ensure that astrometric corrections are calculated based on real detections, and we only keep the point sources.

- (v) For the mosaic-mode observations (see Footnote 2), the multiple pointings under the same ObsID were already registered on the same WCS frame of the ObsID. Therefore, we do not correct the astrometry for each pseudo-exposure but only consider the astrometric offsets on an ObsID-by-ObsID basis. The source lists for the mosaic-mode observations were generated using the SAS task EMOSAIC\_PROC, which is a mosaic-mode wrapper for procedures similar to (i)-(iv) described above.

For steps (iv) and (v), the source searching was con-

<sup>11</sup> <http://xmm-tools.cosmos.esa.int/external/sas/current/doc/emdletect/node3.html>.

ducted simultaneously on the images of the three EPIC cameras as the astrometric offsets between PN, MOS1, and MOS2 are negligible. For each ObsID, we cross-correlate the high-confidence EMLDETECT list of point sources (with the EMLDETECT flag EXT= 0) with the optical source catalog culled from the Hyper Suprime-Cam Subaru Strategic Program Public Data Release 1 (HSC-SSP; Aihara et al. 2017), which is an ultra-deep optical photometric catalog with sub-arcsec angular resolution. The astrometry of HSC-SSP is calibrated to the Pan-STARRS1  $3\pi$  survey and has a  $\lesssim 0.05''$  astrometric uncertainty. More details of the HSC-SSP catalog can be found in Aihara et al. (2017), and it is also briefly discussed in §4. For astrometric corrections, we limit the optical catalog to HSC sources with  $i = 18 - 23$  to minimize possible spurious matches due to large faint source densities at  $i > 23$  and matches to bright stars that might have proper motions or parallaxes.

The offset between each ObsID and the HSC catalog is calculated based on a maximum-likelihood algorithm similar to the SAS task EPOSCORR. The major difference between our approach and EPOSCORR is that we use an iterative optimization approach compared to the grid-searching algorithm adopted by EPOSCORR. During each iteration, we cross-correlate the optical catalog with the X-ray catalog using a  $10''$  search radius and exclude all matches with multiple counterparts (less than 5% of our X-ray sources have more than one optical counterpart in the bright HSC-SSP catalog). We then calculate the required astrometric corrections that maximize the cross-correlation likelihood. After each iteration, we apply the best-fit astrometric offsets to the source list and next repeat the catalog cross-correlation steps and re-calculate the required additional corrections for the source list. The required astrometric corrections usually converge after 1–2 iterations. For the purpose of frame correction, we adopt the X-ray positional uncertainties calculated based on the PSF-fitting likelihood ratios provided by EMLDETECT ( $\sigma_{eml}$  hereafter). The positional uncertainty information is necessary because the required astrometric corrections should be weighted toward X-ray sources with better positions within each observation. To avoid over-weighting sources with extremely small  $\sigma_{eml}$ , we also include a constant  $0.5''$  systematic uncertainty when calculating the best-fit values for frame-correction.<sup>12</sup> The median number of X-ray sources in an ObsID with only one HSC counterpart within  $3''$  is 32.

The required frame-correction offsets calculated using our approach are less than  $3''$  in both RA and DEC and are generally consistent with the results calculated using EPOSCORR, with a median difference of  $0.1''$ . For two obsIDs the difference between our offsets and the EPOSCORR offsets are non-negligible ( $> 0.5''$ ). We visually inspect the **X-ray to optical angular offsets** of these ObsIDs and conclude that our approach does improve the alignments between the optical and corrected X-ray images. The event files and the attitude file for each ObsID are then projected onto the WCS frame of the HSC catalog by updating the relevant keywords using a modified version of *Chandra*'s ALIGN\_EVT routine (Ranalli et al. 2013). Since the sky coordinates for

the event files of the mosaic-mode pseudo-pointings are derived based on the reference point centered at the nominal RA and DEC positions of the mosaic-mode ObsIDs, we also recalculate the sky coordinates for these event files with the SAS task ATTCALC using the true pointing positions as the reference point, which is necessary for using regular SAS tasks for mosaic-mode pseudo-exposures.

### 3.2 Second-pass source detection

We re-create images, exposure maps, detector masks, and background maps using the frame-corrected event files and attitude files. We then run source-detection tasks for the second time considering all *XMM-Newton* observations listed in Table 2. Similar to the approach used for the XMM-H-ATLAS survey (Ranalli et al. 2015), we divide the XMM-LSS field into a grid when running the second-pass source detection because the number of images that can be processed by a single EMLDETECT thread is limited. We use a custom-built wrapper of relevant SAS tasks to carry out the second-pass source detection, which is similar to the GRIDDETECT<sup>13</sup> tool built for the XMM-H-ATLAS survey (Ranalli et al. 2015).

The cell sizes of the grid are determined by the number of EWAVELET sources. For each cell in the grid, we co-add the images and exposure maps for all observations with footprint inside the cell and run EWAVELET with a low detection threshold<sup>14</sup> on the co-added image and exposure map. For each cell, we only keep EWAVELET sources within the RA/DEC range of the cell plus  $1'$  “padding” on each side of the cell. We then use the EWAVELET list as an input for EMLDETECT to assess the detection likelihood. The EMLDETECT point-source list of the full XMM-LSS region is constructed from the union of the sources from all cells after removing duplicates due to the “padding”. We search for sources in three different bands: 0.5–2 keV (soft), 2–10 keV (hard), and 0.5–10 keV (full). For each source, EMLDETECT computes a detection likelihood DET<sub>ML</sub>, which is defined as  $DET_{ML} = -\ln P$ , where  $P$  is the probability  $P$  of a detected source being a random Poisson fluctuation of the background. In practice, the spurious fractions of a source catalog derived based on simulations are known to differ from the values obtained with the simple  $DET_{ML} = -\ln P$  equation (e.g., Cappelluti et al. 2007, 2009; Ueda et al. 2008; Watson et al. 2008; LaMassa et al. 2016). Since the source catalog is constructed based a complex multi-stage source-detection approach, the relation between DET<sub>ML</sub> and the true spurious fraction may not be as straightforward as the simple  $DET_{ML} = -\ln P$  equation, especially in the low source count regime where even this simple relation breaks.<sup>15</sup> Therefore, we do not adopt a single DET<sub>ML</sub> value for our source catalog. Instead, we use the DET<sub>ML</sub> value corresponding to the 1% spurious fraction determined by simulations for each band (see the next subsection, §3.3, for details). The

<sup>12</sup> We assume the systematic uncertainties to be  $0.5''$  as suggested by Watson et al. (2008).

<sup>13</sup> <https://github.com/piero-ranalli/griddetect>.

<sup>14</sup> THRESHOLD=4.

<sup>15</sup> See <http://xmm-tools.cosmos.esa.int/external/sas/current/doc/emldetect.pdf>.

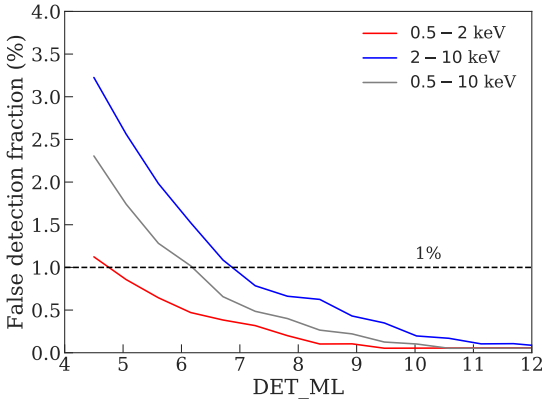


**Figure 5.** The fraction of spurious sources detected at different DET\_ML based on simulations. The detection thresholds relevant to our catalog are marked as the vertical dashed lines.

DET\_ML thresholds with 1% spurious fraction are 4.8, 7.8, and 6.2 for the soft, hard, and full bands, respectively. A total of 5242 sources satisfy this criterion in at least one of the three bands (see §3.5). We show the spatial distribution of the 5242 detected sources in Fig. 4.

### 3.3 Monte Carlo simulation

To assess our survey sensitivity and catalog reliability, we perform Monte Carlo simulations of X-ray observations. For each simulation, we generate a list of mock X-ray sources by sampling from the  $\log N - \log S$  relations reported in the XMM-COSMOS survey (Cappelluti et al. 2009, for the 0.5–2 keV and 2–10 keV bands) and the Chandra Multi-wavelength Project survey (ChaMP; Kim et al. 2007, for the 0.5–10 keV band). The maximum flux of the mock X-ray catalogs is set at  $10^{-11}$  erg cm $^{-2}$  s $^{-1}$ . The minimum flux of the mock X-ray sources at each energy band is set as 0.5 dex lower than the minimum detected flux (e.g., LaMassa et al. 2016). We randomly place the mock X-ray sources in the RA/DEC range covered by the *XMM-Newton* observations used in this work. We then use a modified version of the simulator written for the *XMM-Newton* survey of the CDF-S (Ranalli et al. 2013), CDFS-SIM,<sup>16</sup> to create mock event files. CDFS-SIM converts X-ray fluxes to PN and MOS count rates with the same model used for deriving the ECFs, and it then randomly places X-ray events around the source location according to the count rates, the *XMM-Newton* PSFs at the given off-axis angle, and the real exposure maps. We extract images from the simulated event files using the same methods described in §3. For each observation, the simulated image is combined with a simulated background, which is created by re-sampling the original background map according to Poisson distributions to create simulated images that mimic the real observations. For each energy band, a total of 20 simulations are created. We run the same two-stage source-detection procedures described in

§3.2 on the simulated data products. For each simulation, we match the detected sources to the input sources within a 10'' cut-off radius by minimizing the quantity  $R^2$ :

$$R^2 = \left( \frac{\Delta\text{RA}}{\sigma_{\text{RA}}} \right)^2 + \left( \frac{\Delta\text{DEC}}{\sigma_{\text{DEC}}} \right)^2 + \left( \frac{\Delta\text{RATE}}{\sigma_{\text{RATE}}} \right)^2. \quad (1)$$

Here  $\Delta\text{RA}$  and  $\Delta\text{DEC}$  are the differences between the simulated RA/DEC positions and the RA/DEC positions obtained by running source detection on the simulated images.  $\Delta\text{RATE}$  is the difference between the simulated count rates and the detected count rates.  $\sigma_{\text{RA}}$ ,  $\sigma_{\text{DEC}}$ , and  $\sigma_{\text{RATE}}$  are the uncertainties of RA, DEC, and count rates of the detected sources. Minimizing  $R^2$  takes into account the flux and positional differences between the input catalog and the sources detected in the simulated images (e.g., Cappelluti et al. 2007; Ranalli et al. 2015). Detected sources without any input sources within the 10'' radius are considered to be spurious detections.

Fig. 5 presents the spurious fraction ( $f_{\text{spurious}}$ ) as a function of DET\_ML for the soft, hard, and full bands. For our catalog, we consider sources with  $f_{\text{spurious}}$  smaller than 1% to be reliably detected. At this threshold, the corresponding DET\_ML are 4.8, 7.8, and 6.2 for the soft, hard, and full bands, respectively. The difference between the DET\_ML thresholds in the three bands are likely due to their different background levels. For the full X-ray source catalog of 5242 sources, the  $f_{\text{spurious}} = 1\%$  translates to  $\approx 52$  spurious detections. For each source, we have also calculate a detection reliability parameter (defined as  $1 - f_{\text{spurious}}$ ) for each band using the simulation results presented in Fig. 5, which could be used for selecting sources with a desired reliability.

We also test for source confusion following the methods described in Hasinger et al. (1998); Cappelluti et al. (2007). For all the simulated sources that are detected, we consider sources with observed fluxes ( $S_{\text{out}}$ ) that are larger than the simulated fluxes ( $S_{\text{in}}$ ) by the following threshold to be “confused” sources:  $S_{\text{out}}/(S_{\text{in}} + 3 \times S_{\text{out}}^{\text{err}}) > 1.5$ . Here  $S_{\text{out}}^{\text{err}}$  is the statistical fluctuation of the observed fluxes. The source confusion fractions are 0.14%, 0.16%, and 0.43% in the soft, hard, and full bands, respectively. For the 5242 X-ray sources in this catalog, these fractions translate to  $\approx 7 - 22$  sources with confusion.

### 3.4 Astrometric accuracy

We investigate the positional accuracy of the *XMM-Newton* sources by comparing the second-pass X-ray catalog with the HSC-SSP catalog. Similar to the frame-correction procedures described in §3.1, we search for unique optical counterparts around the X-ray positions using a 3'' search radius. For the 5199 X-ray sources detected in the full-band during the second-pass source-searching process, a total of 2434 X-ray sources are found to have only one  $i = 18 - 23$  HSC counterpart within 3''. We use the separations between the optical and X-ray positions of this subsample as a means to determine empirical X-ray positional uncertainties, which is a commonly adopted practice in X-ray surveys (e.g. Watson et al. 2008; Luo et al. 2010; Xue et al. 2011; Xue et al. 2016; Luo et al. 2017).

The X-ray positional accuracy is determined by how

<sup>16</sup> <https://github.com/piero-ranalli/cdfs-sim>

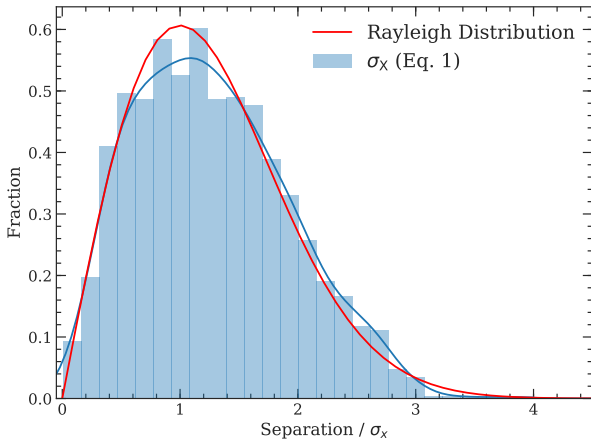


**Figure 6.** Histograms of the normalized full-band positional offsets, a dimensionless quantity defined as the positional offsets normalized by the empirically derived positional uncertainty, and comparison with the expected Rayleigh distribution, the solid red curve. The kernel-density estimation of the normalized positional offset distribution is shown as the solid blue curve. The excellent agreement between the two distributions suggests that our empirically derived  $\sigma_x$  values are reliable indicators of the true positional uncertainties.

well the PSF-centroid location can be measured, which usually depends on the number of counts of the detected source and the PSF size of the instrument (primarily dependent on the off-axis angle). For the vast majority of the X-ray sources presented in this work, the detected photons are from at least three different observations, and hence the dynamical range of effective off-axis angle for each source detected on the coadded image is relatively small. Thus, the X-ray positional uncertainty is mostly dependent on the number of counts available for detected sources. Using the angular separations between the 2434 X-ray sources and their unique optical counterparts, we derive an empirical relation between the number of X-ray counts,  $C$ ,<sup>17</sup> and the 68% positional-uncertainty radius ( $r_{68\%}$ ) for the full-band-detected X-ray sources,  $\log_{10} r_{68\%} = -0.31 \times \log_{10} C + 0.85$ . The parameters are chosen such that 68% of the sources have positional offsets smaller than the empirical relation.

For this work, we define the X-ray positional uncertainty,  $\sigma_x$ , to be the same as the uncertainties in RA and DEC where  $\sigma_{RA} = \sigma_{DEC} = \sigma_x$ . Under this definition,  $\sigma_x$  is  $r_{68\%}$  divided by a factor of 1.515 (e.g., Eq. 21 and §4.2 of Pineau et al. 2017). The factor 1.515 is determined by integrating the Rayleigh distribution until the cumulative probability reaches 0.68. For reference, 90%, 95%, and 99.73% uncertainties correspond to  $2.146\sigma_x$ ,  $2.448\sigma_x$ , and  $3.439\sigma_x$ , respectively. Because the separations in both RA and DEC behave as a univariate normal distribution with  $\sigma_{RA}$  and  $\sigma_{DEC}$ , respectively,<sup>18</sup> the angular separation should therefore follow the joint probability distribution function of the

<sup>17</sup> An upper limit of 2000 is set on  $C$  because the improvement of positional accuracy is not significant for larger source counts (e.g., Luo et al. 2017).

<sup>18</sup> Here we consider the positional uncertainties of the HSC-SSP catalog to be negligible compared to the *XMM-Newton* positional uncertainties.

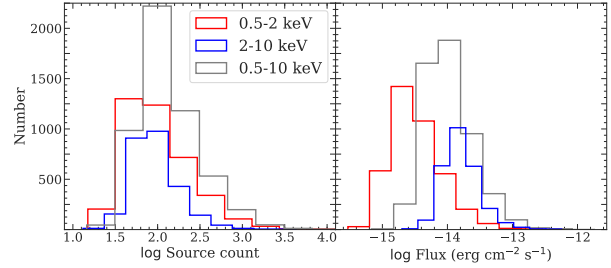


**Figure 7.** *Left* – Source-count distributions for the sources detected in the soft (red), hard (blue), and full (gray) bands. *Right* – Flux distributions of the sources detected in the three bands. Colors are the same as in the left panel.

uncertainties in the RA and DEC directions. Since we assume  $\sigma_{RA} = \sigma_{DEC}$ , the angular separation between an optical source and an X-ray source should follow the univariate Rayleigh distribution with the scaling parameter  $\sigma_x$ , where  $\sigma_x = \sigma_{RA} = \sigma_{DEC}$  (see §4 of Pineau et al. 2017, for details).

For each energy band, we repeat the same process to find the best-fit relation for  $\sigma_x$  using the following equation:

$$\log_{10} \sigma_x = \alpha \times \log_{10} C + \beta. \quad (2)$$

Given the PSF size and positional accuracy of *XMM-Newton*, it is possible for X-ray sources to have angular separation from optical sources larger than  $3''$ , and the positional uncertainties derived based on counterparts found within the  $3''$  search radius can be underestimated. Therefore, we adopt an iterative process. For each iteration, we use the derived  $\sigma_x$  to identify reliable matches using the likelihood-ratio matching method described in §4.1. We then re-derive Eq. 2 using the reliable matches, and the updated astrometric uncertainties are used for running likelihood-ratio matching again. This is a stable process, as the parameters converge after 2–3 iterations. The average positional uncertainties ( $\sigma_x$ ) for our soft-band, hard-band, and full-band X-ray catalogs are  $1.^{\circ}35$ ,  $1.^{\circ}37$ , and  $1.^{\circ}31$ , respectively. Fig. 6 presents a comparison of the normalized separation (Separation/ $\sigma$ ) between the full-band X-ray sources and their bright optical counterparts with  $\sigma$  derived using Eq. 2,  $\sigma_x$ . The agreement between the Rayleigh distribution and the Separation/ $\sigma_x$  distribution of our sample demonstrates that our empirically derived  $\sigma_x$  values are reliable indicators of the true positional uncertainties. As for  $\sigma_{eml}$ , previous studies have reported that some on-axis sources with large numbers of counts can have unrealistically low  $\sigma_{eml}$  values, therefore an irreducible systematic uncertainty should be added to  $\sigma_{eml}$  for the normalized separation to follow a Rayleigh distribution (e.g., Watson et al. 2008), but the nature of this systematic uncertainty remains unclear. For this work, we use  $\sigma_x$  as the positional uncertainties of our X-ray catalog, but  $\sigma_{eml}$  is also included in the final catalog for completeness.

### 3.5 The main X-ray source catalog

We detect 3988, 2618, and 5199 point sources with  $f_{\text{spurious}} \leq 1\%$  in the 0.5–2 keV, 2–10 keV, and 0.5–10 keV bands, respectively. The details of the main X-ray source catalog are reported in Table A of Appendix A.

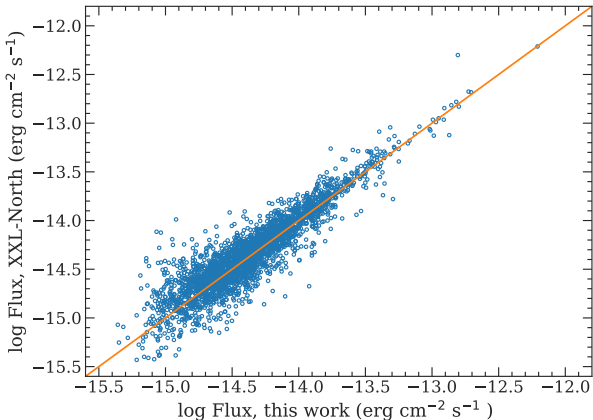


**Figure 8.** Comparison of the soft-band X-ray fluxes of our X-ray sources and those of the *XMM-Newton* counterparts identified in the XMM-XXL-North source catalogs (Liu et al. 2016) within a  $10''$  radius. As expected, almost all of the XMM-XXL-North X-ray sources in our catalog region can be matched to a counterpart in our X-ray source catalog with comparable flux.

The extended sources (identified by the  $\text{EXT} > 0$  flag of EMLDETECT) are not included, as the properties of the extended X-ray emission are beyond the scope of this work.<sup>19</sup> We combine catalogs from the three energy bands using a similar approach to that adopted by the *XMM-Newton* Serendipitous Source Catalogue. We consider two sources from different catalogs to be the same if their angular separation is smaller than any of the following quantities: (1)  $10''$ , (2) distance to the nearest-neighbor in each catalog, or (3) quadratic sum of the 99.73% positional uncertainties from both bands. The final source catalog is the union of the sources detected in the three energy bands. We check for potential duplicate sources by visually inspecting all sources with distance to the nearest-neighbor ( $\text{DIST\_NN}$ ) less than  $10''$ , and only one set of sources is found to be duplicated, resulting in a total of 5242 unique sources. There are 2967 sources with more than 100 PN+MOS counts in the full-band, and 126 sources with more than 1000 X-ray counts. A unique X-ray source ID is assigned to each of the 5242 sources at this stage. Visual inspection of the image in each band suggests that no apparent sources were missed by our detection algorithm.

We also derive the count rate (vignetting-corrected) to flux energy conversion factors (ECFs) assuming a power-law spectrum with photon index  $\Gamma = 1.7$ , which is typical for distant X-ray AGNs found in *XMM-Newton* surveys with comparable sensitivities (e.g., XMM-COSMOS, Mainieri et al. 2007 and XMM-H-ATLAS, Ranalli et al. 2015) and Galactic absorption,  $N_{\text{H}} = 3.57 \times 10^{20} \text{ cm}^{-2}$ . The energy ranges are those where the removed instrumental lines are excluded when deriving the ECFs. Since the archival observations and the AO-15 observations were carried out in different epochs between 2000–2017, we compute the ECFs by including the slight

<sup>19</sup> There are 68, 11, and 77 sources identified as  $\text{EXT} > 0$  by EMLDETECT in the 0.5–2 keV, 2–10 keV, and 0.5–10 keV bands, respectively. The properties of the extended sources will be reported in a separate work.

temporal variations in the EPIC instrumental calibrations into account. In detail, we make use of the canned response files of 14 different epochs for MOS and 3 different epochs for PN available at the *XMM-Newton* SOC website.<sup>20</sup> The effective ECF for each detected source is the exposure-time-weighted average of all relevant observations. For all X-ray sources, the mean conversion factors for (PN, MOS1, MOS2) are  $(6.23, 1.78, 1.76)$ ,  $(1.15, 0.43, 0.43)$ , and  $(2.84, 0.88, 0.87)$   $\text{counts s}^{-1}/10^{-11} \text{ erg cm}^{-2} \text{ s}^{-1}$ , in the 0.5–2 keV, 2–10 keV, and 0.5–10 keV bands, respectively. We note that temporal variations in the ECFs are  $< 1\%$  for all three bands (e.g., Mateos et al. 2009; Rosen et al. 2016). For each source detected by EMLDETECT, the flux from each EPIC camera is calculated separately using the corresponding ECF. The final flux of the source is the error-weighted mean of the fluxes from the three EPIC cameras, when available. The median fluxes for the soft, hard, and full bands are  $2.9 \times 10^{-15}$ ,  $1.5 \times 10^{-14}$ , and  $9.4 \times 10^{-15} \text{ erg cm}^{-2} \text{ s}^{-1}$ , respectively. The source-count and flux distributions of the sources detected in the three energy bands are displayed in Fig. 7.

For sources that are detected in fewer than three bands, we calculate the source-count upper limits using the mosaicked background map of the band in which the source is not detected. The mosaicked background map of each band is generated by summing the background maps from all individual observations (see §3.1). According to the Poisson probability set by the EMLDETECT detection likelihood threshold ( $P_{\text{Random}}$ , the probability of the detected source being a random Poisson fluctuation due to the background), we can calculate the minimum required total counts ( $m$  in the following equation) required to exceed the expected number of background counts,  $B$ , using the regularized upper incomplete  $\Gamma$  function (which is equivalent to Eq. 2 of Civano et al. 2016 if  $m$  is a positive integer):

$$P_{\text{Random}} = \frac{1}{\Gamma(m)} \int_B^\infty t^{m-1} e^{-t} dt \quad (3)$$

The upper limits are those corresponding to the DET\_ML values with a 1% spurious fraction:  $P_{\text{Random}} = 8.2 \times 10^{-3}$  for the soft band,  $P_{\text{Random}} = 4.1 \times 10^{-4}$  for the hard band, and  $P_{\text{Random}} = 2.0 \times 10^{-3}$  for the full band. For each non-detected source in each band, we determine the background counts by summing the background map within the circle with 70% encircled energy fraction (EEF). We then calculate  $m$  by solving Eq. 3 using the SCIPY function SCIPY.SPECIAL.GAMMAINCINV.<sup>21</sup> Since  $m$  is the required total counts to exceed random background fluctuations at the given probability, the flux upper limit is calculated based on the following equation, which is similar to Equation 2 of Cappelluti et al. (2009) and Equation 2 of Civano et al. (2016):

$$S = \frac{m - B}{t_{\text{exp}} \times \text{EEF} \times \text{ECF}} \quad (4)$$

<sup>20</sup> <https://www.cosmos.esa.int/web/xmm-newton/epic-response-files>.

<sup>21</sup> This quantity is the inverse function of Eq. 2.

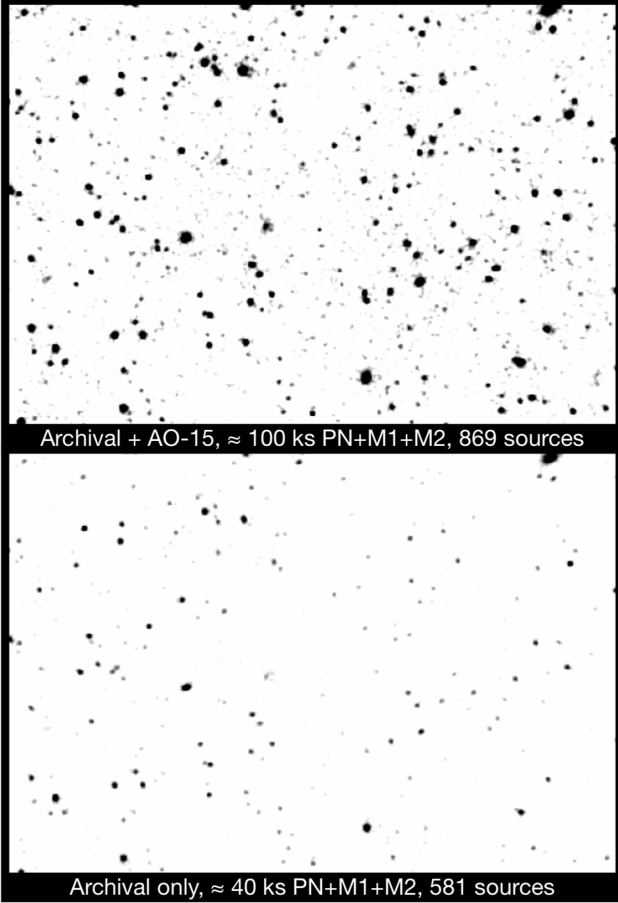


**Figure 9.** *Top* – Background-subtracted, smoothed, and coadded PN+MOS image in the 0.5–10 keV band for a  $0.8 \times 0.6 \text{ deg}^2$  region centered at  $\text{RA}=35.580^\circ$ ,  $\text{DEC}=-4.965^\circ$ . This image is created using both archival data and the new AO-15 data, and a total of 869 sources are detected in this region. *Bottom* – Same as the top image, but only the archival data are included. The two images are matched in color scale. In the Liu et al. (2016) catalog, only 581 sources can be found in this region. The typical vignetting-corrected exposure times are shown at the bottom of both panels. The exposure time of the full survey region is shown in Fig. 3.

Here EEF corrects for PSF loss and is 0.7, and  $t_{\text{exp}}$  is the median exposure time within the 70% EEF circle. The flux upper limits are calculated as the exposure-time-weighted mean of the three EPIC detectors.

For each source detected in either the soft or the hard band (or both), we calculate its hardness ratio (HR), defined as  $(H-S)/(H+S)$ , where  $H$  and  $S$  are the source counts weighted by the effective exposure times in the hard and the soft bands, respectively. For sources not detected in either the soft or the hard band, we assign their HR as  $-1$  (hard-band non-detection) or  $+1$  (soft-band non-detection). The source counts are the default output of EMLDETECT, which is the sum of the counts from all three EPIC detectors. We report this value in our catalog for direct comparison with previous studies. The uncertainties on HR are calculated based on the count uncertainties from the output of EMLDETECT using the error propagation method described in §1.7.3 of Lyons (1991).

As a comparison, a total of 2861 X-ray sources from

**Table 3.** Sensitivity curves. Column 1: Soft-band flux. Column 2: Soft-band survey solid angle. Columns 3–4: Similar to Columns 1–2 but for the hard band. Columns 5–6: Similar to Columns 1–2 but for the full band. This table is available in its entirety online.

$\log S_{0.5-2\text{keV}}$ (cgs)	$\Omega_{0.5-2\text{keV}}$ (deg $^2$ )	$\log S_{2-10\text{keV}}$ (cgs)	$\Omega_{2-10\text{keV}}$ (deg $^2$ )	$\log S_{0.5-10\text{keV}}$ (cgs)	$\Omega_{0.5-10\text{keV}}$ (deg $^2$ )
(1)	(2)	(3)	(4)	(5)	(6)
-14.78	4.828	-13.93	4.652	-14.38	3.421
-14.77	4.862	-13.92	4.694	-14.37	3.583
-14.76	4.898	-13.91	4.737	-14.36	3.727
-14.75	4.931	-13.90	4.778	-14.35	3.855
-14.74	4.960	-13.89	4.815	-14.34	3.976
-14.73	4.991	-13.88	4.852	-14.33	4.081
-14.72	5.016	-13.87	4.885	-14.32	4.182
-14.71	5.044	-13.86	4.918	-14.31	4.262

XMM-XXL-North (Liu et al. 2016) are found to have a counterpart within the  $10''$  radius in our X-ray catalog.<sup>22</sup> For these matched sources, we show a comparison between the soft-band X-ray fluxes reported in the XMM-XXL-North catalog and those in our catalog in Fig. 8. As expected, the majority of the archival sources detected in our catalog have archival soft-band fluxes consistent to those in our catalog. The small scatter in the measured fluxes is expected as the XMM-XXL-North catalog adopts a different source-detection method, background-subtraction approach, and energy conversion factors. Since the SXDS observations were also used for constructing the XXL-North (Liu et al. 2016) catalog, the 2861 sources matched to the XMM-XXL-North catalogs are considered to be matched to all available archival sources, and we conclude that the other 2381 X-ray sources in our catalogs are new sources. We include the IDs from the Liu et al. (2016) catalog for these matched objects in our source catalog (Table A). In our source-detection region, 172 sources from the original (Liu et al. 2016) catalog do not have a counterpart in our point-source catalog. Of these 172 sources, 150 can be associated with the extended sources or **sources deemed unreliable based on our DET\_ML criteria** (see §3.3). The remaining sources comprise  $< 1\%$  of the XMM-XXL-North catalog in our source-detection region. Visual inspection suggests that the vast majority of these sources might be spurious detections, but we cannot rule out the possibility that some sources are missed in our catalog due to X-ray variability (e.g., Yang et al. 2016; Falocco et al. 2017; Paolillo et al. 2017; Zheng et al. 2017). Also, the XMM-XXL-North catalog adopted a different source-detection approach (see §2 of Liu et al. 2016 for details). The properties of sources that exhibit strong X-ray variability will be presented in a separate work. Fig. 9 shows the background-subtracted, 0.5–10 keV PN+MOS image (see §3 for the details of the data analysis) from a  $\approx 0.5 \text{ deg}^2$  region in XMM-LSS generated using the combined AO-15 and archival data. An image produced using only the archival data is also displayed for comparison, demonstrating the improved source counts with the additional AO-15 observations.

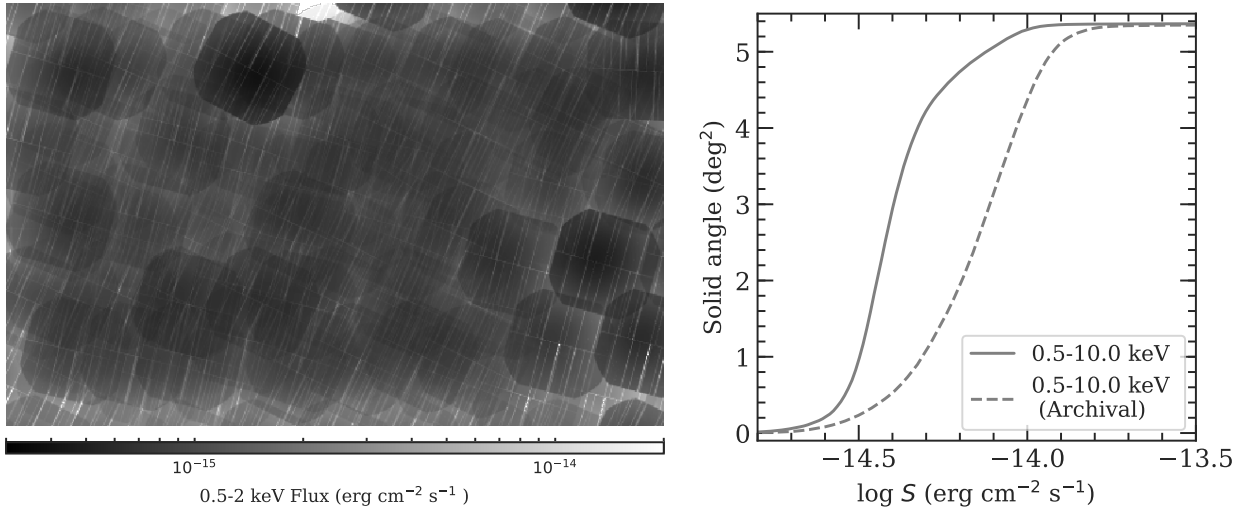


**Figure 10.** *Left* – Soft-band sensitivity map of the source-detection region (the same as the cyan box shown in Fig. 3). *Right* – Comparison of the full-band sky coverages between this work (solid line) and the archival *XMM-Newton* observations (dashed line), demonstrating the improved and more uniform sensitivity across the wide field enabled by the new data.

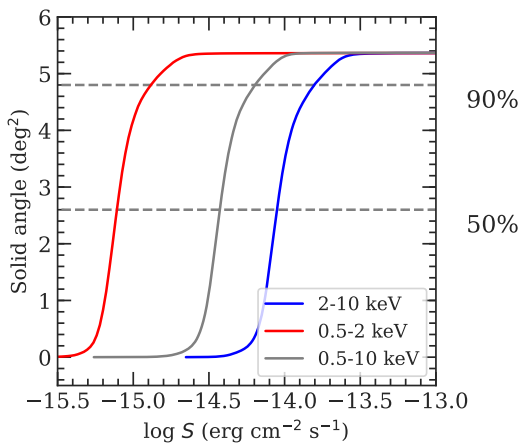


**Figure 11.** Sky coverage in the soft, hard, and full bands of our X-ray survey in XMM-LSS. The sensitivity curves were calculated with DET $_ML$ = 4.8, 7.8, and 6.2 for the soft, hard, and full bands. These DET $_ML$  values correspond to 1% spurious fraction based on extensive simulations (see §3.3.)

### 3.6 Survey sensitivity, sky coverage, and $\log N - \log S$

We create sensitivity maps of our survey region in different bands using the background and exposure maps generated as described in §2.2. The mosaicked background and exposure maps are binned to  $5 \times 5$  pixels ( $20'' \times 20''$ ). For each pixel of the binned, mosaicked background map, the minimum required source counts to exceed the random background fluctuations are calculated using Eq. 3. The sensitivity is then calculated using Eq. 4 with the corresponding EEF and ECF values. According to the sensitivity maps, our survey has flux

limits of  $1.7 \times 10^{-15}$ ,  $1.3 \times 10^{-14}$ , and  $6.5 \times 10^{-15}$  erg cm $^{-2}$  s $^{-1}$  over 90% of its area in the soft, hard, and full bands, respectively, reaching the desired depth-area combination. We also compared the sensitivity maps with the detected sources, and find that the spatial distribution of the fluxes of our sources largely obey the sensitivity maps. The soft-band sensitivity map is presented in Fig. 10-left. We also generated a soft-band sensitivity map using only the archival data. To visualize the improvement upon the archival data, we compare the full-band sky coverage obtained from all available *XMM-Newton* data in our survey region with the sky coverage obtained using only the archival data. Fig. 10-right demonstrates the improved survey depth and uniformity with the new *XMM-Newton* observations. The sensitivity curves corresponding to the DET $_ML$  thresholds in the soft, hard, and full-bands are shown in Fig. 11 and presented in Table 3.

We calculate the  $\log N - \log S$  relations of our survey using the sky coverage curves described above and the following equation:

$$N(>S) = \sum_{i=1}^{N_s} \frac{1}{\Omega_i}. \quad (5)$$

Here  $N(>S)$  represents the total number of detected sources with fluxes larger than  $S$ , and  $\Omega_i$  is the sky coverage associated with the flux of the  $i$ th source. The  $\log N - \log S$  relations of our survey are shown in Fig. 12, along with the  $\log N - \log S$  relations for a selection of surveys spanning a wide range of area and sensitivity (CDF-S 7Ms, Luo et al. 2017; XMM-COSMOS, Cappelluti et al. 2009; COSMOS-Legacy, Civano et al. 2016; and Stripe 82X, LaMassa et al. 2016). The flux differences caused by different choices of power-law indices and/or slight differences in energy ranges have been corrected assuming a  $\Gamma = 1.7$  power-law spectrum adopted in this work. Considering factors such as different spectral models and/or methods of generating survey sensitivity curves, our  $\log N - \log S$  relations are consistent with

<sup>22</sup> The  $10''$  search radius is approximately 3 times the quadratic sum of the largest positional uncertainties in both catalogs.

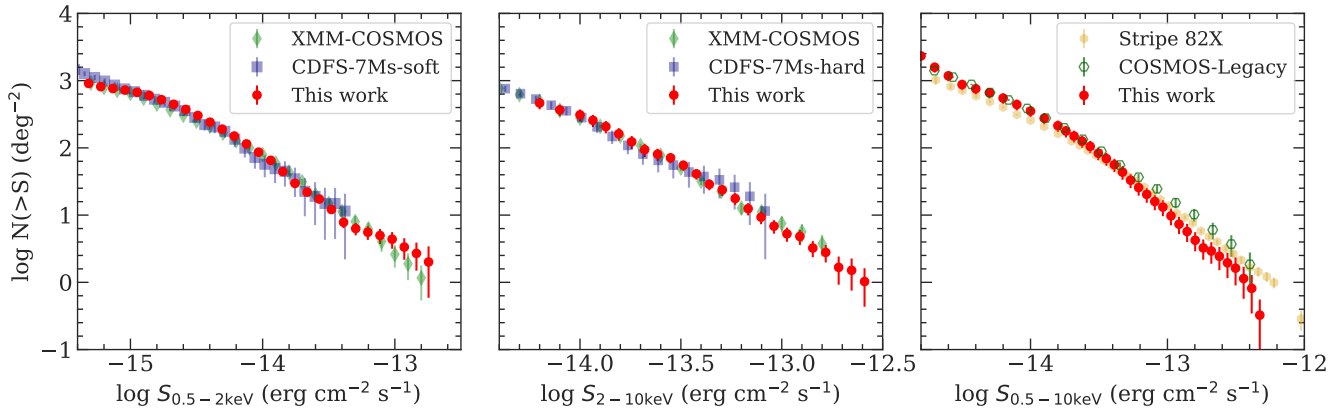


**Figure 12.** The  $\log N - \log S$  relations for our catalog in the soft band (left), hard band (middle), and full band (right). For comparison, a few  $\log N - \log S$  relations from surveys spanning a wide range of area and sensitivity are also shown (XMM-COSMOS, Cappelluti et al. 2009; Stripe-82X, LaMassa et al. 2016; COSMOS-Legacy, Civano et al. 2016; and CDF-S 7Ms, Luo et al. 2017; the energy range and power-law photon index differences have been corrected). The  $\log N - \log S$  relations of our survey are generally consistent with those of previous studies.

the relations reported in the literature within the measurement uncertainties.

#### 4 MULTIWAVELENGTH DATA IN THE XMM-LSS FIELD

The XMM-LSS region is one of the most extensively observed extragalactic fields. The publicly available multiwavelength observations in the XMM-LSS region utilized in this work are SERVS (Mauduit et al. 2012), SWIRE (Lonsdale et al. 2003), VIDEO (Jarvis et al. 2012), the CFHTLS-wide survey (Hudelot et al. 2012), and the HSC-SSP survey (Aihara et al. 2017).

We focus on identifying the correct counterparts for our X-ray sources in four deep optical-to-near-IR (OIR) catalogs: SERVS, VIDEO, CFHTLS, and HSC-SSP. SERVS is a post-cryogenic *Spitzer* IRAC survey in the near-IR 3.6 and 4.5  $\mu\text{m}$  bands with  $\approx 2\mu\text{Jy}$  survey sensitivity limits and  $\approx 5 \text{ deg}^2$  solid-angle coverage in the XMM-LSS region. We make use of the highly reliable two-band SERVS catalog built using SExtractor, obtained from the *Spitzer* Data Fusion catalog (Vaccari 2015), which has  $\approx 4 \times 10^5$  sources. The Spitzer Data Fusion catalog has already integrated data from SWIRE, which include photometry in all four IRAC bands and the photometry in MIPS 24, 70, and 160  $\mu\text{m}$ . A total of 82% of the X-ray sources have at least one SERVS counterpart candidate within their 99.73% positional-uncertainty radius ( $r_{99\%}$  hereafter, which is equivalent to  $3.44\sigma_x$ ), which is calculated based on the quadratic sum of the 99.73% X-ray positional uncertainties and the corresponding OIR positional uncertainties.

VIDEO is a deep survey in the near-infrared  $Z$ ,  $Y$ ,  $J$ ,  $H$ , and  $K_s$  bands with  $\approx 80\%$  completeness at  $K_s < 23.8$ . In the XMM-LSS region, VIDEO covers a  $4.5 \text{ deg}^2$  area ( $\approx 85\%$  of our X-ray survey region) with a total of  $\approx 5.7 \times 10^5$  sources; 79% of the X-ray sources have at least one VIDEO counterpart candidate within  $r_{99\%}$ .

The CFHTLS-W1 survey covers the entirety of our X-ray data, with an 80% completeness limit of  $i' = 24.8$ . We select the CFHTLS sources in the RA/DEC ranges

marginally larger ( $1'$ ) than our source-detection region. We limit the CFHTLS sources to those with  $SNR > 5$  in the  $i'$ -band. The total number of sources in the  $i'$ -band selected catalog is  $\approx 8.1 \times 10^5$ . A total of 90% of the X-ray sources in our catalog have at least one CFHTLS counterpart candidate within  $r_{99\%}$ .

The XMM-LSS field is entirely encompassed by the  $108 \text{ deg}^2$  HSC-SSP wide survey. The limiting magnitude in the  $i$ -band for the wide HSC-SSP survey is 26.4. Inside the XMM-LSS field, HSC-SSP also has “ultra-deep” ( $\approx 1.77 \text{ deg}^2$ ) and “deep” ( $\approx 5 \text{ deg}^2$ ) surveys, which overlap with the SXDS and XMDS regions, respectively. We focus only on the wide survey because in the currently available data release it is only 0.1 mag shallower than the deep survey in the  $i$ -band, and the uniform coverage is important for determining the background source density when matching to the X-ray catalog (see §4.1). We select the  $i$ -band detected HSC-SSP sources in the RA/DEC ranges slightly larger than our source-detection region.<sup>23</sup> The total number of HSC-SSP sources in our source-detection region is  $\approx 3.1 \times 10^6$ , and  $\approx 93\%$  of the X-ray sources in our main catalog have at least one HSC-SSP counterpart candidate within  $r_{99\%}$ .

Although CFHTLS is not as deep as HSC-SSP in the  $g$ ,  $r$ ,  $i$ , and  $z$  bands, it has complementary  $u^*$ -band photometry. Including photometry from both optical surveys also ensures that we will minimize the risk of missing an optical counterpart due to bad photometry caused by artifacts such as satellite tracks in either survey.

Since there are small systematic offsets in the astrometry of each catalog, we match SERVS, VIDEO, and CFHTLS to the HSC-wide catalog, and correct for the small offsets

<sup>23</sup> We select sources with the DETECT\_IS\_PRIMARY and IDETECTED\_NOTJUNK flags set as TRUE, and CENTROID\_SDSS\_FLAGS set as FALSE. According to the HSC-SSP example script for selecting “clean objects”, we also exclude the HSC sources with FLAGS\_PIXEL\_EDGE, FLAGS\_PIXEL\_SATURATED\_CENTER, FLAGS\_PIXEL\_CR\_CENTER, FLAGS\_PIXEL\_BAD flags in the  $i$ -band to avoid unreliable  $i$ -band sources.

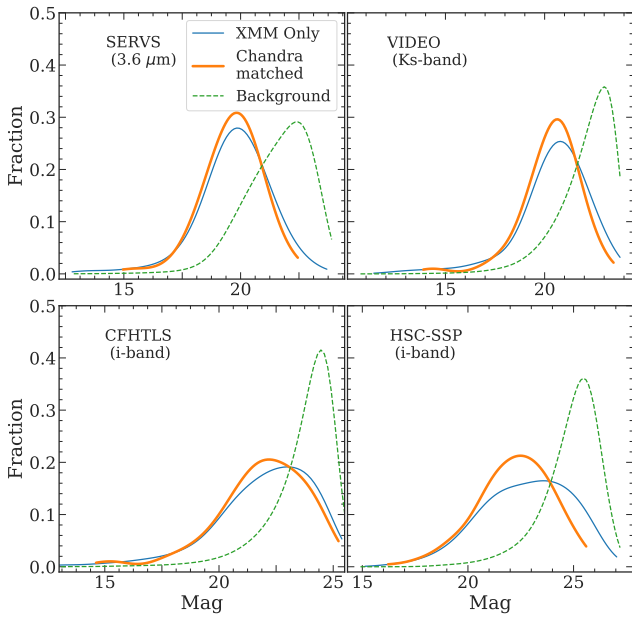


**Figure 13.** Kernel-density estimations of the magnitude distributions (solid lines) for the expected counterparts in SERVS (top-left), VIDEO (top-right), CFHTLS (bottom-left), and HSC-SSP (bottom-right). We show the distributions obtained using the full *XMM-Newton* catalog ( $q(m)_{XMM-Newton}$ ), and the distributions obtained using the *Chandra* sources in the XMM-LSS field ( $q(m)_{Chandra}$ ). The magnitude distributions of the background, unrelated sources are also displayed in each panel as the dashed curves. This figure demonstrates that  $q(m)_{Chandra}$  significantly improves upon the background-dominated  $q(m)_{XMM-Newton}$  for the deep OIR catalogs in the bottom panels (in particular, the most-probable magnitude values).

between each catalog to the HSC-wide catalog to maximize the counterpart matching accuracy. In the RA direction, the adopted corrections are  $0.^{\circ}020$ ,  $0.^{\circ}027$ , and  $0.^{\circ}026$  for SERVS, VIDEO, and CFHTLS, respectively. For DEC, the adopted corrections are  $-0.^{\circ}009$ ,  $-0.^{\circ}006$ ,  $-0.^{\circ}008$  for SERVS, VIDEO, and CFHTLS, respectively.

#### 4.1 The likelihood-ratio matching method

To match reliably the X-ray sources to the OIR catalogs with much higher source densities, we employ the likelihood-ratio method (LR hereafter) similar to previous X-ray surveys, (e.g., Brusa et al. 2007; Luo et al. 2010; Xue et al. 2011; Xue et al. 2016; Luo et al. 2017). The likelihood ratio is defined as the ratio between the probability that the source is the correct counterpart, and the probability that the source is an unrelated background object (Sutherland & Saunders 1992):

$$LR = \frac{q(m)f(r)}{n(m)}. \quad (6)$$

Here  $q(m)$  is the magnitude distribution of the expected counterparts in each OIR catalog,  $f(r)$  is the probability distribution function of the angular separation between X-ray and OIR sources, and  $n(m)$  is the magnitude distribution of the background sources in each OIR catalog.

We calculate the background source magnitude distributions using OIR sources between  $10''$  and  $50''$  from any sources in our X-ray catalog.

As discussed in §3.4, the probability distribution function of the angular separation should follow the Rayleigh distribution:

$$f(r) = \frac{r}{\sigma_x^2} \exp^{-\frac{r^2}{2\sigma_x^2}}. \quad (7)$$

Note that Eq. 7 is different from the two-dimensional Gaussian distribution function that maximizes at  $r = 0$ , and thus the  $LR$  values calculated in this work are not directly comparable to previous works that adopted a Gaussian  $f(r)$ .

In practice, for an X-ray source with a total of  $N_c$  counterpart candidates within the search radius, the matching reliability for the  $i$ -th counterpart candidate  $MR_i$ , can be determined using the following equation:

$$MR_i = \frac{LR_i}{\sum_{k=0}^{N_c} LR_k + (1 - Q)} \quad (8)$$

Here  $Q$  is the completeness factor, which is defined as  $Q = \int_{-\infty}^{m_{lim}} q(m) dm$ , where  $m_{lim}$  is the limiting magnitude of the OIR catalog being used for matching. For each counterpart candidate,  $MR$  is equivalent to the relative matching probability among all possible counterpart candidates. See Eq. 5 of Sutherland & Saunders (1992) and §2.2 of Luo et al. (2010) for details.

Due to the relatively large positional uncertainties of *XMM-Newton* and the high source densities of the OIR catalogs, deriving an accurate magnitude distribution of the expected counterparts,  $q(m)$ , using *XMM-Newton* data is challenging. Therefore, we obtain  $q(m)$  for our X-ray sources by first matching our *XMM-Newton* catalog to the *Chandra* Source Catalog 2.0 (CSC 2.0; Evans et al. 2010) to take advantage of the higher angular resolution and positional accuracy of *Chandra*. We derive the positional uncertainties of the *Chandra* sources in our survey region using the same empirical approach described in Xue et al. (2011) by selecting CSC sources in the RA/DEC range of our catalog, and matching them onto HSC-SSP using a  $1.5''$  radius. We select CSC sources that are uniquely matched to our X-ray catalogs within the 95% uncertainties (*Chandra* and *XMM-Newton* positional uncertainties are added in quadrature). A total of 223 sources in our *XMM-Newton* catalog are matched to a unique *Chandra* source in the CSC. We match these *Chandra* sources to the four OIR catalogs using Eq. 6, with  $q(m)$  derived using the iterative approach described in Luo et al. (2010), which determines the  $LR$  threshold by optimizing the matching reliability and completeness. The  $q(m)$  derived from the CSC sources,  $q(m)_{Chandra}$ , is then used as the expected magnitude distribution for OIR counterparts of our *XMM-Newton* sources. The X-ray flux distributions in the soft, hard, and full bands of the *Chandra*-matched subsample are similar to those of our entire *XMM-Newton* catalog, and therefore  $q(m)_{Chandra}$  should be consistent with the intrinsic magnitude distributions of the real OIR counterparts of our full X-ray catalog. The counterpart-matching processes are run on four different OIR catalogs: SERVS, VIDEO, CFHTLS, and HSC-SSP. The details of the filters and apertures of the photometry in each OIR catalog can be found in Appendix A, where we give the descriptions of the

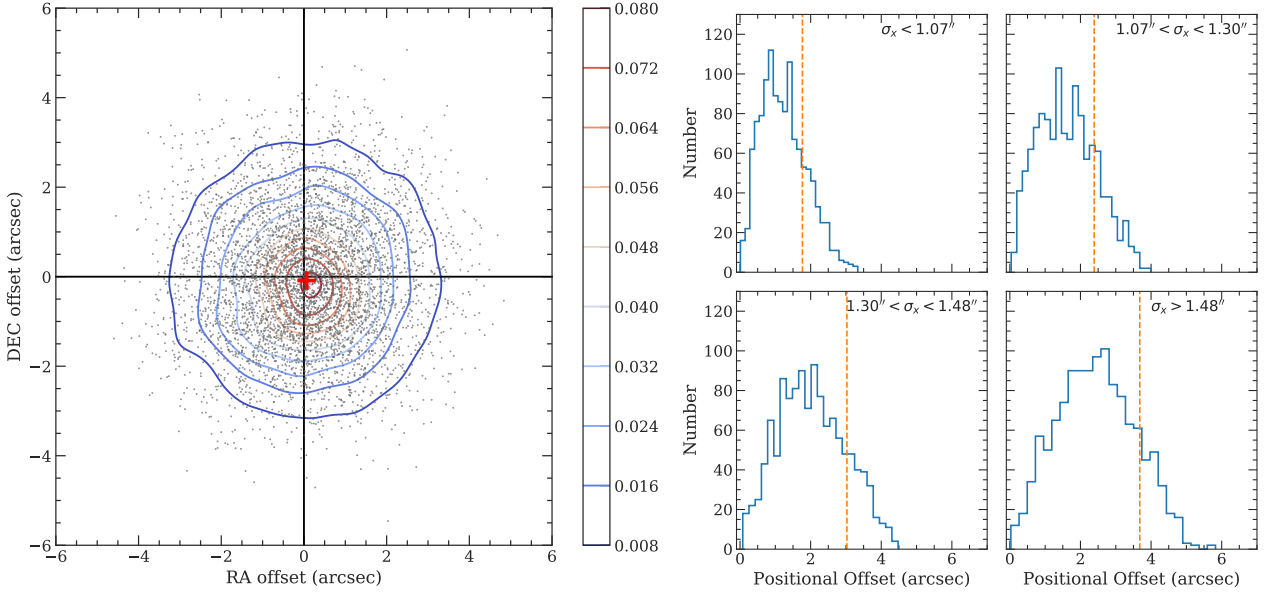


**Figure 14.** *Left:* Distribution of the OIR-to-X-ray positional offsets in the RA vs. DEC plane for the 4858 *XMM-Newton* sources with reliably matched OIR counterparts. The contours represent the isodensity levels of the points. The mean positional offsets are  $< 0.1''$  in both the RA and DEC directions (the red cross). *Right:* Histograms of positional offsets for the 4858 reliably matched sources, divided into four bins based on their positional uncertainties. In each panel, we also mark the median 68% positional offset value ( $r_{68\%}$ ) as the vertical dashed line.

columns reported in the source catalog (Columns 113–180 of Table A). For illustration, Fig. 13 shows the magnitude distributions of the background sources and the distributions of the expected counterparts derived using CSC sources.

For comparison, we also obtain  $q(m)$  for the full *XMM-Newton* catalog without using the *Chandra* positions,  $q(m)_{XMM-Newton}$ . We again use the Luo et al. (2010) iterative method, but with a  $3''$  initial search radius.  $q(m)_{XMM-Newton}$  is also plotted in Fig. 13. It is evident that for ultra-deep OIR catalogs such as HSC-SSP and CFHTLS,  $q(m)_{XMM-Newton}$  is skewed toward the faint background sources compared to the *Chandra*-matched subsample. For the other catalogs, we find no qualitative difference between  $q(m)_{Chandra}$  and  $q(m)_{XMM-Newton}$ , but we still use  $q(m)_{Chandra}$  for consistency.

We next compute the  $LR$  values for all OIR sources within a  $10''$  radius (i.e., the counterpart “candidates”) of the X-ray sources using Eq. 6. For each OIR catalog, we choose the  $LR$  thresholds ( $LR_{th}$ ) such that the reliability and completeness parameters are maximized (see Eq. 5 of Luo et al. 2010 for details). Counterparts with  $LR > LR_{th}$  are considered to be reliably matched. A summary of the results is reported in Table 4. For each OIR catalog, we list the number of all X-ray sources with at least one OIR counterpart candidate within  $r_{99\%}$  of the X-ray sources,  $N_{All}$ , and the number of X-ray sources with at least one reliably matched source with  $LR > LR_{th}$ ,  $N_{Reliable}$ . For an X-ray source with only one OIR counterpart candidate within the search radius but where its matching  $LR$  is smaller than  $LR_{th}$ , we consider the counterpart candidate to be an acceptable match if the separation from the OIR position to the X-ray position is less than  $r_{99\%}$ . The total number of such cases for each OIR catalog is listed as  $N_{Acceptable}$  in Table 4.

Motivated by the sizes of the spurious-matching rates (see §4.2 for the cross-matching reliability analysis), we first

select a “primary” counterpart for each X-ray source from, in priority order, SERVS, VIDEO, CFHTLS, and HSC-SSP. After selecting the primary OIR counterpart, we associate different OIR catalogs with each other using a simple nearest-neighbor algorithm. Thanks to the much smaller positional uncertainties of the OIR catalogs, we adopt a constant search radius of  $1''$  for the OIR catalog associations, which is the approach used by the *Spitzer* Data Fusion database (Vaccari 2015).

Using this approach, 4832 ( $\approx 93\%$ ) X-ray sources have at least one robust counterpart with  $LR > LR_{th}$ . We consider an additional 26 X-ray sources without any counterpart candidates having  $LR > LR_{th}$  to have “acceptable” matches because there is only one unique counterpart in all four OIR catalogs within  $r_{99\%}$ . When considering both the  $LR > LR_{th}$  counterparts and the acceptable counterparts, 4858 X-ray sources in our catalog are considered to have reliable OIR counterparts (94%). Of these sources, 4011 are matched to SERVS as the primary counterpart, 370 are from VIDEO, 376 are from CFHTLS, and 180 are from HSC.

Besides the 4858 X-ray sources with reliable/acceptable counterparts, **most of the remaining 316 sources have  $f_{spurious} \leq 0.05\%$  in at least one band**, and thus they are unlikely to be spurious X-ray detections. 234 of these 316 sources still have at least one OIR counterpart candidate within the  $r_{99\%}$  circle. Therefore, 5147 X-ray sources have at least one OIR counterpart candidate within  $r_{99\%}$ . Of the other 82 sources, 77 still have at least one OIR counterpart candidate within the  $10''$  counterpart-searching radius. We still select counterparts for these sources and the properties of these counterparts are included in the main X-ray catalog. However, only the previously mentioned 4858 sources are considered to be reliably matched and are flagged in the catalog. We find 5 sources that are completely “isolated”, i.e.,

**Table 4.** Summary of  $LR$  counterpart-matching results for each OIR catalog, with an additional summary row for the combined results from all OIR catalogs considered. The columns in the summary row are the same as those for individual OIR catalogs except for Column 7). Column 1: Catalog name. Column 2: Survey magnitude limit for each catalog in AB. Column 3: Survey area. Column 4: Positional uncertainty for each OIR catalog. Column 5:  $LR$  threshold. Column 6: Total number of X-ray sources with at least one counterpart within the  $10''$  search radius in each catalog. Column 7: Average number of OIR sources within  $r_{99\%}$  of the X-ray sources (if the X-ray source is within the coverage of the OIR catalog). Here the summary row shows the total number of X-ray sources with at least one OIR counterpart within  $r_{99\%}$ . Column 8: Total number of X-ray sources with at least one counterpart with  $LR > LR_{th}$ . The summary row displays the number of all X-ray sources with at least one  $LR > LR_{th}$  counterpart from any of the four OIR catalogs, plus the 23 sources with only one unique counterpart within  $r_{99\%}$  from all OIR catalogs considered (see §4.1 for details). X-ray sources having only one unique OIR counterpart in all OIR catalogs considered within  $r_{99\%}$ , but the  $LR$  values do not exceed the reliability thresholds in all OIR catalogs. Columns 9–11: See §4.2 for details. Column 9: The fraction of X-ray sources in the “associated population” based on the results of Monte Carlo simulations. Column 10: False-matching rates determined using Monte Carlo simulations. Column 11: Fraction of the X-ray sources having identical reliable counterparts found based on their *Chandra* and *XMM-Newton* positions. Based on sources in regions where there is overlapping *XMM-Newton* and *Chandra* coverage. For the summary row, Columns 9–11 are calculated as the weighed sum (based on the number of primary counterparts from each catalog) of the results from all four OIR catalogs.

Catalog	Limiting Magnitude	Area deg $^2$	$\sigma$	$LR_{th}$	$N_{\text{All}}$	$\overline{N}_{99\%}$	$N_{\text{Reliable}}$	$f_{\text{AP}}$	False Rate (Simulation)	Identical Fraction ( <i>Chandra</i> )
(1)	(2)	(3)	(4)	(5)	(6)	(7)	(8)	(9)	(10)	(11)
SERVS	$3.6\mu\text{m} < 23.1$	5.0	$0.5''$	0.32	4689	1.0	3948	96.8%	4.2%	97.3%
VIDEO	$K_s < 23.8$	4.5	$0.3''$	0.25	4380	1.3	3827	86.3%	8.0%	94.4%
CFHTLS-wide	$i < 24.8$	5.4	$0.2''$	0.22	5185	1.5	4207	75.6%	15.6%	90.8%
HSC-SSP	$i < 26.5$	5.4	$0.1''$	0.25	5124	2.3	4317	78.6%	18.4%	87.3%
Summary	N/A	N/A	N/A	N/A	5237	5147	4858	93.1%	5.8%	97.1%

no counterpart candidates were found within a  $10''$  search radius. Visual inspection of these sources shows that all coincide with a bright star, thus making the pipeline OIR photometry unavailable.

Fig. 14 presents the positional offsets between the X-ray sources and the reliably matched sources. The small median positional offsets in the RA and DEC directions demonstrate the quality of our astrometry, and the histograms of the positional offsets for sources binned in different  $\sigma_x$  show that our empirically derived positional uncertainties are reliable. For each source, we also generate postage-stamp images at X-ray, mid-IR, near-IR, and optical wavelengths. For illustration, we show a random collection of 16 X-ray sources with reliable counterparts in Fig. 15.

For the 4465 X-ray sources with primary counterparts from SERVS or VIDEO (regardless of matching reliabilities), 295 of them have no optical counterparts in CFHTLS and HSC-SSP. Visual inspection suggests that most of these sources are genuinely optically-faint. For 33 of the 295 sources, the optical counterpart is a bright star (or in the vicinity of one), and the photometry is unavailable from the CFHTLS or HSC-SSP catalogs due to saturation. There are also 1214 X-ray sources without a VIDEO counterpart, of which 784 are not in the footprint of VIDEO. For the remaining 430 X-ray sources without VIDEO photometry, visual inspection suggests that most of them are indeed NIR-faint, except for these 42 sources that either coincide with a bright star or are located on artifacts such as satellite tracks. To obtain useful OIR information for sources without reliable optical or NIR photometry, we search for counterparts in several additional OIR surveys with footprint in our X-ray catalog region, including the Sloan Digital Sky Survey (York et al. 2000) Data Release 12 (SDSS, Alam et al. 2015), the Two Micron All Sky Survey (2MASS, Skrutskie et al. 2006), and the UK Infrared Telescope Deep Sky Survey (the Deep Extragalactic Survey layer, UKIDSS-DXS; Warren et al. 2007). For our X-ray sources catalog, we only search for counterparts in these catalogs that are within  $1''$

of the OIR positions of the primary counterparts. With the supplementary catalogs, we recover the optical photometry for the 33 sources that do not have pipeline photometry from CFHTLS and HSC-SSP. We also identify an additional 298 sources with NIR photometry from 2MASS or UKIDSS-DXS. The basic properties of counterparts in these supplementary catalogs are also reported in the final source catalog (Table A).

There are also 1068 sources with multiple counterparts having  $LR > LR_{th}$  and  $LR > 0.5LR_{\text{primary}}$  in various OIR catalogs. For these sources, we select a “secondary” counterpart based on the following priority order: (i) 239 best matches from VIDEO; (ii) 48 second-best matches from SERVS; (iii) 77 second-best matches from VIDEO; (iv) 287 best matches from CFHTLS; (v) 238 best matches from HSC; (vi) 86 second-best matches from CFHTLS; and (vii) 93 second-best matches from HSC. Finally, there are 29 X-ray sources with three reliable counterparts; these tertiary counterparts are from VIDEO (4), CFHTLS (6) and HSC (19).

For the 1068 X-ray sources with secondary and/or tertiary counterparts, 869 of them are matched to a SERVS counterpart. Due to the larger PSF size of *Spitzer* IRAC ( $\approx 2''$  at  $[3.6\mu\text{m}]$ ) compared to the other OIR catalogs used in this work, it is possible that some of these secondary/tertiary counterparts from VIDEO, CFHTLS, or HSC-SSP are blended with the primary counterparts in the *Spitzer* image. Among these 1068 X-ray sources, a total of 318 of them are matched to a primary SERVS counterpart which appears to be two sources separated by  $< 2''$  in higher angular resolution bands. These counterparts are flagged in our final catalog. Excluding these 318 X-ray sources with potentially blended SERVS counterparts, the vast majority ( $\approx 85\%$ ) of X-ray sources with secondary and/or tertiary counterparts have a primary counterpart with  $MR > 0.9$ , suggesting that these additional counterparts are unlikely to be true counterparts of the X-ray sources. For completeness, these secondary and tertiary counterparts are also reported in our final catalog in Table A.

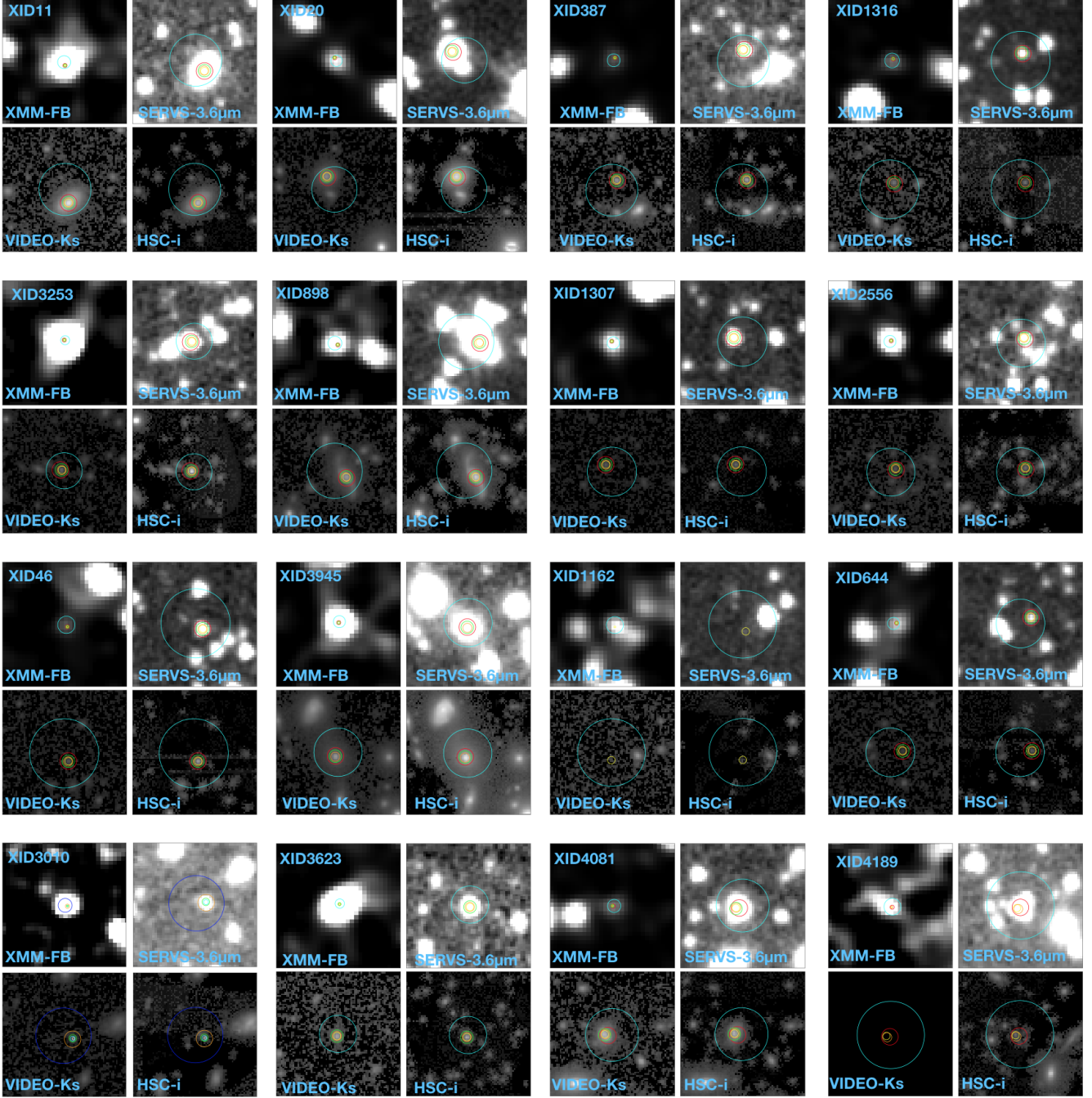


**Figure 15.** Postage-stamp images for 16 randomly selected X-ray sources in our catalog. For each source, we show (1) Full-band X-ray image smoothed with a Gaussian filter (upper-left panel). The unique source ID from Table A is shown in this panel. (2)  $3.4\mu\text{m}$  mid-IR image from SERVS (upper-right panel) (3)  $Ks$ -band near-IR image from VIDEO (lower-left panel) (4)  $i$ -band optical image from HSC-SSP (lower-right panel), re-sampled to a  $0.^{\prime}4$  pixel size. Due to the large pixel size, the X-ray image for each source is set at  $2' \times 2'$ . For the OIR images, the sizes are set at  $0.5' \times 0.5'$ . In each image, the X-ray position is marked as the cyan circle with the  $r_{99}$  radius. The position of the most-probable mid-IR SERVS counterpart is marked as the red circle with a  $1.^{\prime}5$  radius. The positions of VIDEO, CFHTLS, and HSC-SSP counterparts are marked as green, orange, and yellow circles with a  $0.^{\prime}9$ ,  $0.^{\prime}6$ , and  $0.^{\prime}3$  radius, respectively. The size of the OIR counterpart circles are 3 times the positional uncertainty values reported in Table 4. The entire set of postage-stamp images is available in the electronic version.

## 4.2 Counterpart identification reliability

We assess the reliability of the *LR* matching results using the Monte Carlo simulation approach described in Broos et al. (2007) and Xue et al. (2011). Compared to the simple estimation based on matching OIR catalogs to a random X-ray catalog, the Broos et al. (2007) method usually provides a more realistic assessment of the matching reliability. As described in Broos et al. (2007) and Broos et al. (2011), we consider our X-ray sources to consist of two different intrinsic populations, the “associated population” and the “isolated population”. The associated population is comprised of X-ray sources that do have a real counterpart in the corresponding OIR catalog, and the X-ray sources that should not have any OIR counterparts belong to the isolated population.

For the associated population, counterpart-matching procedures can produce three different outcomes: (1) an X-ray source is matched to its correct counterpart (correct match, or CM), (2) an X-ray source is matched to an incorrect counterpart (incorrect match, or IM), and (3) no counterparts were recovered (false negative, or FN). The spurious fraction of the associated population is defined as  $N_{\text{IM}}/(N_{\text{IM}}+N_{\text{CM}})$ . For the isolated population, there are two possible matching results: (1) no counterparts are found (true negative, or TN), and (2) an OIR source is identified as a counterpart (false positive, or FP). The spurious fraction of the isolated population is defined as the number of FPs divided by the size of the X-ray catalog. By definition, the spurious matches for these two populations are intrinsically different. The chance for the X-ray sources in the isolated population to have a counterpart is mostly determined by the source surface density of the OIR catalog being matched. On the other hand, since X-ray sources in the associated population must have a real OIR counterpart within a reasonable search radius, the spurious fraction is essentially determined by how well the *LR* matching method can discern a real counterpart from background sources.

In order to estimate the fractions of X-ray sources in both populations for our catalog, we simulate each population separately. The details of the simulation procedure can be found in the appendix of Broos et al. (2007) and §5 of Broos et al. (2011). A brief summary of the simulations is given below: (1) For the “associated population”, we remove all OIR sources considered to be a match in §4.1, then move the position of each OIR source by  $1'$  in a random direction. We then generate fake OIR “counterparts” for each X-ray source in our catalog based on the X-ray and OIR positional uncertainties, and the expected magnitude distributions derived in §4.1. (2) For the “isolated population”, we create mock X-ray sources that are at least  $20''$  away from any real X-ray sources.

A total of 100 simulations are carried out for each population, and we run the *LR* matching procedures on each simulation as described in §4.1. The simulations of the isolated populations usually produce a much higher spurious fraction (i.e., the number of false-positives divided by the size of the X-ray catalog). For the SERVS, VIDEO, CFHTLS, and HSC-SSP catalogs, the median spurious fractions of the isolated populations are 19%, 24%, 30%, and 40%, respectively. For the associated populations, the spurious fractions

(defined as  $N_{\text{IM}}/(N_{\text{IM}}+N_{\text{CM}})$ ) for SERVS, VIDEO, CFHTLS, and HSC-SSP are 3%, 5%, 7%, and 9%, respectively.

For the *LR* matching results with the real data, X-ray sources that were not reliably matched to any counterparts (with a total number of  $N_{\text{negative}}$ ) should contain a mixture of the FNs of the associated population and the TNs of the isolated population. Therefore, we can use the median FN and TN from simulations to estimate the fraction of X-ray sources in the associated population ( $f_{\text{AP}}$ ):

$$N_{\text{negative}} = N_{\text{FN}} \times f_{\text{AP}} + N_{\text{TN}} \times (1 - f_{\text{AP}}). \quad (9)$$

With  $f_{\text{AP}}$ , we can estimate the expected number of X-ray sources that have a spurious match as the weighted sum of the numbers of IM and FP. The false-matching rate,  $f_{\text{False}}$ , should therefore be:

$$f_{\text{False}} = (N_{\text{IM}} \times f_{\text{AP}} + N_{\text{FP}} \times (1 - f_{\text{AP}}))/(N_{\text{positive}}). \quad (10)$$

Here we consider  $N_{\text{positive}}$  as the combination of both the “reliable” and “acceptable” matches reported in Table 4.

We carry out simulations for each OIR catalog. The values of  $f_{\text{False}}$  and  $f_{\text{AP}}$  for each OIR catalog are also reported in Table 4. Due to the high  $f_{\text{AP}}$  values, the false-matching rates of our matching results are mostly determined by the spurious fractions of the associated populations, which are much lower than those of the isolated populations. Adopting the *Chandra*-matched counterpart magnitude density,  $q(m)_{\text{Chandra}}$ , does reduce the false-matching rates compared to those derived using  $q(m)_{\text{XMM-Newton}}$ . For the SERVS and VIDEO catalogs, the improvements are marginal (< 0.5%), while the improvements for CFHTLS and HSC-SSP are more significant ( $\approx 2\%$  and 6%, respectively).

We further scrutinize the *LR* matching reliabilities by making use of the 223 CSC sources and their multiwavelength matching results described in §4.1. We assess the reliability of the matching results of these *Chandra* sources using the aforementioned Monte Carlo method, and measure false-match fractions of 0.9%, 1.4%, 2.8%, and 3.3%, for SERVS, VIDEO, CFHTLS, and HSC-SSP, respectively. For each catalog, we also directly compare the reliable matches obtained with *XMM-Newton* and *Chandra* positions; 97%, 94%, 91%, and 87% of the reliable *Chandra* matching results and the reliable *XMM-Newton* results are the same for the SERVS, VIDEO, CFHTLS, and HSC catalogs, respectively. The high “identical fractions” between the matching results obtained using *Chandra* positions and *XMM-Newton* positions are slightly lower than the false-matching rates calculated based on the Monte Carlo simulation because we only compare X-ray sources with reliable counterparts at the *Chandra* and *XMM-Newton* positions in each catalog. Similar to what was done for the full *XMM-Newton* catalog, we also select “primary” counterparts for the *Chandra* sources using the same priority orders. 85%, 10%, 1%, and 4% of the *Chandra* sources have their “primary” counterparts from SERVS, VIDEO, CFHTLS, and HSC-SSP, respectively. When comparing the primary counterparts of these *Chandra* sources and the primary counterparts of the corresponding *XMM-Newton* sources,  $\approx 97\%$  are identical, demonstrating that the matching results of the *XMM-Newton* catalog are highly reliable.

### 4.3 Supplementary multiwavelength matching results with the NWAY Bayesian catalog matching method

We supplement the *LR* matching results with the Bayesian catalog matching tool NWAY (Salvato et al. 2017).<sup>24</sup> The fundamental difference between the Bayesian approach and the likelihood-ratio approach is that the former makes use of the distance and magnitude priors from multiple catalogs simultaneously to select the most-probable counterpart in all catalogs considered. NWAY also allows cases in which counterparts can be absent, and the matching results were computed considering all possible combinations. The details of the NWAY matching methodology are described in Appendix B of Salvato et al. (2017).

NWAY computes three quantities for deciding the most-probable match, *p-single*, *p-any* and *p-i*, where each possible counterpart has a different *p-single* value based on its distance from the *XMM-Newton* position. This value could be weighted by the priors supplied (e.g.,  $q(m)$  and  $n(m)$  in Eq. 6 are similar to a magnitude prior). In our case, *p-single* is the posterior probability for a counterpart to be correctly associated with the X-ray source based on the angular separation from the X-ray position weighted by the magnitude-distribution prior, and the surface densities of the X-ray and OIR catalogs. For each X-ray source, *p-single* of all possible counterparts is considered to compute a single *p-any* value, which represents the posterior probability of the X-ray source having any correct counterparts (i.e.,  $p\_any = 0$  if there are no OIR counterparts within the search radius of the X-ray source). The last quantity, *p-i*, is the relative probability of a possible counterpart being the correct match. For an X-ray source with multiple possible counterparts, the counterpart with the highest *p-i* ( $p_{i\text{Best}}$ ) is considered to be the most-probable match and is assigned the MATCH\_FLAG = 1 flag by NWAY. Counterparts with *p-i* higher than 50% of  $p_{i\text{Best}}$  are also flagged by NWAY as MATCH\_FLAG = 2.

Similar to our *LR* approach, we make use of the *Chandra* sources in the XMM-LSS field to compute the priors of the expected counterparts. We use the “auto” functionality of NWAY with a 1.5'' search radius for defining the “real” counterparts. In addition to the magnitude priors, we include an additional prior based on the *Spitzer* IRAC color from SERVS, [3.6μm]/[4.5μm]. Since the majority of our X-ray sources are expected to be AGNs, the distinct [3.6μm]/[4.5μm] mid-IR color of luminous AGNs (see Fig. 23) provides additional discerning power. For a small number of sources, this additional prior is useful for discerning two adjacent SERVS sources with comparable magnitudes (see the top-right panel of Fig. 16 for illustration).

After computing the magnitude and IRAC color priors using the *Chandra* sources, we run NWAY on the full X-ray catalog with a search radius of 10''. Based on the results from *LR* matching (§4.1), we do not assume a completeness prior because only 0.01% of the X-ray sources are completely isolated. All four OIR catalogs are considered simultaneously. We report the multiwavelength matches with MATCH\_FLAG=1,2 in Table B supplementary to the *LR* matching results.

Since NWAY matches all four OIR catalogs simultaneously, we cannot determine the spurious-matching rates for the “associated” and “isolated” populations as we did for estimating the spurious-matching rates for *LR* results using Monte Carlo simulations (see §4.2). Salvato et al. (2017) suggest that the NWAY matching reliability can be determined by a *p-any* threshold, which is chosen based on re-running NWAY on randomly shifted “fake” X-ray catalogs. However, this approach is equivalent to estimating the spurious matching rates for the “isolated” population using the Broos et al. (2007) method, which is usually much higher than the results obtained with the two-population approach (see Broos et al. 2007, Xue et al. 2011, and §4.2 for details). Therefore, we do not adopt any *p-any* thresholds for the NWAY matching results. The NWAY matching results can still be assessed by investigating the CSC-matched subsample of 223 X-ray sources; the difference between the matching results obtained using *Chandra* and *XMM-Newton* positions with NWAY are similar to the *LR* results described in §4.2.

We also use the 223 *Chandra*-detected subsample as a baseline for comparing matching results obtained using the NWAY or *LR* methods. We focus only on comparing the SERVS counterparts, as the vast majority of *LR* matching results are decided based on the primary counterparts from SERVS. We confirm that all *Chandra* sources have the same SERVS matching results using *LR* and NWAY. Therefore, we can use the *Chandra* results obtained with *LR* to assess the matching reliability of both *LR* and NWAY matching results with *XMM-Newton* positions. Examples of such comparisons are shown in Fig. 16. 95% of the sources have the same matching results from LR, NWAY, and *Chandra*. A small fraction (two sources) of *LR* matching results do not agree with those of *Chandra* but could be recovered by NWAY. On the other hand, two of the NWAY matching results do not agree with the *Chandra* results but could be identified by LR. Five of the *Chandra* sources have different SERVS counterparts than both the *LR* and NWAY results. *Chandra* and OIR images of these sources suggest that they are either two X-ray sources blended due to the *XMM-Newton* PSF, or there are multiple OIR counterparts with very similar magnitudes and distances to the X-ray position, and thus it is not surprising neither *LR* nor NWAY could successfully recover the correct counterparts. As demonstrated in Fig. 16, these five sources have multiple counterparts with comparable magnitudes and similar spatial separations from the *XMM-Newton* position. This result suggests *LR* and NWAY perform similarly for finding SERVS counterparts. For the ≈ 5% of X-ray sources with different LR and NWAY counterparts, their X-ray fluxes are typically lower (with a median full-band flux of  $7.5 \times 10^{-15}$  erg cm<sup>-2</sup> s<sup>-1</sup>, which is ≈ 44% of the median flux of the full X-ray catalog). This is expected as fainter X-ray sources have larger positional uncertainties, which lead to higher numbers of counterpart candidates.

When further scrutinizing the 95% of sources with identical SERVS counterparts from LR, NWAY, and *Chandra*, we find that NWAY occasionally (for ∼ 10% of the X-ray sources) consider the best-fit combination to be the one with counterparts in some of the other OIR catalogs being “absent”. For instance, one of the X-ray sources has a reliable SERVS counterpart identified

<sup>24</sup> <https://github.com/JohannesBuchner/nway>.

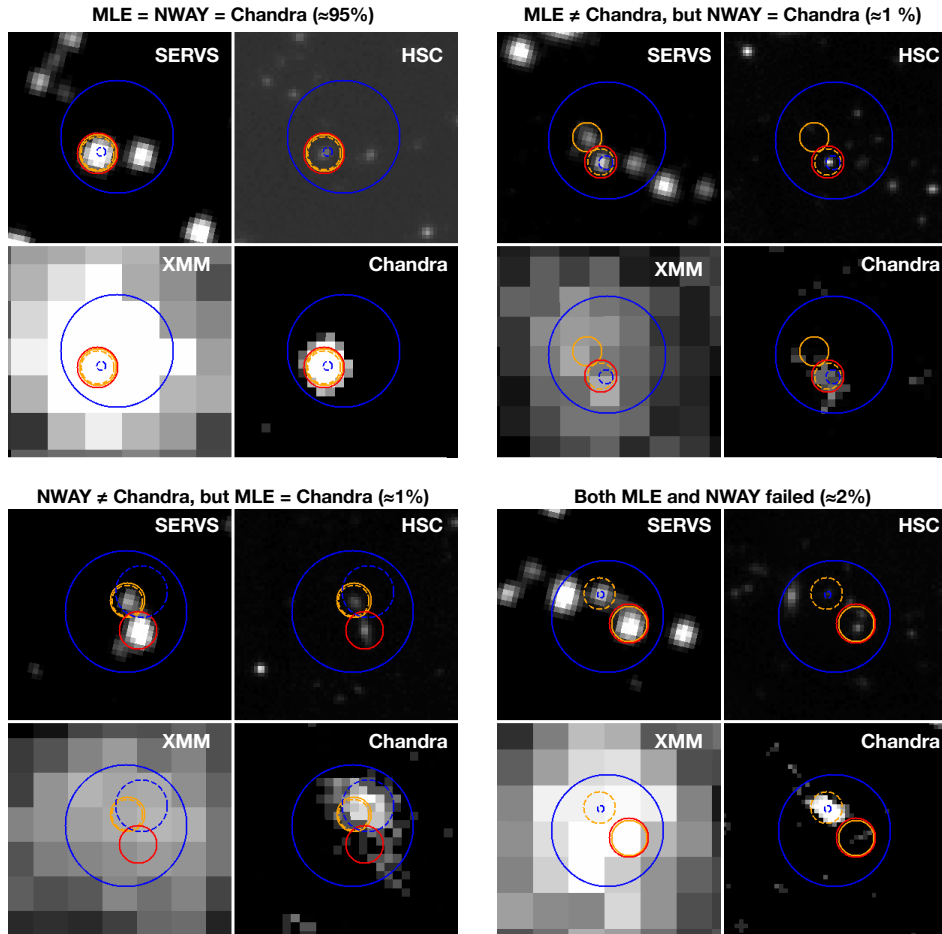


**Figure 16.** Illustrations of the comparison between the matching results using *XMM-Newton* positions or *Chandra* positions for four X-ray sources in our sample. The panel for each source shows images from SERVS [3.6 $\mu$ m](top-left), HSC *i*-band (top-right), *XMM-Newton* 0.5–10 keV (bottom-left), and *Chandra* 0.5–7 keV (bottom-right). X-ray positions are marked as blue circles with a 99.73% error radius, with the *XMM-Newton* positions indicated using solid lines and the *Chandra* positions identified using dashed lines. SERVS counterparts identified with the *LR* method are marked as orange circles with a 2'' radius, solid lines are the counterparts of the *XMM-Newton* positions, and dashed lines are the counterparts of the *Chandra* positions. SERVS counterparts of the *XMM-Newton* positions identified using *NWAY* are shown as the red circles. For the vast majority of *XMM-Newton* sources with *Chandra* counterparts from CSC, our counterpart-matching results are identical to the results obtained using *Chandra* coordinates and positional uncertainties.

by both *NWAY* and *LR*. For the SERVS counterpart, there is only one VIDEO source within the 0.5'' positional error circle of SERVS. For the *LR* approach described in §4.1, the VIDEO source is assigned to the correct SERVS counterpart. However, *NWAY* does not consider this VIDEO source to be among the most-probable combination of counterparts from all four OIR catalogs that were being matched simultaneously. This result is likely due to how *NWAY* computes  $p_i$ . When multiple OIR catalogs are taken into account simultaneously,  $p_i$  represents the relative probability of counterparts from *all* OIR catalogs being the correct match. In this example, the VIDEO counterpart has an unlikely magnitude according to the VIDEO magnitude prior; therefore, including the VIDEO source as a correct match would result in a lower  $p_i$  compared to the case where the VIDEO source is excluded from the matched counterparts. Similar mismatches are found when comparing the *NWAY* and *LR* matching results for the full *XMM-Newton* catalog. *NWAY*

does not have this behavior when no magnitude or color priors are used; however, without the inclusion of magnitude and color priors, *NWAY* can only rely on the distance-based priors, thereby losing critical discerning powers for matching *XMM-Newton* sources to the dense OIR catalogs. Further corroborating the Bayesian method's effectiveness of counterpart-matching with multiple OIR catalogs is beyond the scope of this work. Therefore, we list the *NWAY* matching results “as-is” in Table B, and we consider only the *LR* matching results listed in Table A when exploring the multi-wavelength properties of the X-ray sources reported in this work. The matching results obtained using *NWAY* are shown in Table B, and the descriptions of this table's columns are listed in Appendix B. Only the counterparts with  $\text{MATCH\_FLAG} \geq 1$  are included.

**Table 5.** Redshift catalogs used in this work. Column 1: Redshift survey name. Column 2: Survey instrument. Column 3: Survey sensitivity. Column 4: Targeting fields. Column 5: Survey area. Column 6: Total number of redshifts matched the main X-ray catalog. Column 7: Total number of redshifts assigned to the X-ray sources in the main catalog. Column 8: Reference

Catalog (1)	Instrument (2)	Survey sensitivity (3)	Targeting fields (4)	Area (5)	$N_{\text{matched}}$ (6)	$N_{\text{assigned}}$ (7)	Reference (8)
SDSS	BOSS	$r \lesssim 22.5$	XMM-XXL-North	$25 \text{ deg}^2$	1075	1075	Dawson et al. (2013); Menzel et al. (2016)
PRIMUS	IMACS (Low-Dispersion Prism)	$i \lesssim 23.5$	XMM-LSS	$2.9 \text{ deg}^2$	749	347	Coil et al. (2010)
VIPERS	VIMOS	$i \lesssim 22.5$	XMM-LSS	$7.8 \text{ deg}^2$	332	164	Garilli et al. (2014)
UDS Compilation	Multiple instruments	N/A	UDS	$0.8 \text{ deg}^2$	302	73	N/A (see Footnote 22)
CSI	IMACS (Uniform-Dispersion Prism)	$[3.6 \mu\text{m}]_{\text{AB}} \lesssim 21$	XMM-LSS	$6.9 \text{ deg}^2$	516	68	Kelson et al. (2014); Patel et al. (2015)
VVDS	VIMOS	$17.5 \lesssim i \lesssim 24.5$	XMDS+SXDS	$3 \text{ deg}^2$	81	38	Le Fevre et al. (2013)
UDSz	VIMOS/FORS2	$K < 23$	UDS	$0.5 \text{ deg}^2$	22	15	Bradshaw et al. (2013); McLure et al. (2013)
3D-HST	WFCS G141 Grism	$JH_{\text{IR}} \lesssim 24$	UDS	$191.2 \text{ arcmin}^2$	15	6	Skelton et al. (2014); Momcheva et al. (2016)

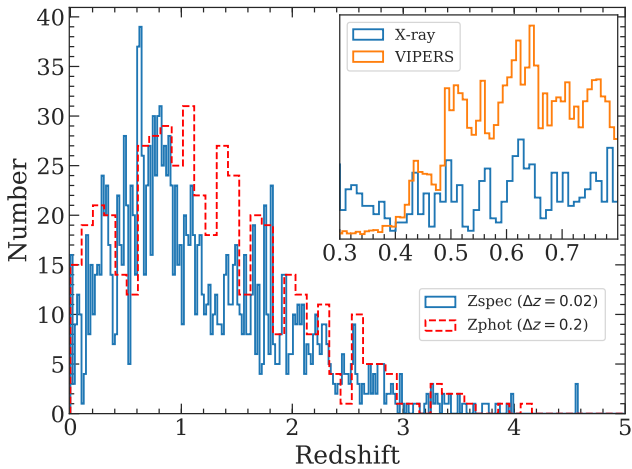


**Figure 17.** Distribution of the redshifts in bins of  $\Delta z = 0.02$  for the 1787 X-ray sources with spectroscopic-redshift measurements from the literature. The photometric redshift distribution for the 477 sources with high-quality photometric redshifts are also plotted as the red dashed histogram in bins of  $\Delta z = 0.2$ . The redshift spikes are likely associated with large-scale structure filaments (e.g., Luo et al. 2017; Xue 2017). A comparison between the normalized redshift distribution of the X-ray sources and that of the  $i$ -band selected galaxies from the VIPERS survey is also shown in the insert with  $\Delta z = 0.01$  bins, which suggests that some of the redshift spikes (e.g.,  $z \approx 0.6$ ) of X-ray sources overlap with those of the general galaxy population.

#### 4.4 Spectroscopic redshifts

The XMM-LSS region is covered by a number of spectroscopic redshift surveys that target galaxies with various optical magnitude constraints: the PRISM Multi-Object Survey (PRIMUS; Coil et al. 2010), the VIMOS Public Extragalactic Redshift Survey (VIPERS; Garilli et al. 2014), and the VIMOS VLT Deep Survey (VVDS; Le Fevre et al. 2013). As part of the SDSS-BOSS program, 3042 X-ray sources found in the XMM-XXL-North field ( $25 \text{ deg}^2$ ) with  $r < 22.5$  were all observed by the SDSS Baryon Oscillation Spectroscopic Survey (Dawson et al. 2013; Menzel et al. 2016). Also, there are three other redshift surveys in the XMM-LSS region that target near-IR selected galaxies, including the spec-

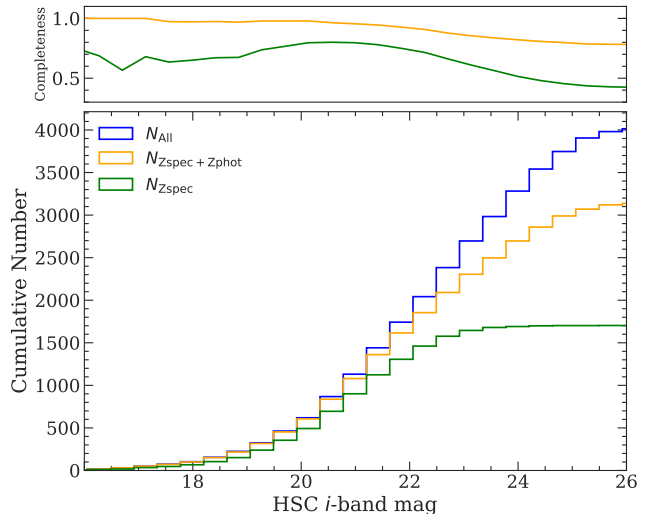


**Figure 18.** Cumulative distribution of the HSC  $i$ -band magnitudes for all of the 4548 X-ray sources in the  $4.5 \text{ deg}^2$  subfield covered by the N18 forced-photometry catalog (see § 4.5) is shown as the blue histogram. The cumulative distribution of the spectroscopic redshifts is indicated by the green histogram, and the cumulative distribution of sources with high-quality photometric or spectroscopic redshifts is indicated by the orange histogram. Top panel shows the fraction of sources with spectroscopic redshifts (i.e., the green histogram divided by the blue histogram) as a function of the  $i$ -band magnitudes. Fraction of sources with good photometric or spectroscopic redshifts as a function of  $i$ -band magnitudes is shown as the orange curve.

troscopic observations of the UKIDSS Ultra-Deep Survey (UDSz; Bradshaw et al. 2013; McLure et al. 2013), the 3D-HST Survey (Skelton et al. 2014; Momcheva et al. 2016) in the UDS region, and the Carnegie-Spitzer-IMACS Redshift Survey (CSI; Kelson et al. 2014). We list the properties of each redshift catalog in Table 5.

We adopt the same nearest-neighbor matching criterion with a  $1''$  matching radius to associate these redshifts to each OIR catalog. The redshift for each X-ray source is determined by the coordinates of its primary OIR counterpart.

In cases where redshifts from different catalogs do not agree with each other, we choose redshifts using the following ordering (ranked by the spectral resolution at  $r$ -band and reliability): SDSS, VVDS, VIPERS, UDSz, PRIMUS (reliable), CSI (reliable), 3D-HST, PRIMUS (acceptable), and CSI (acceptable). In addition to these redshift surveys, We include the compilation of  $\approx 4000$  publicly available but unpublished redshifts in the UDS field.<sup>25</sup> An additional 72 X-ray sources have spectroscopic redshifts culled from this catalog. We also search for publicly available spectroscopic redshifts for all of our counterparts not included in the aforementioned redshift catalogs on NASA Extragalactic Database (NED), but no additional secure redshifts were found.

Of the 5242 sources in our main X-ray source catalog, 1787 have spectroscopic redshifts ranging from  $0 < z < 4.57$ . Fig. 17 presents the redshift histogram in bins of  $\Delta z = 0.02$ . There are several redshift “spikes” indicative of large-scale structures containing X-ray AGNs (e.g., Fig. 9 of Luo et al. 2017 and Fig. 20 of Xue 2017). Notably, the X-ray source redshift spike at  $0.6 < z < 0.7$  appears to coincide with one of the major large-scale structures seen in the VIPERS redshift survey (see Fig. 14 of Garilli et al. 2014 and the insert panel of Fig. 17). The cumulative histogram of the  $i$ -band magnitudes of the sources with spectroscopic redshifts is shown in Fig. 18 as the green histogram.

#### 4.5 Photometric redshifts

High-quality photometric redshifts for AGNs are not yet available for our full survey region, but they are available in a number of smaller subfields. In particular, in a  $\approx 1 \text{ deg}^2$  area within the XMM-LSS region, Nyland et al. (2017) have presented a “forced-photometry” catalog using the Tractor image modeling code (Lang et al. 2016). The forced-photometry technique employs source position and surface brightness profile priors from the high-resolution fiducial band of the VIDEO survey to model and fit the fluxes of lower-resolution bands. Nyland et al. (2017) demonstrated that their multi-band forced photometry of mixed resolution optical and IR surveys using the Tractor led to a statistically significant improvement in photometric redshift accuracy compared to position-matched multi-band catalogs (see §5.2 of Nyland et al. 2017 for details). For this work, we make use of a similar forced-photometry catalog for the full **4.5 deg<sup>2</sup>** area with VIDEO or SERVS coverage (Nyland et al. 2018, in preparation; N18 hereafter). The N18 catalog is similar to the Nyland et al. (2017) catalog, except the image cutout width for each source has increased by a factor of two (from  $10''$  to  $20''$ ) and the sky noise and sky level are now calculated in each image cutout using iterative sigma clipping. We make use of the 12-band photometry from  $u'$  to IRAC  $4.5\mu\text{m}$  to derive photometric redshifts for the X-ray sources in this region using the methods described in Yang et al. (2014). The photometric bands include CFHTLS  $u$ -band; HSC-SSP  $g$ ,  $r$ ,  $i$ ,  $z$ , and  $y$  bands (Deep layer); VIDEO

<sup>25</sup> These redshifts were obtained with Subaru FOCAS, AAT 2dF, VLT VIMOS, and AAOmega, and the full redshift catalog is available at [http://www.nottingham.ac.uk/~ppzoa/UDS\\_redshifts\\_18oct2010.fits](http://www.nottingham.ac.uk/~ppzoa/UDS_redshifts_18oct2010.fits), see <http://www.nottingham.ac.uk/astronomy/UDS/data/data.html> for an overview of this compilation.

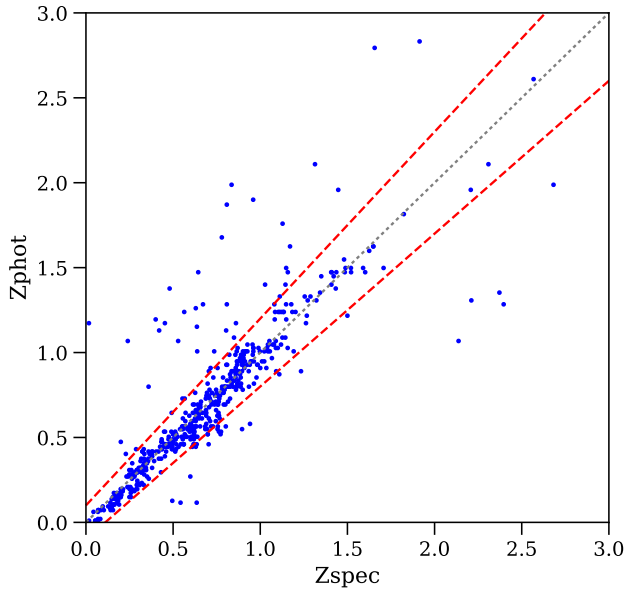


**Figure 19.** Spectroscopic and photometric redshifts for the 536 non-broad-line AGN sources with high-quality photometric redshifts and spectroscopic redshifts. The red dashed lines mark the  $|\Delta z|/(1 + z_{\text{spec}}) = 0.15$  thresholds for outliers, and the black dotted line marks the  $z_{\text{spec}} = z_{\text{phot}}$  relation.

$J$ ,  $H$ , and  $K_s$  bands (DR5); and *Spitzer*  $3.6 \mu\text{m}$  and  $4.5 \mu\text{m}$  bands from the SERVS DeepDrill survey (*Spitzer* Program ID 11086; Lacy et al., in preparation).

We match the N18 catalog to the coordinates of the primary counterparts of the X-ray sources that are considered to be reliable matches using a  $1''$  matching radius. We exclude X-ray sources that are classified as broad-line AGNs according to their optical spectra due to their much higher photometric redshift uncertainties. **A total of 3731 X-ray sources satisfy these criteria. Of these sources,  $\approx 27\%$  of them are detected (i.e., with Tractor measured signal-to-noise-ratio  $> 5$ ) in all 12 bands. The 25th, 50th, and 75th percentile of the number of bands with detection for the 3731 X-ray sources are 9, 11, and 12.** Since the flux uncertainties in N18 do not account for uncertainties in PSF homogenization processes, we adopt an additional 3% systematic for the flux errors, which is typical of PSF modeling uncertainties (e.g., §5.3 of Yang et al. 2014).

Following the recipe of Yang et al. (2014), we measure the photometric redshifts using the SED-fitting code EAZY (Brammer et al. 2008) using the default galaxy templates and settings, and an additional obscured AGN template from Polletta et al. (2007). As described in §5.6 of Yang et al. (2014), we perform iterative procedures to adjust the photometric zero points; the zero-point corrections are  $\lesssim 0.1$  mag. For each source, EAZY calculates a parameter  $Q_z$  (see Eq. 8 of Brammer et al. 2008) to indicate photometric-redshift quality. We consider photometric redshifts with  $Q_z < 1$  as reliable (see §6.3 of Yang et al. 2014). There are 538 sources with  $Q_z < 1$  and reliable spectroscopic redshifts, which can be used to assess the quality of photometric-redshift measurements. The normalized median

absolute deviation (NMAD) is  $\sigma_{\text{NMAD}} = 0.04$ , with an outlier fraction (defined as  $|\Delta z|/(1+z_{\text{spec}}) > 0.15$ ) of  $f_{\text{outlier}} = 9.3\%$ , which is comparable to the photometric-redshift reliability reported in Yang et al. (2014) for the CDF-N. For this work, we do not include the broad-line AGN (BLAGN) templates as Yang et al. (2014) did. This is primarily driven by the significantly worse photometric redshift qualities when including the BLAGN templates. In addition, Yang et al. (2017) estimated that the fraction of broad-line AGNs missed by spectroscopic campaigns in the COSMOS field is likely less than  $\approx 18\%$ . Considering the comparable surface density of the spectroscopically confirmed BLAGNs in this work and that in the COSMOS field, only a small fraction of sources would require an additional BLAGN template. In fact, the vast majority of our sources (excluding spectroscopically confirmed BLAGNs) can be well-characterized with galaxy templates alone, and the high fraction (see below) of our sources with high-quality photometric redshifts also justifies our choice of fitting templates.

Fig. 19 compares the photometric and spectroscopic redshifts for the 536 sources with reliable photometric redshifts. The  $4.5 \text{ deg}^2$  area covered by N18 contains 1543 reliable photometric redshifts for sources that do not have spectroscopic redshift measurements, increasing the fraction of sources with redshifts from  $\approx 32\%$  to  $\approx 70\%$ . We expect to expand the photometric redshift measurements to all of our X-ray sources to the full XMM-SERVS:XMM-LSS field when the photometry catalog with data from both the SERVS DeepDrill survey (*Spitzer* Program ID 11086; Lacy et al., in preparation) and the VEILS survey (see Table 1) becomes available in the near future. We have also ran our photoz codes on all sources in the preliminary N18 catalog, and we report the full photometric redshifts for the 426,348 sources (excluding the broad-line AGNs) in Appendix C. The full details of the Tractor catalog over the  $4.5 \text{ deg}^2$  field will be presented in Nyland et al. (2018).

#### 4.6 Source properties and classification

In this section we briefly discuss some of the properties of the 4858 sources with reliable counterparts. For the 1787 X-ray sources with secure spectroscopic redshifts, we calculate their rest-frame 2–10 keV “apparent” luminosity assuming a  $\Gamma = 1.7$  power-law spectrum corrected for Galactic absorption. Fig. 20 compares the flux, redshift, and luminosity distributions of our sample to those from archival X-ray surveys, including XMM-COSMOS, COSMOS-Legacy, and Stripe 82X. Fig. 21 displays the  $L_X - z$  distribution of our sample, along with the  $L_X$  vs. HR, HR vs. full-band flux, and full-band flux vs. redshift distributions. The comparisons in the middle and right panels of Fig. 20 are limited to sources with available spectroscopic redshifts in the Stripe-82 and XMM-LSS regions. The left panel of Fig. 20 demonstrates that our catalog occupies a valuable region of parameter space among X-ray surveys by more than doubling the source counts of the XMM-COSMOS survey, which will enable a wide range of science that was previously limited by either survey sensitivity or cosmic variance.

Here we also include the basic AGN identification results in our catalog. Detailed source clas-

sifications using multiwavelength SED and X-ray spectroscopic fitting results will be presented in a separate article. For sources with spectroscopic observations, we directly make use of the spectroscopic classifications when available. Since each spectroscopic survey has its own unique design and methodology, we only make use of the “broad-line” classifications provided in the SDSS, VIPERS, VVDS, and PRIMUS catalogs to identify broad-line AGNs. The information on spectroscopic classifications are not yet publicly available for the other spectroscopic surveys. For each X-ray source with optical spectroscopic coverage, we have included the spectroscopic flags from all available redshift catalogs (see Column 181 of the main X-ray catalog described in Appendix A.) A total of 927 sources are classified as AGNs based on the broad-line spectroscopic flags specified in the SDSS, VIPERS, VVDS, or PRIMUS catalogs. Since 90% of the spectroscopic redshifts for our X-ray sources are culled from one of these four catalogs, we expect the vast majority of the remaining X-ray sources with spectroscopic coverages to have galaxy-like spectra. For sources without spectroscopic observations, only a small fraction ( $\sim 18\%$ ) of them is expected to be broad-line AGNs (see §4.5 and Yang et al. 2017 for details). For the other sources, we use the criteria described in Luo et al. (2017) to select AGNs: (1) An X-ray luminosity threshold where we regard sources with rest-frame  $L_{2-10 \text{ keV}} > 3 \times 10^{42} \text{ erg s}^{-1}$  as an AGN. A total of 1635 sources satisfy this criterion. (2) X-ray bright sources with X-ray-to-optical or X-ray-to-near-IR flux ratios larger than  $\log f_x/f_r > -1$  or  $\log f_x/f_{Ks} > -1.2$ , respectively. To calculate the flux ratios, we use the HSC-SSP  $r$ -band photometry of the primary counterpart. For sources without a detection in the HSC-SSP  $r$ -band, we make use of CFHTLS or SDSS  $r$ -band when available. For the 265 sources that are not detected in HSC-SSP, CFHTLS, or SDSS, we calculate their flux-ratio lower limits using the HSC-SSP wide survey upper limit,  $r = 26.4$ . For the X-ray-to-near-IR flux ratios, we use the VIDEO  $Ks$ -band photometry. For sources within the VIDEO coverage but not detected in the  $Ks$ -band, we calculate the lower limits for  $\log f_x/f_{Ks}$  assuming a  $Ks = 23.8$  upper limit. For sources outside the VIDEO coverage, we make use of the UKIDSS DXS survey  $Ks$ -band photometry when possible and assign an upper limit of  $Ks = 21$  for the non-detected sources. For sources outside the coverage of VIDEO and UKIDSS, the shallow photometric depth of 2MASS ( $Ks < 14.3$ ) cannot be used to select AGNs, since no sources this bright would have a high  $\log f_x/f_{Ks}$  ratio satisfying the AGN selection criterion. There are 5011 sources with  $\log f_x/f_r > -1$  and 4723 sources with  $\log f_x/f_{Ks} > -1.2$ , totaling 5078 sources that can be classified as an AGN based on their  $f_x/f_r$  or  $f_x/f_{Ks}$  values. The flux-ratio distributions are displayed in Fig. 22.

In addition to the classification methods described above, AGNs can also be identified based on the distinctive red mid-IR color arising from hot dust heated by SMBH accretion (e.g., Lacy et al. 2004; Stern et al. 2005, 2012; Donley et al. 2012; Assef et al. 2013; Mateos et al. 2013). We select these mid-IR AGNs based on three different selection criteria from Lacy et al. (2004), Stern et al. (2005), and Donley et al. (2012). The Lacy et al. (2004), Stern et al. (2005) crite-

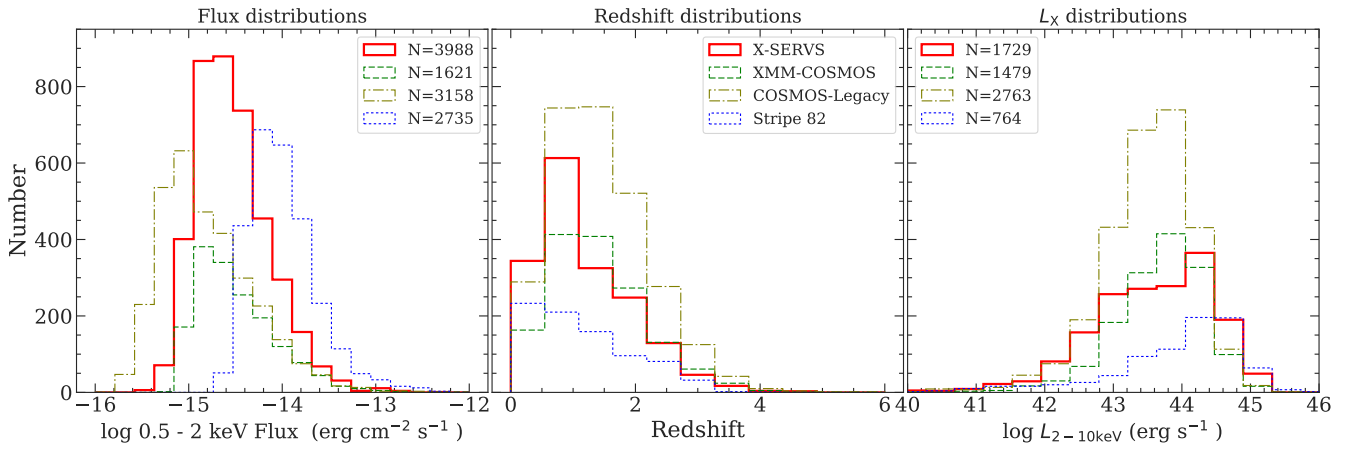


**Figure 20.** A comparison between this work (solid red line), XMM-COSMOS (green dashed line), COSMOS-Legacy (brown dash-dotted line), and Stripe 82-X (blue dotted line). Distributions shown in panels from left to right are: 0.5–2 keV flux, redshift, and  $\log L_{2-10\text{keV}}$ , respectively. The left panel shows the distribution of soft-band fluxes for the soft-band detected sources in each catalog; no redshift information is required. The numbers of the soft-band sources are listed in the left panel. For the middle and right panels, the histograms are for the subset of sources with redshift measurements (regardless of the detection bands), with source numbers marked in the right panel.

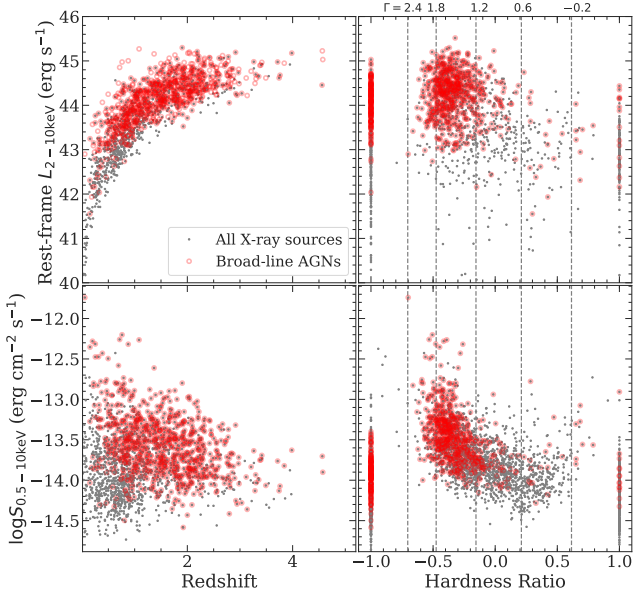


**Figure 21.** Properties of the 1787 X-ray sources with spectroscopic-redshift measurements, including (1) the  $L_{2-10\text{keV}}$  vs.  $z$  distribution (top-left), (2)  $L_{2-10\text{keV}}$  vs. hardness ratio (top-right), (3) 0.5–10 keV flux vs. redshift (bottom-left), (4) 0.5–10 keV flux vs. hardness ratio (bottom-right). Broad-line AGNs are marked as the red open circles. In the right panels, the expected hardness ratios for power-law spectra (with Galactic column density) with different photon indices are plotted as the vertical dashed lines. Sources detected only in the soft or hard bands have their HR set at  $-1$  and  $1$ , respectively.

ria have higher completeness while the Donley et al. (2012) criterion is more reliable (i.e., has much less star-forming galaxy interlopers). Only 1716 X-ray sources have a primary counterpart that are detected in all four IRAC bands, which

is a requirement of using these IRAC two-color selection criteria. Of these 1716 sources, 1300, 1158, and 834 satisfy the Lacy et al. (2004), Stern et al. (2005), and Donley et al. (2012) criteria, respectively, for a total of 1325 individual X-ray sources. Notably, 6 sources are only identified as an AGN based on their IRAC colors. On the other hand, of all X-ray sources with detections in all four IRAC bands, 257 AGNs identified using the AGN selection criteria described in the previous paragraph do not satisfy any of the three IRAC color-color selection criteria. The IRAC color distributions of the 1716 X-ray sources, and the 12990 SWIRE sources in our X-ray catalog region are displayed in Fig 23.

The total number of sources classified as AGNs is 5084, or 96.8% of the total sample. For the sources not classified as AGNs, 53 of them have spectroscopic-redshift measurements, including 13 stars with  $z \approx 0$ , and 40 galaxies hosting low X-ray luminosity sources. They may be powered by star-formation processes in galaxies given their relatively weak X-ray to OIR ratios and low X-ray luminosities. The remaining 115 sources are relatively bright in the optical and NIR bands (median  $r$ -band and  $K_s$ -band magnitudes are 15.5 and 14.1, respectively), and thus all of them have optical-to-X-ray and near-to-X-ray flux ratios lower than the AGN selection thresholds, suggesting they are either foreground stars or low-redshift galaxies hosting X-ray sources powered by stellar processes.

## 5 SUMMARY

In this work, we present a new X-ray point-source catalog in the XMM-LSS region constructed using both considerable new AO-15 and archival *XMM-Newton* data. The main results are the following:

1. Our X-ray catalog is constructed based on data in a  $5.3 \text{ deg}^2$  rectangular region centered at RA= $35.580^\circ$ , DEC= $-4.965^\circ$ . A total of 155 pointings from 149 different *XMM-Newton*

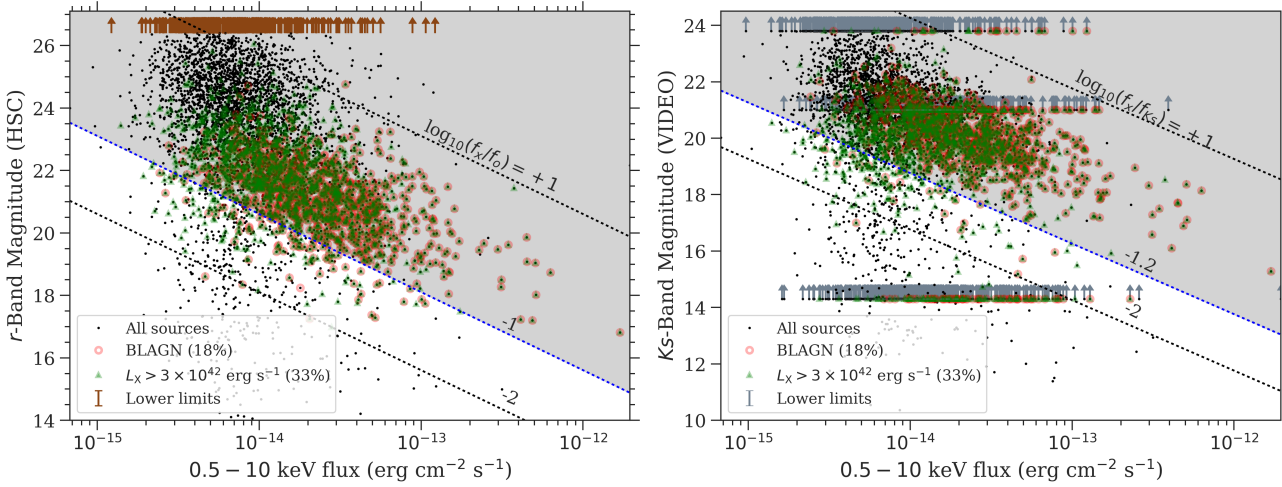


**Figure 22.** *Left* – Distributions of the optical flux in the  $r$ -band vs. full-band (0.5–10 keV) X-ray flux. Lower limits for sources not detected in the HSC-SSP wide survey  $r$ -band are displayed as the brown upward arrows. *Right* – The near-IR flux in the  $K_s$ -band versus full-band X-ray flux. Lower limits for sources not detected in VIDEO are also shown as the upward arrows. Since only  $\approx 85\%$  of the X-ray catalog region is covered with VIDEO, some of the X-ray sources have lower limits from 2MASS ( $K_s = 14.3$ ), UKIDSS DXS survey ( $K_s = 21$ ), and VIDEO ( $K_s = 23.8$ ). In both plots, the shaded regions mark the “AGN” regime as defined by the  $\log_{10} f_x/f_0 > -1$  (left) or the  $\log_{10} f_x/f_{Ks} > -1.2$  (right) thresholds as described in §4.5 of Luo et al. (2017). For sources with spectroscopic redshift measurements, we also mark those with  $L_x > 3 \times 10^{42} \text{ erg s}^{-1}$  as the green triangles. The 833 sources with optical spectra consistent with broad-line AGNs are also marked as open red circles.

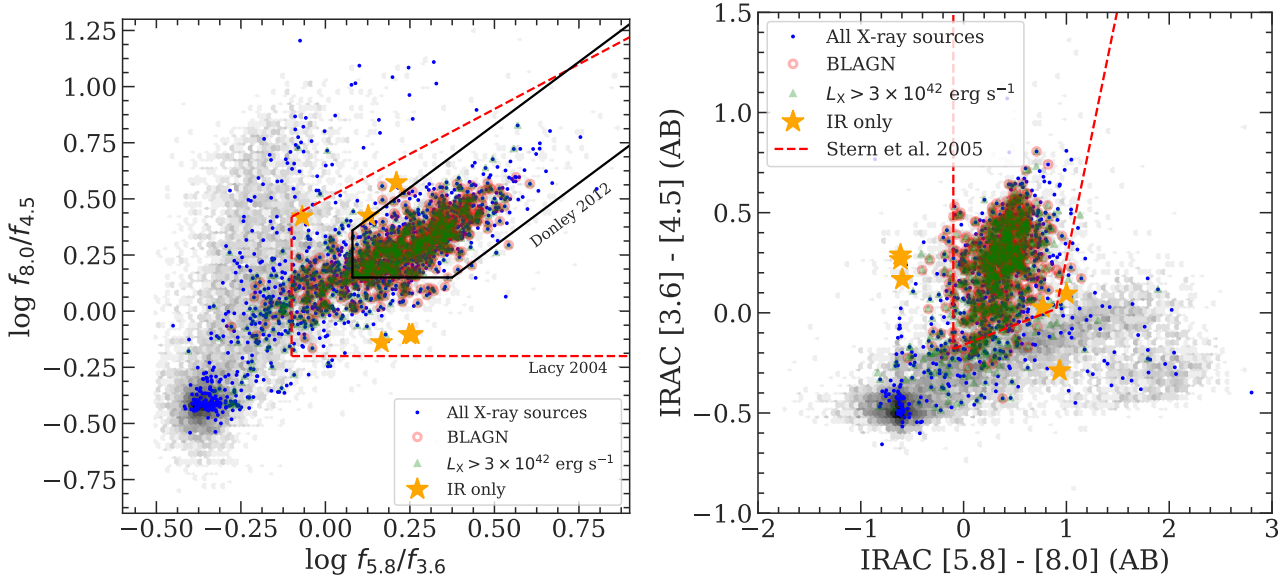


**Figure 23.** *Left* –  $\log f_{5.8}/f_{3.6}$  vs.  $\log f_{8.0}/f_{4.5}$  distribution. *Right* – IRAC[5.8] – [8.0] vs. [3.6] – [4.5] (AB) distributions. In both panels, the *Spitzer* IRAC two-color distribution for the 1716 X-ray sources with detections in all four IRAC bands are shown as the blue dots. X-ray luminous AGNs and spectroscopically confirmed quasars are also shown as the green triangles and the open red circles, respectively. There are a total of 1325 sources with IRAC colors satisfying one of the three mid-IR color AGN selection criteria (Lacy et al. 2004, Stern et al. 2005, and Donley et al. 2012). The 6 sources that are only identified as an AGN based on their IRAC colors are displayed as the large orange stars. The color distribution for the 12990 SWIRE sources in our X-ray catalog region is also shown as the gray hexagonal cells, where darker color indicates higher source density.

ObsIDs are used, with a total of 2.7 Ms background-filtered exposure time (1.1 Ms from AO-15). The median value of the cleaned PN exposure time is 46 ks for the full 5.3 deg<sup>2</sup> field (see §2). Our survey has a flux limit of  $1.7 \times 10^{-15}$ ,  $1.3 \times 10^{-14}$ , and  $6.5 \times 10^{-15}$  erg cm<sup>-2</sup> s<sup>-1</sup> over 90% of its

5.3 deg<sup>2</sup> area in the soft, hard, and full bands, respectively, reaching the desired uniformity and survey depth (see §3.6).

2. We use Monte Carlo simulations to estimate the fraction of spurious sources ( $f_{\text{spurious}}$ ) as a function of DET\_ML values at each band, and we consider sources with  $f_{\text{spurious}} \leq 1\%$  to be reliably detected. This corre-

- sponds to DET<sub>ML</sub> thresholds of 4.8, 7.8, and 6.2 in the soft, hard, and full bands, respectively (§3.3).
3. The main X-ray source catalog is generated using EWAVELET and EMLDETECT. All 5242 sources with EMLDETECT DET<sub>ML</sub> values satisfying the  $f_{\text{spurious}} \leq 1\%$  criterion in the soft band (0.5–2 keV), hard band (2–10 keV), or full band (0.5–10 keV) are included. Of the 5242 sources, 2861 are the same X-ray sources identified in previous X-ray surveys in our survey area (e.g., the XMM-XXL-North survey; Liu et al. 2016), and 2381 are newly discovered X-ray sources (see §3.5). There are 2967 sources with more than 100 X-ray counts in the full band (PN + MOS), and 126 sources with more than 1000 X-ray counts (see §3.5).
  4. The absolute astrometry of the *XMM-Newton* catalog is registered to the WCS frame of the Subaru HSC-SSP survey (§3.1). The positional uncertainties for the X-ray sources are determined based on an empirical relation between the X-ray-to-optical positional offsets and the X-ray source counts. Our empirical positional uncertainties are well-characterized by the Rayleigh distribution. The median positional uncertainties in the soft, hard, and full bands are 1''.35, 1''.37, and 1''.31, respectively (see §3.4).
  5. We search for OIR counterparts in the SERVS, VIDEO, CFHTLS, and HSC-SSP surveys; 98% (5147/5242) of the X-ray sources have at least one OIR counterpart candidates within the 99.73% positional uncertainties ( $r_{99\%}$ ). A total of  $\approx 93\%$  (4858/5242) of the X-ray sources have at least one reliable OIR counterpart (§4.1). There are 1787 secure spectroscopic redshifts from SDSS, VIPERS, VVDS, UDSz, PRIMUS, CSI, and 3D-HST (§4.4). For a 4.5 deg<sup>2</sup> sub-field in our survey region covered by SERVS, we make use of the forced-photometry catalog from N18 to compute photometric redshifts (§4.5), achieving >70% spectroscopic+photometric redshift completeness for 85% of our survey area. We expect to expand the photometric redshift measurements to all of our X-ray sources when SERVS DeepDrill survey (Spitzer Program ID 11086; Lacy et al., in preparation) and the VEILS survey (see Table 1) are completed.
  6. We test the matching results using a subsample of 223 X-ray sources with a reliable *Chandra* counterpart from CSC 2.0. Approximately 97% of the matching results from *XMM-Newton* and *Chandra* are identical, demonstrating our multiwavelength matching results are highly reliable (see §4.2).
  7. We classify 5054 X-ray sources as AGNs based on their optical spectra from SDSS, VIPERS, or VVDS (927); X-ray luminosity larger than  $3 \times 10^{42}$  erg s<sup>-1</sup> (1635); large X-ray-to-optical and/or X-ray-to-NIR flux ratios (5078); and *Spitzer* IRAC colors (1325). See §4.6 for details.

The X-ray source catalog presented in this work is the first > 2 deg<sup>2</sup> X-ray survey with sensitivity comparable to that of COSMOS. The 5.3 deg<sup>2</sup> wide-area and 46 ks depth survey will enable a wide range of studies. For instance, the large AGN sample and the excellent multiwavelength coverage will provide a means of exploring the behavior of AGNs in the multidimensional space of galaxy parameters. The wide area of this survey will also enable studies of AGN triggering mechanisms as a function of environment. In the near future, the combination of AGN samples from this work, COSMOS, and the other XMM-SERVS fields will sample the full range of cosmic large-scale structures, alleviating the

cosmic-variance uncertainties present in previous COSMOS results (e.g., Meneux et al. 2009; de la Torre et al. 2010; Skibba et al. 2014) as well as advancing our understanding of the coevolution of SMBHs and their host galaxies.

## ACKNOWLEDGMENTS

We thank the referee for the suggestions that improved the manuscript. We thank Matthias Ehle, Norbert Scharbel, and the *XMM-Newton* Science Operations Centre for help with scheduling the *XMM-Newton* AO-15 observations. We thank Stephanie LaMassa and Johannes Buchner for helpful discussions, Francesca Civano and Stefano Marchesi for providing comparison data. We acknowledge the support of NASA grant NNX17AF07G (CTJC, WNB, GY, and FV), National Key R&D Program of China grant 2016YFA0400702 (BL), and National Natural Science Foundation of China grant 11673010 (BL). DMA acknowledges support from Science and Technology Facilities Council (STFC) grant code ST/L00075X/1. FEB acknowledges support from CONICYT-Chile (Basal-CATA PFB-06/2007, FONDECYT Regular 1141218), the Ministry of Economy, Development, and Tourism's Millennium Science Initiative through grant IC120009, awarded to The Millennium Institute of Astrophysics, MAS. MJJ was supported by the Oxford Centre for Astrophysical Surveys, which is funded through generous support from the Hintze Family Charitable Foundation. MJJ and BH acknowledge support from STFC (ST/N000919/1). IRS acknowledges support from STFC (ST/P000541/1), the ERC Advanced Investigator programme DUSTYGAL 321334 and a Royal Society/Wolfson Merit Award. YQX was supported by NSFC-11473026, NSFC-11421303, and the CAS Frontier Science Key Research Program (QYZDJ-SSW-SLH006). This work made use of data products from CFHTLS, HSC-SSP, SDSS, and VIDEO. The CFHTLS survey was based on observations obtained with MegaPrime/MegaCam, a joint project of CFHT and CEA/IRFU, at the Canada-France-Hawaii Telescope (CFHT) which is operated by the National Research Council (NRC) of Canada, the Institut National des Sciences de l'Univers of the Centre National de la Recherche Scientifique (CNRS) of France, and the University of Hawaii. This work is based in part on data products produced at Terapix available at the Canadian Astronomy Data Centre as part of the Canada-France-Hawaii Telescope Legacy Survey, a collaborative project of NRC and CNRS. The Hyper Suprime-Cam (HSC) collaboration includes the astronomical communities of Japan and Taiwan, and Princeton University. The HSC instrumentation and software were developed by the National Astronomical Observatory of Japan (NAOJ), the Kavli Institute for the Physics and Mathematics of the Universe (Kavli IPMU), the University of Tokyo, the High Energy Accelerator Research Organization (KEK), the Academia Sinica Institute for Astronomy and Astrophysics in Taiwan (ASIAA), and Princeton University. Funding was contributed by the FIRST program from Japanese Cabinet Office, the Ministry of Education, Culture, Sports, Science and Technology (MEXT), the Japan Society for the Promotion of Science (JSPS), Japan Science and Technology Agency (JST), the Toray Science Foundation, NAOJ, Kavli IPMU, KEK, ASIAA, and Princeton University. Funding for

SDSS-III has been provided by the Alfred P. Sloan Foundation, the Participating Institutions, the National Science Foundation, and the U.S. Department of Energy Office of Science. The SDSS-III web site is <http://www.sdss3.org/>. The observations for the VIDEO survey were made with ESO telescopes at the La Silla Paranal Observatories under ESO programme ID 179.A-2006.

## APPENDIX A: MAIN CATALOG DESCRIPTION

Here we describe the columns of the main X-ray source catalog, Table A. Throughout the table, we mark null values as  $-99$ . All celestial coordinates are given in equinox J2000.

### X-ray properties

Columns 1–103 give the X-ray properties of our sources. Columns for the soft-band results are marked with the “SB\_” prefix. Columns for the hard-band and full-band results are marked with the “HB\_” and “FB\_” prefixes, respectively. Note that we have calculated the upper limits on counts, count rates, and fluxes for the non-detections (Eq. 4). For these upper limits, their corresponding uncertainty columns are set as  $-99$ .

- (1) Column 1: The unique source ID (XID) assigned to each X-ray source.
- (2) Columns 2–3: RA and DEC in degrees of the X-ray source. The positions are determined based on EMLDETECT. Based on availability, we use the positions from, in priority order, the full band, soft band, and hard band as the primary position of the X-ray source. Band-specific positions are listed in Columns 8–13.
- (3) Column 4: X-ray positional uncertainty ( $\sigma_x$ ) in arcsec based on the empirical relation between source counts and positional offsets to the HSC-SSP catalog. Note that this is not the  $\sigma$  of a 2D-Gaussian distribution but rather the scaling parameter of the univariate Rayleigh distribution (see §3.4 and Pineau et al. 2017 for details). The positional uncertainties are based on those of the full band. For sources without a full-band detection, the soft-band or hard-band positional uncertainties are listed. See §3.4 for details.
- (4) Columns 5–6: 68% and 99.73% X-ray positional uncertainties in arcsec based on the Rayleigh distribution; see §3.4 for details.
- (5) Column 7: Positional uncertainties calculated by EMLDETECT,  $\sigma_{\text{eml}}$ , in arcsec. Similar to  $\sigma_x$ , we list the full-band values when possible and list soft-band or hard-band  $\sigma_{\text{eml}}$  for sources not detected in the full band.
- (6) Columns 8–13: RA and DEC in degrees of the source in the soft, hard, and full bands, respectively.
- (7) Columns 14–16: The source-detection threshold in each band, DET<sub>ML</sub>, which is computed using EMLDETECT.
- (8) **Columns 17–19:** The source-detection reliability parameter in each band, defined as  $1 - f_{\text{spurious}}$ , where  $f_{\text{spurious}}$  is the expected spurious fraction based on simulations described in §3.3. Due to the limited numerical precision, all sources with spurious fractions smaller than 0.01% have a reliability of 1. For this work, we consider sources with  $f_{\text{spurious}} \leq 1\%$  to be robustly detected.
- (9) Columns 20–22: Total (PN + MOS1 + MOS2) exposure time in seconds in each band.
- (10) Columns 23–31: PN, MOS1, and MOS2 exposure time in seconds in each band.
- (11) Columns 32–34: Total background-map values (PN + MOS1 + MOS2) in counts per pixel in each band.
- (12) Columns 35–43: PN, MOS1, and MOS2 background-map values in counts per pixel in each band.
- (13) Columns 44–46: Total (PN + MOS1 + MOS2) net counts in each band.
- (14) Columns 47–55: PN, MOS1, and MOS2 net counts in each band.
- (15) Columns 56–67: Uncertainties of total, PN, MOS1, and MOS2 net counts in each band.
- (16) Columns 68–79: Total, PN, MOS1, and MOS2 net count rates in each band, in count s<sup>-1</sup>.
- (17) Columns 80–91: Uncertainties of total, PN, MOS1, and MOS2 net count rates in each band, in count s<sup>-1</sup>.
- (18) Columns 92–97: Flux and flux uncertainty in each band, in erg cm<sup>-2</sup> s<sup>-1</sup>. The conversion factors between count rates and fluxes are derived assuming a power-law spectrum with a  $\Gamma = 1.7$  photon index and the Galactic absorption column density for each EPIC detector. Note that no correction is made for possible intrinsic absorption. See §3.5 for details. The fluxes and uncertainties reported here are the error-weighted average of all EPIC detectors.
- (19) Columns 98–100: Hardness ratio, defined as  $(H - S)/(H + S)$ , where  $H$  is the total (PN + MOS1 + MOS2) net counts divided by the total exposure time in the hard band and  $S$  is the total net counts divided by the total exposure time in the soft band. The uncertainties on the HRs are calculated based on the count uncertainties using the error-propagation method described in §1.7.3 of Lyons (1991). Sources detected only in the full band are set to  $-99$  in all three columns. The HR values for sources detected only in the soft-band are set to  $-1$ , and the HR values for sources detected only in the hard-band are set to 1. We note that one of the CCDs on MOS1 was affected by a micrometeorite impact, therefore  $H$  and  $S$  are sometimes calculated based on only results from the two cameras with non-zero exposure time.
- (20) Column 101: Rest-frame, “apparent” 2–10 keV X-ray luminosity (only corrected for Galactic absorption) computed as in §4.6.
- (21) Column 102: CSC 2.0 source name of the nearest *Chandra* source in the CSC within  $10''$ .
- (22) Column 103: XMM-XXL-North catalog source name of the nearest *XMM-Newton* source in Liu et al. (2016) within  $10''$ .

### Multiwavelength-matching results

Columns 104–113 list the multiwavelength-matching results based on the *LR* method described in §4.1. In these columns, the 99.73% positional-uncertainty radius represents the quadratic sum of the positional uncertainties of each X-ray source and the corresponding OIR catalog (see Table 4).

- (1) Columns 104–107: Number of counterpart candidates from each OIR catalog within the  $10''$  search radius of each X-ray source.
- (2) Columns 108–111: Number of sources from each OIR catalog that satisfy  $LR \geq LR_{\text{th}}$ .
- (3) Column 112: Flag set to 1 if a reliable counterpart has been identified for the X-ray source. See §4.1 for details.
- (4) Column 113: Flag set to 1 if the primary counterpart of

the X-ray source is from the SERVS catalog and might suffer from source blending. There are a total of 318 flagged sources. See §4.1 for details.

### ***Multiwavelength properties***

Columns 114–189 provide the multiwavelength properties from each OIR catalog for the primary counterparts matched to X-ray sources using the *LR* method. Properties from SERVS, SWIRE, VIDEO, CFHTLS, and HSC-SSP are marked with prefixes “SERVS\_”, “SWIRE\_”, “VIDEO\_”, “CFHT\_”, and “HSC\_”, respectively.

- (1) Column 114: Catalog from which the primary counterpart is selected. The primary counterpart is chosen in priority order from SERVS, VIDEO, CFHTLS, and HSC-SSP, which is based on the matching reliability of each OIR catalog. See §4.2 for details.
- (2) Column 115–117: RA and DEC in degrees of the primary counterpart and its separation in arcsec from the X-ray source.
- (3) Column 118: The matching likelihood ratio (*LR*) of the primary counterpart.
- (4) Columns 119–134: RA, DEC, Object ID, and the matching reliability (*MR*) of the primary counterpart culled from the original OIR catalogs.
- (5) Columns 135–138: SERVS 1.9'' aperture photometry and the associated uncertainties in the 3.6 $\mu\text{m}$  and 4.5 $\mu\text{m}$  bands.
- (6) Columns 139–146: SWIRE 1.9'' aperture photometry and the associated uncertainties in the 3.6 $\mu\text{m}$ , 4.5 $\mu\text{m}$ , 5.8 $\mu\text{m}$ , and 8.0 $\mu\text{m}$  bands.
- (7) Columns 147–148: SWIRE 5.25'' aperture photometry and the associated uncertainty in the 24 $\mu\text{m}$  band.
- (8) Columns 149–158: VIDEO PSF photometry and uncertainties in AB magnitude in the *Z*, *Y*, *J*, *H*, and *Ks* bands.
- (9) Columns 159–168: CFHTLS PSF photometry and uncertainties in AB magnitude in the *u*, *g*, *r*, *i*, and *z* bands.
- (10) Columns 169–178: HSC CModel photometry and uncertainties in AB magnitude in the *g*, *r*, *i*, *z*, and *y* bands.
- (11) Columns 179–181: RA, DEC, and Object ID from the original redshift catalogs for the primary counterparts.
- (12) Column 182: Spectroscopic redshift adopted for the X-ray source. The redshifts are chosen based on the spectral resolution of the observations and the redshift reliabilities. See §4.4 for details.
- (13) Column 183: The catalog that provided the redshift.
- (14) Column 184: Original redshift flag from one of the redshift catalogs. For SDSS, see <http://www.sdss.org/dr14/algorithms/bitmasks/#ZWARNING> for the definition of flags. For VVDS, see §3.4 of Le Fevre et al. (2013) for the definition of flags. For VIPERS, see §4.3 of Garilli et al. (2014) for the definition of flags. For PRIMUS, see <http://primus.ucsd.edu/version1.html#ztags> for the definition of flags. For CSI, see §4.6 of Kelson et al. (2014) for the definition of flags. For UDSz, see McLure et al. (2013) for the definition of flags. For the 3D-HST catalog, we only select redshifts with  $\sigma_z/(1+z) \leq 0.003$  and thus no redshift flags are included.
- (15) Column 185–188: Photometric redshift, the associated upper and lower uncertainties, and the photometric-redshift quality parameter ( $Q_z$ ). See §4.5. The photometric-redshift measurements are limited to the 4.5 deg<sup>2</sup> area with forced photometry from N18. See §4.4 for details.
- (16) Column 189: A five-digit AGN classification flag, each digit

represents the flag for an AGN classification criterion described in §4.6. From left to right: spectroscopic classification, X-ray luminosity classification, X-ray to optical flux ratio classification, X-ray to near-IR flux ratio classification, and IRAC color classification. For each digit, the number “1” means the source is not classified as an AGN using the corresponding criterion. The number “2” means the source is classified as an AGN. If the given criterion cannot be used to classify the X-ray source (e.g., there is no spectroscopic coverage), the numeric expression is “3”. For instance, if an X-ray source does not have optical spectral coverage, has  $L_X > 3 \times 10^{42}$  erg s<sup>-1</sup> and high X-ray-to-optical as well as X-ray-to-NIR flux ratios, but is not an mid-IR AGN, the source is flagged as “32221”.

### ***Multiwavelength properties for additional counterparts***

In our source catalog, there are 1068 X-ray sources with two  $LR \geq LR_{\text{th}}$  counterparts where the second-highest *LR* counterpart also satisfies  $LR \geq 0.5 LR_{\text{primary}}$  (see §4.1 for details). The highest *LR* counterparts are considered as “primary” with properties reported in Columns 114–184. Here we report the multiwavelength properties of the “secondary” counterparts in Columns 187–257, which are identical as Columns 111–181 except for the additional “SECONDARY\_” prefixes. There are also 29 X-ray sources with three  $LR \geq LR_{\text{th}}$  counterparts, where the secondary and the tertiary counterparts both satisfy the  $LR \geq 0.5 LR_{\text{primary}}$  criterion. The multiwavelength properties of the secondary counterparts for these 29 sources are also reported in Columns 190–260. The properties for the tertiary counterparts are reported in Columns 261–331, which are identical as Columns 111–181 except for the additional “TERTIARY\_” prefixes.

### ***Supplementary multiwavelength properties for primary counterparts***

In our catalog, a small number of primary counterparts do not have reliable photometry from VIDEO, CFHTLS, and HSC-SSP due to the lack of areal coverage or various instrumental artifacts (see §4.1). Columns 332–360 report supplementary properties for sources in SDSS DR12, 2MASS, and UKIDSS-DXS that are matched within 1'' of the primary counterparts. These columns are marked with “SUPPLEMENTARY\_” prefixes.

- (1) Columns 329–341: Source ID, RA, DEC (J2000, in degrees), and photometry and the associated uncertainties in the SDSS *u*, *g*, *r*, *i*, and *z* bands (CModel magnitudes).
- (2) Columns 342–350: Source ID, RA, DEC (J2000, in degrees), and photometry and the associated uncertainties in the 2MASS *J*, *H*, and *Ks* bands (in AB magnitudes).
- (3) Columns 351–357: Source ID, RA, DEC (J2000, in degrees), and photometry and the associated uncertainties in the UKIDSS-DXS *J* and *Ks* bands (in AB magnitudes).

## **APPENDIX B: SUPPLEMENTARY CATALOG WITH NWAY**

Here we describe the columns of the supplementary multiwavelength matching results obtained with NWAY (see

§4.3). Only the counterparts with  $\text{MATCH\_FLAG} \geq 1$  are included. Similar to the *LR* matching results, some of the X-ray sources have multiple probable counterparts. In this table, the same X-ray source can have multiple counterparts and the information for each counterpart is given in an independent row. Similarly to columns 114–184 of Table A, properties from SERVS, VIDEO, CFHTLS, and HSC-SSP are marked with the prefixes “SERVS\_”, “VIDEO\_”, “CFHT\_”, and “HSC\_”, respectively. Null values are marked as –99 throughout the table.

- (1) Column 1: The unique source ID (XID) assigned to the X-ray source.
- (2) Column 2: The posterior probability of the X-ray source having any correct counterparts,  $p_{\text{any}}$ , for each X-ray source.
- (3) Column 3: The relative probability of a counterpart to be the correct match,  $p_{\text{i}}$ .
- (4) Columns 4–11: RA and DEC of the counterpart in each OIR catalog in degrees.
- (5) Columns 12–15: The original Object ID of the counterpart from each OIR catalog.
- (6) Columns 16–19: Separation of the X-ray position from the counterpart in each OIR catalog in arcseconds.
- (7) Columns 20–23: SERVS 1.9'' aperture photometry and the associated uncertainties in the  $3.6\mu\text{m}$  and  $4.5\mu\text{m}$  bands.
- (8) Columns 24–31: VIDEO PSF photometry and uncertainties in AB magnitude in the  $Y$ ,  $J$ ,  $H$ , and  $K_s$  bands.
- (9) Columns 32–41: CFHTLS PSF photometry and uncertainties in AB magnitude in the  $u$ ,  $g$ ,  $r$ ,  $i$ , and  $z$  bands.
- (10) Columns 42–51: HSC CModel photometry and uncertainties in AB magnitude in the  $g$ ,  $r$ ,  $i$ ,  $z$ , and  $y$  bands.
- (11) Columns 52: Matching flag,  $\text{MATCH\_FLAG}$ . For the most-probable counterparts the flag is set to 1. For other counterparts that are almost as likely as the most-probable counterpart (i.e., with  $p_{\text{i}} \geq p_{\text{iBest}}$ ), the flag is set to 2.

## APPENDIX C: PHOTOMETRIC REDSHIFTS FOR GALAXIES IN THE 4.5 DEG<sup>2</sup> SERVS REGION

Since one of the major scientific goals of the XMM-SERVS survey is to study the interactions between AGN activity and large-scale structures, it is important to simultaneously consider the X-ray AGNs and the galaxies in the same survey region. This requires photometric redshift measurements for the full galaxy population. To this end, we have also computed photometric redshifts for the 426,348 sources from the N18 catalog that have reliable ( $\text{SNR} > 5$ ) detections in at least 5 bands. For these sources, the 25th, 50th, and 75th percentile of the number of bands with reliable detections are 9, 10, and 11, respectively. The methodologies and the multiwavelength data used are identical to those described in §4.5, except we do not include the Seyfert 2 template in our fitting for these sources. These photometric redshifts were calculated using all 12-band OIR photometry when available. To assess the quality of these photometric redshifts, we make use of the 45232 spectroscopic redshifts culled from the same redshift catalogs reported in §4.4. The normalized median absolute deviation (NMAD) is  $\sigma_{\text{NMAD}} = 0.043$ , with an outlier fraction (defined as  $|\Delta z|/(1+z_{\text{spec}}) > 0.15$ ) of  $f_{\text{outlier}} = 6.6\%$ . Fig. C1 compares the photometric and spec-

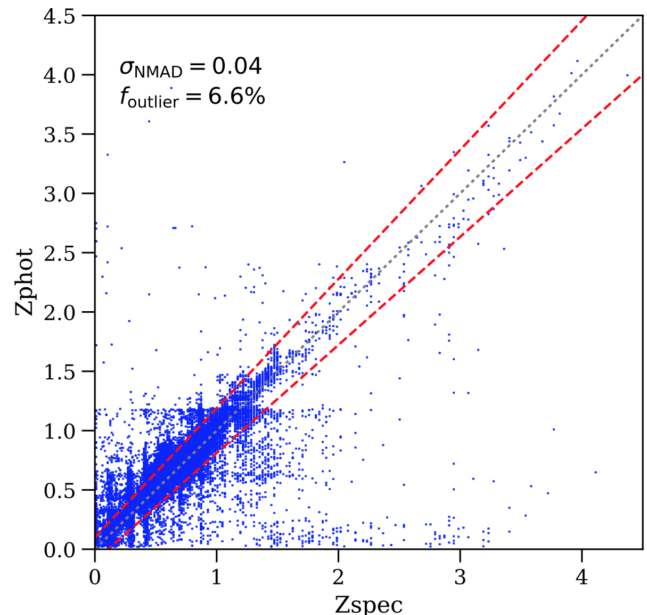


**Figure C1.** Spectroscopic and photometric redshifts for the 45232 sources with high-quality photometric redshifts and spectroscopic redshifts in the N18 catalog. The red dashed lines mark the  $|\Delta z|/(1+z_{\text{spec}}) = 0.15$  thresholds for outliers, and the black dotted line marks the  $z_{\text{spec}} = z_{\text{phot}}$  relation.

troscopic redshifts for the 45232 sources with reliable photometric and spectroscopic redshifts.

For comparison, photometric redshifts for HSC-detected sources in our survey region were also reported in (Tanaka et al. 2018). As part of HSC-SSP PDR1, these photometric redshifts were derived using the  $g$ ,  $r$ ,  $i$ ,  $z$  and  $y$  band photometry and a number of different photometric redshift algorithms (Tanaka et al. 2018), yielding  $\sigma_{\text{NMAD}} \approx 0.05$  and an outlier fraction of  $f_{\text{outlier}} \approx 15\%$  for  $i < 25$  galaxies with  $0.2 \lesssim z_{\text{phot}} \lesssim 1.5$ . For the full HSC photometric redshift sample, the mean NMAD is  $\sigma_{\text{NMAD}} = 0.08$ , and the outlier fraction is 22.7%. Thanks to the infrared photometric data from VIDEO and SERVS, our photometric redshifts are not restricted by limits set by requiring the 4000Å break to stay within the wavelength range of the HSC bands, therefore reducing the NMAD and outlier fractions compared to the HSC-SSP redshifts. In Table C, we report our photometric redshifts as well as basic source identifications. The high quality and range of these redshifts will enable a wide array of science.

**Table A.** The main X-ray source catalog with a selection of columns. Empty or null values are marked as  $-99$ . The numbers listed in the second row of this table is the column numbers of the full X-ray catalog. See Appendix A for a detailed description of each column. This table is available in its entirety in machine-readable form online.

XID (1)	RA (2)	DEC (3)	XPOSERR (4)	FB_DET_ML (16)	FB_EXP (19)	FB_BKG (31)	FB_SCTS (43)	FB_FLUX (93)	HR (95)	LX (98)	LR_RELIABLE (109)	LR_CATALOG (111)	LR_ZBEST (179)	LR_ZSOURCE (180)	CLASS (186)
XMM00000	34.200220	-4.035250	1.44	19.0	59076.2	1.74	83.04	$8.92 \times 10^{-15}$	-99.0	-99	1	HSC	-99.0	-99	33213
XMM00001	34.200710	-4.933730	1.45	63.0	61051.8	1.00	82.03	$8.53 \times 10^{-15}$	-1.0	$9.66 \times 10^{43}$	1	SERVS	1.82	UDSz	32212
XMM00002	34.201450	-5.556720	1.96	16.4	29731.6	0.80	29.64	$5.71 \times 10^{-15}$	1.0	$2.64 \times 10^{42}$	1	SERVS	0.459	VIPERS	32213
XMM00003	34.201470	-4.499310	1.50	23.3	72553.8	1.76	72.37	$5.71 \times 10^{-15}$	-1.0	$1.47 \times 10^{43}$	1	SERVS	0.959	PRIMUS	32212
XMM00004	34.201950	-4.555520	0.93	316.8	87846.9	1.81	351.91	$2.87 \times 10^{-14}$	-0.43	$1.03 \times 10^{43}$	1	SERVS	0.41	SDSS	32213
XMM00005	34.202640	-5.690720	1.66	16.5	26430.1	1.01	52.23	$1.40 \times 10^{-14}$	-1.0	$1.81 \times 10^{44}$	1	CFHTLS	1.932	VIPERS	32213
XMM00006	34.203280	-4.315290	1.55	29.2	107957.7	1.79	65.42	$3.16 \times 10^{-15}$	-99.0	-99	1	SERVS	-99.0	-99	33213
XMM00007	34.203750	-5.433790	1.77	11.3	78270.8	1.54	41.87	$5.06 \times 10^{-15}$	-99.0	-99	1	VIDEO	-99.0	-99	33213
XMM00008	34.203820	-4.595270	1.17	114.8	83485.0	1.49	168.25	$1.31 \times 10^{-14}$	-0.48	$2.21 \times 10^{42}$	1	VIDEO	0.294	SDSS	33213
XMM00009	34.204670	-5.378240	1.35	57.1	93769.9	1.40	101.92	$7.31 \times 10^{-15}$	-1.0	-99	1	SERVS	-99.0	-99	33213
XMM00010	34.204770	-4.520790	1.51	32.0	77664.5	1.51	71.54	$6.12 \times 10^{-15}$	-1.0	-99	1	SERVS	-99.0	-99	33213

**Table B.** The NWAY matching results with a selection of columns. Empty or null values are marked as  $-99$ . See Appendix B for a detailed description of each column. This table is available in its entirety in machine-readable form online.

XID (1)	P_ANY (2)	P_I (3)	SERVS_ID (12)	SERVS_MAG1 (20)	VIDEO_ID (13)	VIDEO_KSMAG (30)	CFHT_ID (14)	CFHT_IMAG (38)	HSC_ID (15)	HSC_IMAG (46)	MATCH_FLAG (52)
XMM00000	0.00331	0.95439	701845.0	19.32	-99	-99.0	-99	-99.0	-99	-99.0	1
XMM00001	0.99892	0.99138	408032.0	19.36	644246149826	20.17	1114_171196	-99.0	37485121644831650	-99.0	1
XMM00002	0.99384	0.98228	162933.0	19.72	644245967165	19.36	1114_017717	-99.0	37485108759911146	-99.0	1
XMM00003	0.98899	0.98536	595262.0	18.96	644246286360	19.57	1105_044095	-99.0	37485134529718079	-99.0	1
XMM00004	0.99204	0.98602	571059.0	18.82	644246268652	18.37	1105_032861	-99.0	37485130234758414	-99.0	1
XMM00005	0.72516	0.99503	-99.0	-99.0	-99	-99.0	1123_209193	-99.0	37485104464927930	-99.0	1
XMM00006	0.02211	0.23506	-99.0	-99.0	644246338512	23.19	-99	-99.0	-99	-99.0	2
XMM00006	0.02211	0.24837	647512.0	22.23	-99	-99.0	-99	-99.0	-99	-99.0	1
XMM00006	0.02211	0.17095	647512.0	22.23	644246338512	23.19	1105_084654	-99.0	38549431720610895	-99.0	2
XMM00007	0.01938	0.17482	-99.0	-99.0	644246413618	22.54	-99	-99.0	-99	-99.0	2
XMM00007	0.01938	0.33487	-99.0	-99.0	644246382177	21.59	-99	-99.0	-99	-99.0	1

**Table C.** The photometric redshifts for galaxies detected in the N18 forced-photometry catalog, see Appendix C for details. Columns 1–3: VIDEO object ID, RA, and DEC (J2000). Columns 4–6: SERVS object ID, RA, and DEC (J2000). Column 7: photometric redshift. Column 8: 68% uncertainties of the photometric redshift. Column 9: photometric redshift quality parameter, see §4.5 for details. Column 10: Spectroscopic redshift. Null values are filled with  $-99$ . Columns 11–12: Similar to Columns 183–184 of Table A. This table is available in its entirety in machine-readable form online.

VIDEO_ID (1)	VIDEO_RA (2)	VIDEO_DEC (3)	SERVS_ID (4)	SERVS_RA (5)	SERVS_DEC (6)	Photo-z (7)	pz_err (8)	Qz (9)	Spec-z (10)	Spec-z Ref. (11)	Spec-z flag (12)
644246417039	34.559784	-4.966628	419320	34.552429	-4.971455	0.890	0.084	0.166874	-99	...	...
644246232645	34.826369	-4.664200	463179	34.826399	-4.664191	0.729	0.89	0.025925	0.7615	VIPERS	2.5
644246414844	34.865246	-5.255360	217192	34.866427	-5.256932	1.239	0.478	0.767938	-99	...	...
644245112476	35.980791	-5.384739	79929	35.980755	-5.384734	0.799	0.169	0.351430	1.009558	PRIMUS	3
644245112310	35.990999	-5.385472	79380	35.991092	-5.385497	0.431	0.146	0.224409	0.513350	PRIMUS	4
644245264327	36.514834	-4.820542	242344	36.513482	-4.818775	0.010	0.07	0.189810	0.2036	VVDS	3
644245264275	36.703210	-4.820681	223967	36.708090	-4.822620	0.781	0.125	0.100374	0.8856	VVDS	3
644245095781	36.726222	-5.469834	23657	36.726183	-5.469784	0.781	0.08	0.138805	0.782320	SDSS	0
644245094723	36.917557	-5.477334	16945	36.917509	-5.477157	0.781	0.09	0.092994	0.796421	SDSS	0
644245094839	37.109022	-5.476115	11526	37.109010	-5.476131	0.872	0.141	0.352668	1.128211	SDSS	0

## REFERENCES

- Aihara H., et al., 2017, eprint arXiv:1702.08449
- Alam S., et al., 2015, *ApJS*, **219**, 12
- Assef R. J., et al., 2013, *The Astrophysical Journal*, **772**, 26
- Bradshaw E. J., et al., 2013, *Monthly Notices of the Royal Astronomical Society*, **433**, 194
- Brammer G. B., van Dokkum P. G., Coppi P., 2008, *The Astrophysical Journal, Volume 686, Issue 2, article id. 1503-1513, pp. (2008)..*, 686
- Brandt W. N., Alexander D. M., 2015, *The Astronomy and Astrophysics Review*, **23**, 1
- Broos P. S., Feigelson E. D., Townsley L. K., Getman K. V., Wang J., Garmire G. P., Jiang Z., Tsuboi Y., 2007, *The Astrophysical Journal Supplement Series*, **169**, 353
- Broos P. S., et al., 2011, *The Astrophysical Journal Supplement, Volume 194, Issue 1, article id. 2, 19 pp. (2011)..*, 194
- Brusa M., et al., 2007, *The Astrophysical Journal Supplement Series*, **172**, 353
- Cappelluti N., et al., 2007, *The Astrophysical Journal Supplement Series*, **172**, 341
- Cappelluti N., et al., 2009, *Astronomy and Astrophysics*, **497**, 635
- Chiappetti L., et al., 2005, *Astronomy & Astrophysics*, **439**, 413
- Civano F., et al., 2016, *The Astrophysical Journal*, **819**, 62
- Coil A. L., et al., 2010, *The Astrophysical Journal, Volume 741, Issue 1, article id. 8, 15 pp. (2011)..*, 741
- Dawson K. S., et al., 2013, *AJ*, **145**, 10
- Diehl H. T., et al., 2014, in Peck A. B., Benn C. R., Seaman R. L., eds, Vol. 9149, Proceedings of the SPIE, Volume 9149, id. 91490V 15 pp. (2014).. p. 91490V, doi:10.1117/12.2056982, <http://proceedings.spiedigitallibrary.org/proceeding.aspx?doi=10.1117/12.2056982>
- Donley J. L., et al., 2012, *Astrophys. J.*, **748**, 142
- Driver S. P., Robotham A. S. G., 2010, *MNRAS*, **407**, 2131
- Evans I. N., et al., 2010, *The Astrophysical Journal Supplement Series*, **189**, 37
- Falocco S., et al., 2017, preprint, (<arXiv:1709.10290>)
- Franzen T. M. O., et al., 2015, *Monthly Notices of the Royal Astronomical Society, Volume 453, Issue 4, p.4020-4036*, 453, 4020
- Garilli B., et al., 2014, *Astronomy & Astrophysics*, **562**, A23
- Hasinger G., Burg R., Giacconi R., Schmidt M., Trumper J., Zamorani G., 1998, *A&A*, **329**, 482
- Hasinger G., et al., 2007, *ApJS*, **172**, 29
- Hudelot P., et al., 2012, VizieR On-line Data Catalog: II/317. Originally published in: SPIE Conf. 2012, 2317
- Jarvis M. J., et al., 2012, *Monthly Notices of the Royal Astronomical Society*, **428**, 1281
- Jarvis M. J., et al., 2017, preprint, (<arXiv:1709.01901>)
- Kelson D. D., et al., 2014, *The Astrophysical Journal*, **783**, 110
- Kim M., Wilkes B. J., Kim D., Green P. J., Barkhouse W. A., Lee M. G., Silverman J. D., Tananbaum H. D., 2007, *The Astrophysical Journal*, **659**, 29
- Klypin A., Yepes G., Gottlöber S., Prada F., Heß S., 2016, *Monthly Notices of the Royal Astronomical Society*, **457**, 4340
- LaMassa S. M., et al., 2016, *The Astrophysical Journal*, **817**, 172
- Lacy M., et al., 2004, *Astrophys. J. Suppl. Ser.*, **154**, 166
- Lang D., Hogg D. W., Mykytyn D., 2016, The Tractor: Probabilistic astronomical source detection and measurement, *Astrophysics Source Code Library* (ascl:1604.008)
- Le Fevre O., et al., 2013, *Astronomy & Astrophysics*, **559**, A14
- Liu Z., et al., 2016, *Monthly Notices of the Royal Astronomical Society*, **459**, 1602
- Lonsdale C. J., et al., 2003, *The Publications of the Astronomical Society of the Pacific, Volume 115, Issue 810, pp. 897-927, 115*, 897
- Luo B., et al., 2010, *The Astrophysical Journal Supplement Series*, **187**, 560
- Luo B., et al., 2017, *The Astrophysical Journal Supplement Series*, **228**, 2
- Mainieri V., et al., 2007, *ApJS*, **172**, 368
- Mateos S., Saxton R. D., Read A. M., Sembay S., 2009, *Astronomy and Astrophysics*, **496**, 879
- Mateos S., Alonso-Herrero A., Carrera F. J., Blain A., Severgnini P., Caccianiga A., Ruiz A., 2013, *Mon. Not. R. Astron. Soc.*, **434**, 941
- Mauduit J. C., et al., 2012, *Publications of the Astronomical Society of Pacific, Volume 124, Issue 917, pp. 714 (2012)..*, 124, 714
- McLure R. J., et al., 2013, *Monthly Notices of the Royal Astronomical Society*, **428**, 1088
- Meneux B., et al., 2009, *Astronomy & Astrophysics*, **505**, 463
- Menzel M. L., et al., 2016, *Monthly Notices of the Royal Astronomical Society*, **457**, 110
- Momcheva I. G., et al., 2016, *The Astrophysical Journal Supplement Series*, **225**, 27
- Moster B. P., Somerville R. S., Newman J. A., Rix H.-W., 2011, *ApJ*, **731**, 113
- Nyland K., et al., 2017, *The Astrophysical Journal Supplement Series*, **230**, 9
- Oliver S. J., et al., 2012, *Monthly Notices of the Royal Astronomical Society*, **424**, 1614
- Pacaud F., et al., 2006, *Monthly Notices of the Royal Astronomical Society*, **372**, 578
- Paolillo M., et al., 2017, *MNRAS*, **471**, 4398
- Patel S. G., Kelson D. D., Williams R. J., Mulchaey J. S., Dressler A., McCarthy P. J., Shectman S. A., 2015, *The Astrophysical Journal Letters, Volume 799, Issue 2, article id. L17, 5 pp. (2015)..*, 799
- Pierre M., et al., 2016, *Astronomy & Astrophysics*, **592**, A1
- Pineau F.-X., et al., 2017, *Astronomy & Astrophysics*, **597**, A89
- Polletta M., et al., 2007, *ApJ*, **663**, 81
- Ranalli P., et al., 2013, *Astronomy & Astrophysics*, **555**, A42
- Ranalli P., et al., 2015, *Astronomy & Astrophysics*, **577**, A121
- Rosen S. R., et al., 2016, *Astronomy & Astrophysics*, **590**, A1
- Salvato M., et al., 2017, eprint arXiv:1705.10711
- Skelton R. E., et al., 2014, *The Astrophysical Journal Supplement Series, Volume 214, Issue 2, article id. 24, 49 pp. (2014)..*, 214
- Skibba R. A., et al., 2014, *The Astrophysical Journal*, **784**, 128
- Skrutskie M. F., et al., 2006, *AJ*, **131**, 1163
- Stark A. A., Gammie C. F., Wilson R. W., Bally J., Linke R. A., Heiles C., Hurwitz M., 1992, *ApJS*, **79**, 77
- Stern D., et al., 2005, *Astrophys. J.*, **631**, 163
- Stern D., et al., 2012, *Astrophys. J.*, **753**, 30
- Sutherland W., Saunders W., 1992, *Monthly Notices of the Royal Astronomical Society*, **259**, 413
- Takada M., et al., 2014, *PASJ*, **66**, R1
- Tanaka M., et al., 2018, *PASJ*, **70**, S9
- Tonry J. L., et al., 2011, *The Astrophysical Journal, Volume 745, Issue 1, article id. 42, 13 pp. (2012)..*, 745
- Ueda Y., et al., 2008, *The Astrophysical Journal Supplement Series*, **179**, 124
- Vaccari M., 2015, in The Many Facets of Extragalactic Radio Surveys: Towards New Scientific Challenges. p. 27 (<arXiv:1604.02353>)
- Vaccari M., 2016, *The Universe of Digital Sky Surveys*, **42**, 71
- Vaccari M., et al., 2016, in Proceedings of the 4th Annual Conference on High Energy Astrophysics in Southern Africa (HEASA 2016). January 13th, 2016. South African Astronomical Observatory (SAAO), Cape Town, South Africa. Online at <A href="http://pos.sissa.it/cgi-bin/reader/conf.cgi?confid=275">http://pos.sissa.it/cgi-bin/reader/conf.cgi?confid=275</A>, id.26. p. 26 (<arXiv:1704.01495>)
- Warren S. J., et al., 2007, ArXiv Astrophysics e-prints,
- Watson M. G., et al., 2008, *Astronomy and Astrophysics*, **493**,

- 339  
Xue Y. Q., 2017, [New Astron. Rev.](#), **79**, 59  
Xue Y. Q., et al., 2011, [The Astrophysical Journal Supplement Series](#), **195**, 10  
Xue Y. Q., Luo B., Brandt W. N., Alexander D. M., Bauer F. E., Lehmer B. D., Yang G., 2016, [ApJS](#), **224**, 15  
Yang G., et al., 2014, [The Astrophysical Journal Supplement Series](#), **215**, 27  
Yang G., et al., 2016, [The Astrophysical Journal](#), Volume 831, Issue 2, article id. 145, 20 pp. (2016)., 831  
Yang G., et al., 2017, preprint, ([arXiv:1710.09399](#))  
York D. G., et al., 2000, [Astron. J.](#), **120**, 1579  
Zheng X. C., et al., 2017, [ApJ](#), **849**, 127  
de la Torre S., et al., 2010, [Monthly Notices of the Royal Astronomical Society](#), Volume 409, Issue 2, pp. 867-872., 409, 867

This paper has been typeset from a T<sub>E</sub>X/L<sub>A</sub>T<sub>E</sub>X file prepared by the author.